

BRNO UNIVERSITY OF TECHNOLOGY

Faculty of Electrical Engineering  
and Communication

DOCTORAL THESIS

Brno, 2020

Ing. NIKOLA PAPEŽ



# BRNO UNIVERSITY OF TECHNOLOGY

VYSOKÉ UČENÍ TECHNICKÉ V BRNĚ

## FACULTY OF ELECTRICAL ENGINEERING AND COMMUNICATION

FAKULTA ELEKTROTECHNIKY A KOMUNIKAČNÍCH TECHNOLOGIÍ

## DEPARTMENT OF PHYSICS

ÚSTAV FYZIKY

## DEGRADATION OF GAAS SOLAR CELLS

DEGRADACE SOLÁRNÍCH ČLÁNKŮ NA BÁZI GAAS

### DOCTORAL THESIS

DIZERTAČNÍ PRÁCE

### AUTHOR

AUTOR PRÁCE

Ing. Nikola Papež

### ADVISOR

VEDOUCÍ PRÁCE

Mgr. Dinara Sobola, Ph.D.

BRNO 2020

## **ABSTRACT**

Gallium arsenide based solar cells are among the most powerful types of solar cells available. Their main advantage is excellent resistance to thermal and ionising radiation, and therefore they are used primarily in demanding conditions. This dissertation describes the state of GaAs photovoltaic cells exposed to thermal stress, high cooling, gamma radiation and broad-spectrum laser irradiation. The samples were examined before, after and during these processes using several analytical and characterisation methods. The measurements were focused on the characterisation of the surface, optical and electrical properties. Limits and new behaviour of this type of photovoltaic cells have been discovered, which are also affected by thin protective and anti-reflective layers.

## **KEYWORDS**

degradation, gallium arsenide, solar cells, gamma irradiation, thermal processing, cooling, supercontinuum laser

## **ABSTRAKT**

Solární články na bázi arsenidu gallia patří mezi nejvýkonější typ dostupných solárních článků vůbec. Jejich výhodou je výborná odolnost vůči tepelnému a ionizujícímu záření, a proto se využívají zejména v náročných podmínkách. Tato disertační práce popisuje stav GaAs fotovoltaických článků vystavených vůči tepelnému namáhání, vysokému ochlazování, gama záření a ozáření širokospektrálním laserem. Vzorky byly zkoumány před, po a i během těchto procesů pomocí několika analytických a charakterizačních metod. Měření bylo zaměřeno na charakterizaci povrchu, optických a elektrických vlastností. Byly objeveny limity a nové chování tohoto typu článků, které jsou ovlivněny i tenkými ochrannými a antireflexními vrstvami.

## **KLÍČOVÁ SLOVA**

degradace, arsenid gallia, solární články, gama ozařování, teplotní namáhání, ochlazování, superkontinuální laser

PAPEŽ, Nikola. *Degradation of GaAs solar cells*. Brno, 2020, 126 p. Doctoral thesis. Brno University of Technology, Faculty of Electrical Engineering and Communication, Department of Physics. Advised by Mgr. Dinara Sobola, Ph.D.

---

## DECLARATION

I declare that I have written the Doctoral Thesis titled “Degradation of GaAs solar cells” independently, under the guidance of an advisor and using exclusively the technical references and other sources of information cited in the thesis and listed in the comprehensive bibliography at the end of the thesis.

As the author I furthermore declare that, with respect to the creation of this Doctoral Thesis, I have not infringed any copyright or violated anyone’s personal and/or ownership rights. In this context, I am fully aware of the consequences of breaking Regulation § 11 of the Copyright Act No. 121/2000 Coll. of the Czech Republic, as amended, and of any breach of rights related to intellectual property or introduced within amendments to relevant Acts such as the Intellectual Property Act or the Criminal Code, Act No. 40/2009 Coll., Section 2, Head VI, Part 4.

Brno .....

.....

author’s signature



## DEDICATION

I would like to dedicate this work to my son Elias, who always makes me happy.

## ACKNOWLEDGEMENT

As a first and not the last my acknowledgement belongs to my supervisor Mgr. Dinara Sobola, Ph.D. for her professional guidance, consultations, patience and contributing ideas to my work.

Further, acknowledgement goes to the whole team of our department, especially to Ing. Robert Macků, Ph.D., Ing. Pavel Škarvada, Ph.D. and doc. Ing. Petr Sedlák, Ph.D. for their advice, views and professional assessment of my work. And of course to prof. Ing. Lubomír Grmela, CSc., head of department.

I also thank Mgr. Jakub Makal and Ing. Pavel Kaspar, Ph.D. for grammar check of this work.

The last thank goes to my mother for taking care of me during the whole time I was working on my dissertation and to the most beautiful girl, who has always supported me, Tatiana.

# Contents

<b>Introduction</b>	<b>11</b>
<b>1 State of the art</b>	<b>13</b>
<b>2 Aims and objectives</b>	<b>14</b>
2.1 Stress at high temperatures . . . . .	15
2.2 Stress at low temperatures . . . . .	15
2.3 Irradiation processing . . . . .	15
<b>3 Theoretical basis</b>	<b>16</b>
3.1 Classification of solar cells . . . . .	16
3.1.1 1 <sup>st</sup> generation – silicon based solar cells . . . . .	16
3.1.2 2 <sup>nd</sup> generation – thin-film solar cells . . . . .	18
3.1.3 3 <sup>rd</sup> generation – new emerging technology . . . . .	20
3.2 Applications of solar cells . . . . .	21
3.2.1 Use of multiple layers . . . . .	21
3.2.2 Use of concentrators . . . . .	22
3.2.3 Space applications . . . . .	25
3.3 Degradation processes . . . . .	30
3.3.1 Degradation due to defects caused during production . . . . .	31
3.3.2 Degradation due to external conditions . . . . .	31
3.4 Possibilities of investigation and analysis . . . . .	35
3.4.1 Atomic force microscopy . . . . .	35
3.4.2 Scanning electron microscopy . . . . .	35
3.4.3 Raman spectroscopy . . . . .	37
3.4.4 Secondary ion mass spectrometry . . . . .	38
3.4.5 Reflectance . . . . .	39
3.4.6 Ellipsometry . . . . .	39
3.4.7 Electroluminescence . . . . .	40
3.4.8 Electrical characteristics . . . . .	40
3.4.9 Thermal observations . . . . .	46
3.4.10 Fourier transform infrared spectroscopy . . . . .	47
<b>4 Methodology</b>	<b>48</b>
4.1 Used specimens . . . . .	48
4.2 Experimental methods . . . . .	49
4.2.1 Heating to high temperatures . . . . .	50
4.2.2 Cooling to low temperatures . . . . .	50

4.2.3	Irradiation with gamma rays . . . . .	52
4.2.4	Irradiation with broadband light source . . . . .	52
4.3	Examined properties of the solar cell . . . . .	53
4.3.1	Structural morphology and material properties . . . . .	54
4.3.2	Optical properties . . . . .	57
4.3.3	Electrical properties . . . . .	57
<b>5</b>	<b>Experimental results</b>	<b>59</b>
5.1	Mechanical stress and fabrication defects . . . . .	59
5.2	High-temperature processing . . . . .	62
5.3	Low-temperature processing . . . . .	69
5.4	Ionising radiation processing . . . . .	72
5.5	Exposure to the supercontinuum light beam . . . . .	86
	<b>Conclusion</b>	<b>93</b>
	<b>References</b>	<b>96</b>
	<b>List of units</b>	<b>104</b>
	<b>List of symbols</b>	<b>105</b>
	<b>List of acronyms</b>	<b>107</b>
	<b>List of used instruments</b>	<b>110</b>
	<b>A Figures</b>	<b>112</b>
	<b>B Curriculum Vitae</b>	<b>120</b>

# List of Figures

3.1	Silicon PV cells efficiency . . . . .	17
3.2	Silicon PV cells price per watt in the years 1977–2015 . . . . .	17
3.3	Polymer and silicon PV cell difference in function . . . . .	21
3.4	Spectral region of absorption of a second generation solar cell . . . . .	22
3.5	Fresnel lens concentrator without SOE . . . . .	23
3.6	Parabolic mirrors concentrator without optical lenses. . . . .	24
3.7	Luminescent concentrators using glass layers . . . . .	24
3.8	Mirror construction as reflectors . . . . .	25
3.9	Simplified radiation spectrum . . . . .	31
3.10	Cobalt-60 decay scheme . . . . .	33
3.11	Electron scattering and X-ray generation simulation . . . . .	35
3.12	Electron beam-induced current wiring diagram in X-EBIC mode. . . . .	37
3.13	The main principle of ellipsometry . . . . .	39
3.14	Equivalent single diode model of PV cell . . . . .	41
3.15	p-AlGaAs/n-GaAs energy band diagram and 2DHG . . . . .	42
3.16	Energy band diagram of a PN junction in forward and reverse bias . . . . .	42
3.17	The process of creating an electron-hole pair when irradiated with light . . . . .	44
4.1	Detail of the sample captured by optical microscope . . . . .	48
4.2	Solar cell model, its layer distribution, and structure . . . . .	49
4.3	The process of eight measurement points during cooling to $-100^{\circ}\text{C}$ . . . . .	51
4.4	The process of three measurement points during cooling to $-120^{\circ}\text{C}$ . . . . .	51
4.5	Declared spectral power density depending on wavelength for SL . . . . .	53
5.1	Cross-section of a GaAs solar cell and its contact. . . . .	59
5.2	Cross-section of a GaAs solar cell visualised by EBIC . . . . .	59
5.3	Impurity near the junction of GaAs based solar cell . . . . .	60
5.4	Inactive part on silicon solar cell . . . . .	61
5.5	Crack on silicon solar cell visualised by EBIC . . . . .	62
5.6	Solar cell before and after thermal processing scanned by AFM . . . . .	63
5.7	Histogram of heights from thermal processing scanned by AFM . . . . .	63
5.8	Raman spectrum before and after thermal processing . . . . .	64
5.9	Comparison of I-V characteristics before and after thermal processing . . . . .	65
5.10	Photovoltaic cell under infrared camera after thermal processing . . . . .	66
5.11	Observing by SEM after thermal stress . . . . .	67
5.12	Comparison of the elemental composition after thermal stress . . . . .	68
5.13	Difference spectrum intensity in elemental structure after thermal stress . . . . .	68
5.14	Spectral current density comparison before and after thermal processing . . . . .	69
5.15	Differences in reflectance after cooling . . . . .	70

5.16	Raman spectroscopy curves after cooling . . . . .	70
5.17	Dark and light I-V curves after cooling experiment . . . . .	71
5.18	Solar cell before and after irradiation scanned by AFM . . . . .	73
5.19	Histogram of solar cell before and after irradiation scanned by AFM .	73
5.20	Spectrophotometric measurement before and after irradiation . . . . .	74
5.21	Top layers analysed by SIMS before irradiation . . . . .	74
5.22	Substrate interface analysed by SIMS before irradiation . . . . .	75
5.23	Top layers analysed by SIMS after irradiation . . . . .	75
5.24	Substrate interface analysed by SIMS after irradiation . . . . .	76
5.25	Depth profiling of unprocessed sample using Raman spectroscopy . .	77
5.26	Depth profiling of irradiated sample using Raman spectroscopy . . . .	77
5.27	Solar cell observation by SEM with STEM detector after irradiation .	78
5.28	Defect visualisation using electroluminescence before irradiation . . .	79
5.29	Defect visualisation using electroluminescence after irradiation . . . .	79
5.30	Top view of the solar cell surface after irradiation in PV-EBIC mode	80
5.31	Detail of the solar cell surface after irradiation in PV-EBIC mode . .	81
5.32	Cross-section of GaAs-based PV cell after irradiation in X-EBIC mode	81
5.33	Real $\epsilon_1$ and imaginary $\epsilon_2$ part in ellipsometry measurement . . . . .	82
5.34	Interference of irradiated sample observed by FTIR . . . . .	83
5.35	Dark and illuminated I-V characteristic before and after irradiation .	84
5.36	Spectral current density comparison before and after irradiation . . .	84
5.37	Solar cell observing using XPS after and before gamma irradiation . .	85
5.38	Wide XPS spectra from supercontinuum laser irradiation . . . . .	86
5.39	High resolution of carbon from XPS before and after SL irradiation .	87
5.40	High resolution of oxygen from XPS before and after SL irradiation .	87
5.41	High resolution of Al2p region from XPS before and after SL irradiation	88
5.42	High resolution of Al2s region from XPS before and after SL irradiation	88
5.43	Raman spectroscopy from supercontinuum laser irradiation . . . . .	89
5.44	Reflectance measurement from supercontinuum laser irradiation . . .	90
5.45	Light I-V curves from supercontinuum laser irradiation . . . . .	90
5.46	Dark I-V curves from supercontinuum laser irradiation . . . . .	91
5.47	The whole etching process using SIMS in time dependence . . . . .	92
5.48	SIMS in detail from supercontinuum laser irradiation . . . . .	92
A.1	Highest confirmed solar cell efficiencies. . . . .	112
A.2	XPS observing during slow cooling process for C1s . . . . .	113
A.3	XPS observing during slow cooling process for O1s . . . . .	113
A.4	XPS observing during slow cooling process for Al2p . . . . .	114
A.5	XPS observing during fast cooling process of O1s, C1s and Al2p. . . .	115
A.6	Gallium elemental distribution visualised in 3D by SIMS . . . . .	116

A.7	Arsenic elemental distribution visualised in 3D by SIMS . . . . .	116
A.8	Aluminium elemental distribution visualised in 3D by SIMS . . . . .	117
A.9	Titanium elemental distribution visualised in 3D by SIMS . . . . .	117
A.10	Germanium elemental distribution visualised in 3D by SIMS . . . . .	118
A.11	Three-dimensional structure of the top layers measured by SIMS . . .	119

# Introduction

Solar cells, which are expected to be highly efficient under challenging conditions, are much more demanding than conventional silicon photovoltaic cells. In most cases, efficiencies above 40 % are only achieved using multilayer technology for the use of a wide spectral region. The production of such cells is not technologically simple, and therefore these solar cells are used only for special purposes, such as concentrators, aerospace, military, or space use. In all the cases mentioned above, the effort to keep failures to a minimum and to reduce the occurrence of defects is crucial. Such defects can occur both during production and during use in operation. The extent of the particular defects then accelerates the degree of degradation, which continues to occur and is inevitable in the time horizon. Ideally, it would be appropriate to stop the degradation. However, this is a very complex problem, which is influenced by many external and internal factors. Not only the accuracy of production is essential, but also the selection of the materials used, which are the most suitable for the given purposes, and finally the way of using the selected solar cell for its most stable operation.

It is, hence, necessary for some degradation to be present before defects can be identified. A reliable method for causing degradation is accelerated ageing, i.e. a simulation of a given process, which creates inhospitable conditions for said solar cell, thanks to which the degradation manifests itself and increase and consequently causes noticeable decreases in performance. Accelerated ageing usually results in experimentally higher conditions for a sample than in which it usually works. Alternatively, the processing method is repeated until it reaches a point in its operation life where its reduced function is already assumed.

Solar cell degradation can be analysed through countless methods. However, it is essential to understand to what extent and where the solar cell can degrade the most. Since the solar cell works on the principle of the photoelectric effect, its upper part, which is mostly exposed to wide-spectrum electromagnetic radiation, is susceptible. Surface analysis is consequently fundamental because even a slight change in the range of tens of nanometres can affect a wide range of its properties. Whether it is a different morphology, which results in a change in refractive index, or the emergence and spread of microstructural defects or even a change in elemental composition, causing different doping concentrations. These and other changes can subsequently cause a decrease in the performance of the solar cell.

GaAs-based solar cells appear to be the most suitable candidate which meets the conditions for working in a demanding environment. Their superior radiation hardness and resistance to other environmental influences make them ideal for these applications and development in the field of efficiency is continuously ongoing. The



study of their degradation is thus becoming increasingly important in terms of efforts to minimise defects, which, due to the conditions in which they must operate, can expand, and rapidly reduce the life of the cell. Solar cells of this type are used mainly in concentrators where sunlight can be up to 2000 times higher or in satellites, space probes and other space devices, where much higher ionising radiation appear than in normal conditions on Earth. From the mentioned above, it is clear that these solar cells are under enormous stress due to radiation or other external conditions.

# 1 State of the art

The topic of solar cells is very lively and discussed. Practically from the very beginning of their use, many processing methods and new types for numerous applications have been invented. Whether they are various modifications of widely available silicon solar cells, high-performance multilayer cells of group III-V, or experimentally developed, for example, perovskite and organic solar cells. Gallium arsenide based solar cells have been commonly replacing silicon solar cells in harsh environments for many years. GaAs cells also holds the record for the overall effectiveness of solar cells in general, for several years in a row. Currently, they have almost reached the maximum theoretical efficiency, which is, according to the Shockley-Queisser limit of 33.5%. From the latest measurements, an efficiency of 29.1% was achieved for this type with a single-junction structure [1]. However, this efficiency can be increased by multi-layer technology, where up to six layers are already used [2]. It is not surprising that they are deployed in the most modern terrestrial and space technologies.

For that reason, many researchers seek not only to increase efficiency but also to improve durability or reduce production costs, which are mainly due to the purity of the material [3]. It has been shown that radiation damage caused by electrons and protons can be reduced by thermal annealing at 150 °C [4]. However, it is necessary to distinguish between thermal annealing and thermal stress, where the degradation of the photovoltaic (PV) cell already appears. For passively and actively uncooled GaAs cells, where the temperature of thermal stress approaches 350 °C, the opposite adverse effects appear when the efficiency decreases. This is also reflected in the different surface structure that arises during such processing stress [5]. Similarly, it also occurs with intense gamma radiation [6, 7]. It was found that the degradation of gallium arsenide solar cells compared to silicon is up to twofold, but suitable protective coatings or various covers appear to be successful protection against both thermal and ionising radiation [8].

A material of  $\text{Al}_2\text{O}_3$  and  $\text{TiO}_2$  has become the standard for anti-reflective and protective coating, especially for space applications, since they have a transmittance property compatible with the multi-junction solar cells wavelength range. Promising then become use of anti-reflective microlens arrays that have protective layers of these materials. They work similarly to Fresnel lens in concentrators. Thanks to this technology, a photocurrent increase by the amount of 5.9% was achieved in 2019 [9]. Their advantage is also the low weight, which is desirable in some applications. It has recently been further reduced in the form of flexible substrates [10] and solar cells themselves, wherein an ultra-thin PV cell, photo-excited carriers have a very short distance to move to the terminals [11].

## 2 Aims and objectives

This dissertation aims to expand knowledge in the field of degradation and more in-depth investigation of the characteristics and processes of the solar cell based on GaAs. It is necessary to focus on the study of the surface where solar cells are most susceptible to degradation, i.e. various structural defects. It is also desirable to focus on the electrical properties of the solar cell, which loses its efficiency after degradation.

The task is to perform potential induced degradation of the most common cases in which the solar cell degrades in the form of accelerated ageing. These include thermal stress at high temperatures, cooling at low temperatures and exposure to intense radiation (ionising and non-ionising). To meet these goals, it is therefore necessary to implement methods, where such a tests would be possible ideally under the best possible conditions.

GaAs samples should ideally be single-layered to simplify the process of investigating and elucidating the underlying causes of degradation. These should also be samples that are not experimentally deployed, but samples that already have a complete structure and full use. The premise is to carry out multiple measurements to verify the results and which ideally correlate with each other.

The aim is to compare the basic properties of the solar cell to analyse the changes that have occurred after processing. Research and analysis of the following parameters are expected:

### Optical properties

- Reflectance using a spectrophotometer in the UV-VIS-NIR range.

### Structure and composition

- Chemical states and structure using Fourier-transform infrared spectroscopy (FTIR), X-ray photoelectron spectroscopy (XPS) and Raman spectroscopy.
- Evaluation of changes in layers thickness using ellipsometry.
- Elemental analysis using energy-dispersive X-ray spectroscopy (EDX).
- Search for microstructural defects by electroluminescence.
- Analysis of the surface and its structure using atomic force microscopy (AFM).
- Elemental composition of the top layers with secondary ion mass spectrometry (SIMS).
- Examination of the surface condition, contacts and layers using scanning electron microscopy (SEM).
- Recognise contamination and surface and subsurface defects with electron beam-induced current (EBIC) method.

## **Electrical properties**

- Dark and under illumination I-V characteristics.
- Noise characteristic by power spectral density (PSD).

## **2.1 Stress at high temperatures**

During the day and night alternation of temperature cycles on the Earth and the use of solar cells, especially in concentrators, extreme temperature increases can arise. It is necessary to set up a workplace where the solar cell will be stressed at high temperatures. It could also be appropriate to maintain such high temperatures and examine their long-term effect, or to find a point at which the solar cell rapidly loses its stability.

## **2.2 Stress at low temperatures**

Similarly, as with thermal processing, it is useful to find out how solar cell behaves during very low temperatures. Leaving aside polar research stations, where the use of solar power is also desirable, it has not been measured anywhere else on Earth below  $-100^{\circ}\text{C}$ . However, in space, these temperatures are typical, and even very sharp temperature differences are present. Solar cells can reach these temperatures during the opposite side of the sun's rays, for example, due to rotation in the Earth's orbit. It can usually happen that at one moment, their temperature is  $-150^{\circ}\text{C}$  and after a while,  $150^{\circ}\text{C}$ . It is, therefore, advisable to observe and analyse how they behave at such a temperature and whether this temperature is prone to degradation.

## **2.3 Irradiation processing**

In addition to thermal radiation, there is another amount of radiation that causes solar cells to degrade. It can be the ordinary radiation on the wide spectrum that the solar cell uses. However, indirect ionising radiation, especially gamma radiation, is far more harmful. When using solar cells in space, the threat of degradation due to gamma radiation is higher than on Earth. As a choice of processing solar cells and simulating similar conditions for this work, it is required to:

### **Gamma rays irradiation**

- Provide a suitable and safe place for irradiation with proper emitter.

### **Irradiation using a broadband spectrum of light**

- Assemble a workplace for irradiation with proper light source.

## 3 Theoretical basis

Considering the topic of the dissertation, the theoretical part is divided from the description of the current division of solar cells through their applications to degradation and the possibility of what properties of solar cells can be investigated and by what methods. The topics are listed and selected with a closer focus on the type of GaAs.

### 3.1 Classification of solar cells

It has not been the case for a long time that the primary fabrication material of a solar cell was a semiconductor. Solar cells have been divided into several types and generations, generally into three basic ones. Since the efficiency of solar cells varies from year to year depending on their development, it is appropriate to state the basic overview of available and experimentally developed types. These types and generations differ not only in their effectiveness but in their specialization as well.

#### 3.1.1 1<sup>st</sup> generation – silicon based solar cells

Some sources name this category as thick-film solar cells, others only silicon solar cells, as they are made entirely of silicon and differ mostly only in production technology (Fig. 3.1). In general, all subtypes of the first generation of silicon cells do not contain toxic heavy metals and are therefore considered environmentally friendly. It is the most widespread generation that still dominates the market, and is interesting mainly for its price (Fig. 3.2). The decline in the prices of photovoltaic cells is also described by Swanson's law [12], where it predicts a reduction of 75 % about every 10 years.

#### Monocrystalline silicon solar cells

Solar cells are using the process known as Czochralski to be cut off as wafers from a single pure crystal lattice structure – single-crystal silicon. However, this means that production is more demanding and therefore more expensive. For the production of p-type or n-type, boron or phosphorus would be doped. Compared to polycrystalline silicon, single crystal solar cell is used where a larger demand is placed on reduced defectivity. Nonetheless, significant losses of silicon occur during cutting, in the range of 40 % to 50 %. They have an estimated lifespan of 25 years, but in most cases, it can be up to twice as much. Moreover, there is a small efficiency improvement under high temperatures [15].

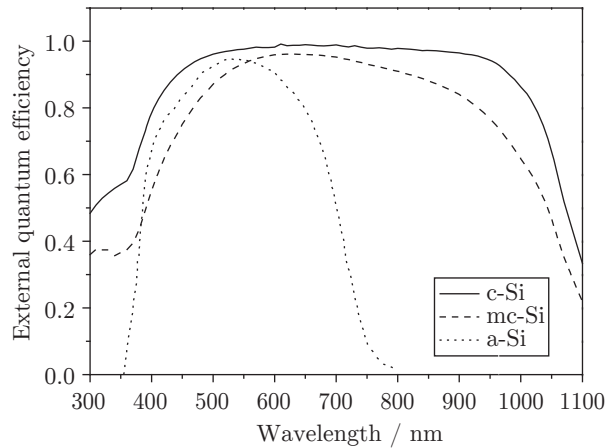


Fig. 3.1: Silicon PV cells efficiency according to different types of silicon solar cells – crystalline silicon (c-Si), multicrystalline silicon (mc-Si) and amorphous silicon (a-Si) [13].

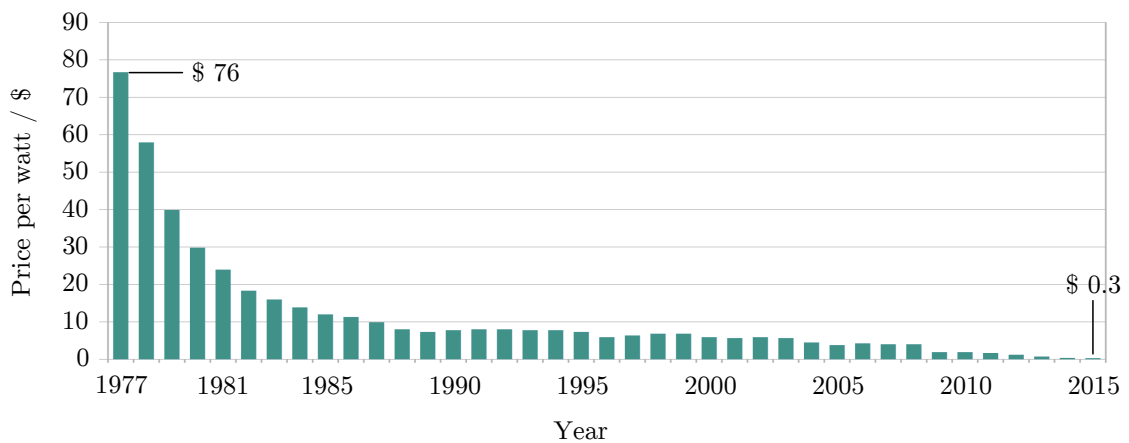


Fig. 3.2: Silicon PV cells price per watt in the years 1977–2015 [14].

### Polycrystalline silicon solar cells

They are also known as polysilicon, multi-crystalline PV cells, poly-Si or mc-Si where crystals are more massive than 1 mm. They tend to have a blue hue with visible grain boundaries against the single crystalline sc-Si with black-ish hue, mainly because of an anti-reflective coating. It is the most widely used solar cells in general, and their presence in the market is around 85%. The reason is a simple advantageous price-performance ratio.

### Amorphous silicon solar cells

If we considered the first generation to be purely silicon cells, the amorphous group would also belong there. Withal, it is already a homogeneous thin-film technology, so

it is often included in the second generation of thin-film solar cells. It is abbreviated as a-Si, and it is not the crystalline structure, this structure, unlike crystalline, consists of tiny grains called crystallites. They are applied to various rigid and flexible substrates. Nevertheless, they have a relatively high defect density, and so in 1969 fabricated by Chittick, Alexander and Sterling were developed hydrogenated amorphous silicon cells, known as a-Si:H. The disadvantage of amorphous silicon cells is their low efficiency and thus they have generally not taken hold. They are widely applied, for example, in calculators, or as solar roof tiles. In addition to solar cells, amorphous silicon is also used in LCDs using thin-film transistors [16].

### 3.1.2 2<sup>nd</sup> generation – thin-film solar cells

At the moment, the production of thin-film solar cells is considered simpler, and therefore cheaper than the first generation. Their basic principle is to evaporate a thin layer on a substrate. The amount of material used is much smaller here, but it can consist of several layers. They are mainly divided into chalcogenides and III-V group compounds as semiconductors. This generation of solar cells is already commonly used commercially.

#### Chalcogenides

Chalcogenides are compounds of chalcogenes with electropositive elements. They include, in particular, sulphides, selenides and tellurides. Chalcogenide PV materials are characterised by high absorbance, flexibility, and high-temperature coefficient.

**CADMIUM TELLURIDE (CdTe)** From the second generation, it is the most widespread and cheapest version of solar cells and is widely used in photovoltaic power stations. Their disadvantage is recycling, as cadmium is a toxic element. However, according to the European Chemicals Agency (ECHA), CdTe is no longer classified as harmful if ingested nor harmful in contact with skin [17].

**COPPER INDIUM SELENIDE (CIS) / COPPER INDIUM GALLIUM SELENIDE (CIGS)** It belongs to the semiconductor group I-III-VI<sub>2</sub>. Their advantage is deposition on very flexible substrates. Like CdTe, they are toxic. It is produced either under vacuum condition where precursors are evaporated onto heated substrate or sputtering is used at the room temperature, where the substrate is then thermally annealed using selenium vapour. It is a relatively complex process due to the reactions during this vaporization, and thus the properties of CIGS are less well controlled. Its direct bandgap can be tuned from 1.0 eV to 1.7 eV [18].

COPPER ZINC TIN SULFIDE (CZTS) AND COPPER ZINC TIN SELENIDE (CZTSE)  
This type of so-called quaternary compound PV cell is composed of only non-toxic elements. It is especially attractive because it is an indium-free variant compared to CIGS [19]. A sulfur-based version has a bandgap of  $E_g \approx 1.5$  eV and selenium-based version  $E_g \approx 1.1$  eV. It is generally considered less powerful than CIGS or CdTe. There are many alternative cation alloys to CZTSe that increase their performance as well as crystalline stability – a potential solution is the Sn cation substitution with Ge or Si. Some sources classify PV cells of this type in the third generation of emerging technology.

### III-V group compounds

According to the newer IUPAC notation, already referred to as group 13–15. Nevertheless, Roman numerals are still familiar. They are semiconductor compounds of at least two chemical elements. These are often GaAs, InP, GaInP, InGaAs or AlInGaP. Notwithstanding, they often work together, as a whole in tandem cells. Solar cells belonging to this group are among the most powerful ever (Fig. A.1). The last measurement in April 2020 reached solar conversion efficiency at 47.1% using a concentrator with a value of 143 suns and 39.2% without a concentrator with the six-junctions solar cell [2]. Of course, regarding it, they are priced differently than in the field of chalcogenide solar cells.

INDIUM PHOSPHIDE (INP) Solar cells are known mainly for their high resistance to radiation. Their direct bandgap is 1.34 eV. In most cases, it is used in combination with multilayer cells and the high energy junction as a result of its electron velocity, i.e. as a top layer to achieve the required bandgap combinations (for example GaInP/GaAs) as it has almost the same lattice as GaAs.

GALLIUM ARSENIDE (GAAS) As already mentioned, GaAs solar cells are used mainly for demanding applications such as aircraft applications, military, concentrators and space, due to their high efficiency, good temperature and radiation resistance and small size [20]. The Russian physicist Zhores Alferov awarded the Nobel prize in 2000, made a significant contribution to their development in the field of heterostructures.

This material is common not only in solar cells but also for high-frequency devices by virtue of its electron velocity. Thanks to its direct bandgap about of 1.44 eV, it tend to create noise level compared to the silicon [21]. Nevertheless, due to the availability of gallium, the production of solar cells is expensive. The price then increases the complexity of technological production, if it is mainly a multi-junction (MJ) structure.



### 3.1.3 3<sup>rd</sup> generation – new emerging technology

Cells in this generation are considered experimental and are still in development and not widespread. However, these are promising technologies that are expected to grow significantly in the future. In many cases, the PN junction is no longer used, as was the case with previous generations, it has been replaced by organic layers. Usually, the vast majority of third generation solar cells cannot be used in difficult conditions because they degrade strongly.

**PEROVSKITE** Undoubtedly, the perovskite cells can be classified among the fastest advanced solar technology according to Fig. A.1. It is an organic-inorganic structure, which can be based on tin. At the moment, they can be considered relatively unstable, as they are subject to considerable degradation in air and moisture. Therefore, they are also often encapsulated. Though, some researches prove these cells to have been stable for one year yet.

**DYE-SENSITISED** Semi-flexible and semi-transparent solar cell based on a photosensitised semiconductor called Grätzel cell or also DSSC. It is an organic dye that absorbs visible radiation as a source of energy. They degrade most when exposed to ultraviolet radiation. Of the third generation of solar cells, this is the most efficient at the moment. Because they use a liquid electrolyte, they cannot be used in a low-temperature environment because of a risk of freezing. At high temperatures, the electrolyte expands and causes mechanical stress and thus physical defects on the cell. However, it is a relatively cheap material with a simple production process.

**COLLOIDAL QUANTUM DOT** They are known as semiconductor nanocrystals or nanoparticles, also abbreviated to QDSC with a size of several nanometres that can absorb a broad-spectrum area. Their function is based on quantum mechanics. Their advantage lies in the possibility of adjusting the bandgap. The colloidal solar cell is then one among others nanoparticles that are mixed into a carrier substance, which can be, for example, plastic. For this reason, it is also clear that their effectiveness will be low. Notwithstanding, by reason of the simplicity of the application, their use is extensive. Regarding toxicity, there is a risk, especially with the heavy-metal quantum dot [22].

**POLYMER** Like plastic, they are one of the organic solar cells. Polymer PV cells consist of a transparent front electrode, which is made of semiconducting polymeric material, and a back electrode, which is printed on a plastic substrate. Polymeric PV cells cannot be compared with inorganic cells in terms of durability or efficiency,

but their flexibility and non-toxicity make them attractive. Also, no scarce materials are needed. The structure is similar, for example, to a silicon PV cell, there is a layer of electron donor and electron acceptor which are on top of each other. Unlike silicon, exciton diffusion lengths are short, so a very thin material around 10 nm is needed. Though, such a thin material is not able to absorb enough light and achieve the desired efficiency. Therefore, a so-called bulk heterojunction is formed, which is basically mixed up PN material called as an active layer, as demonstrated in Fig. 3.3. Between the active layer, there are also transport layers for electrons and donors [23].

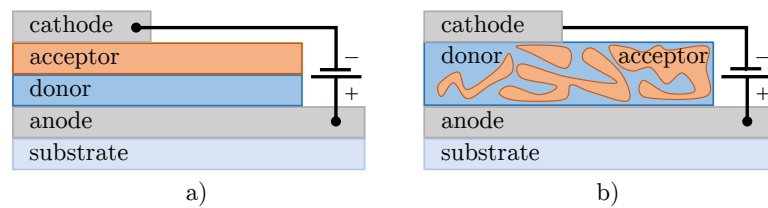


Fig. 3.3: The difference between a) an ordinary semiconductor silicon solar cell and b) an organic polymer PV cell with bulk heterojunction.

## 3.2 Applications of solar cells

It is evident that solar cells, of which solar panels or modules are composed, exist in many variations. In addition to the broadest use of silicon panels for solar energy harvesting (SEH) with solar power plants and solar systems installed on the roofs of houses, there are also special PV cell applications where they find their use. The section, therefore, deals with the use of solar cells, especially the second – thin-film generation, where gallium arsenide PV cells belong. It is also necessary to realize that the solar cell absorbs a broad wave spectrum of light, so it is not only visible light (VIS) but also light in the UV and NIR regions.

### 3.2.1 Use of multiple layers

Performance can also be increased by layering, where one solar cell can contain up to eight thin layers, each absorbing light at a specific wavelength. Such solar cells are called multi-junction or cascade solar cells using tandem fabrication, so they can also be found under the name tandem cells. Each layer contains a different composition and material with a specific bandgap that absorbs light in a particular spectral region. Usually, the top layers have a large bandgap and absorb most of the visible spectrum up to the bottom layer with a small bandgap, which absorbs

light in the UV region, as can be seen in Fig. 3.4 below. An alloy of InGaP with a range with a high bandgap of 1.92 eV to 1.87 eV is used for the top layer. Early cells used straight GaAs (1.42 eV bandgap) in the middle junction, later cells contain InGaAs alloy for a better match to Ge lattices (0.66 eV bandgap) [24]. Thus, in general, to cover most of the spectrum, aluminium can be added to the top of the band to widen the bandgap and indium to other interlayers for better matches of lattice constant. The construction of the layers of the solar cell is separated in the notation by a slash, starting with the top layer and ending with the substrate (in some literature is not always stated), for example, InGaP/GaAs/Ge [25].

Thanks to such a construction, they achieve higher efficiency than conventional single-layer solar cells. From a practical point of view, this type of solar cell is expensive for common use. The metalorganic chemical vapour deposition (MOCVD) method is commonly used. Their use is applicable only when used together with concentrators.

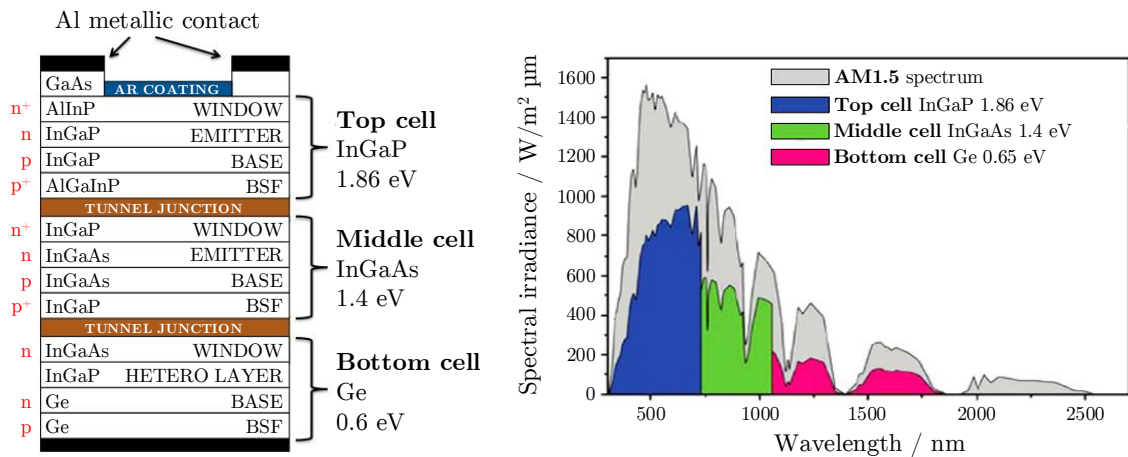


Fig. 3.4: Spectral region of absorption of the second generation solar cell [26].

### 3.2.2 Use of concentrators

Increased performance can be provided by so-called light concentrators, which are commonly used with MJ high-efficiency solar cells. Where the area of the solar cell is not enough, light is directed and concentrated to its focal point using optical devices. Concentrator photovoltaics (CPV) is used to express the intensity of concentration in the number of suns or ratios. For example, "light intensity of 20 suns". Without the concentrator, the light intensity on the solar cell would be 20× less. If the light intensity on the solar cell exceeds 10 suns, it is already necessary to use passive cooling of the PV cell. If the light intensity exceeds 100 suns, the PV cell must already be actively cooled by means of cooling fluid, and we speak of high PV

concentration (HCPV). Thus, it is clear that solar cells are exposed to extreme radiation and temperature in this case, which significantly affects the rate of their degradation. Most concentrator designs follow the concept of Fresnel lens, parabolic mirrors, luminescent concentrators or reflectors. These elements usually serve as a primary optical element (POE) [27]. Furthermore, in the case of high-quality HCPV, another optical element is used to increase the acceptance angle and increase the uniformity of the light distribution over the entire area of the cell – the secondary optical element (SOE). Light from the POE is concentrated in such an element and is usually located just above the solar cell. Thus, great emphasis is placed on design and property, as it follows that SOE operates in difficult conditions. Accordingly, the SOE of the concentrator significantly increases its acquisition price. Emphasis is thus placed on quality POE, where it is not necessary to use SOE. That is, where only one optical element is used in the construction.

Concentrators using Fresnel lenses are among the first concentrators to be used since 1979. Lenses are light and capable of achieving short focal length and large aperture. They can be used in the construction in a shape of a circle focusing the light in a point (Fig. 3.5) or in a cylindrical shape focusing the light in a line, which also results in a lower ratio concentration than in the previously mentioned construction [28].

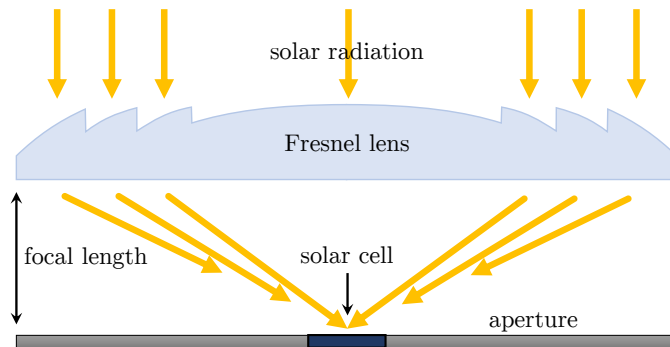


Fig. 3.5: Fresnel lens concentrator focusing the light into one point without SOE.

If optical lenses are not used, the concentrator is usually utilised using two parabolic mirrors (Fig. 3.6). The first larger mirror serves as a collector and the second as a focal point, where all the rays from the first mirror are concentrated and point further on the surface of the solar cell, which is usually placed in the middle of the first mirror. Like Fresnel lenses, they have a high ratio of around 500.

Luminescent solar concentrators (LSC) are composed of one or more glass or plastic plates (Fig. 3.7). The light captured in these plates, which serve as a waveguide, is guided to their edges by a total internal reflection (light bounces around the material) where the solar cell is located. The plates contain fluorescent dye

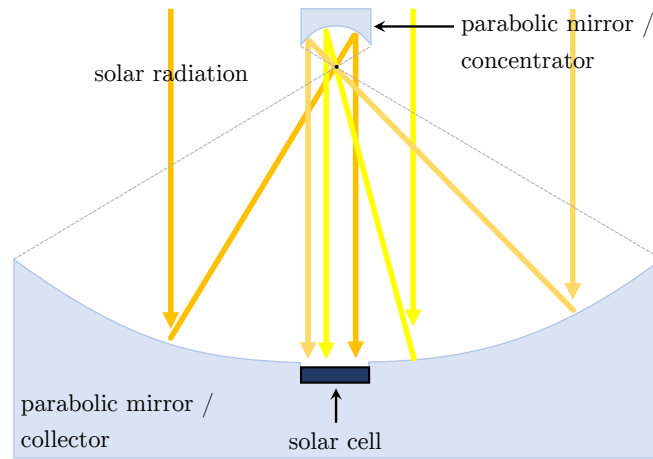


Fig. 3.6: Parabolic mirrors concentrator without optical lenses.

or quantum dots, so they emit absorbed light at longer wavelengths. Their ratio concentration factor can be up to 10, and they are used mainly as transparent and semi-transparent materials for covering buildings or as solar windows [29, 30].

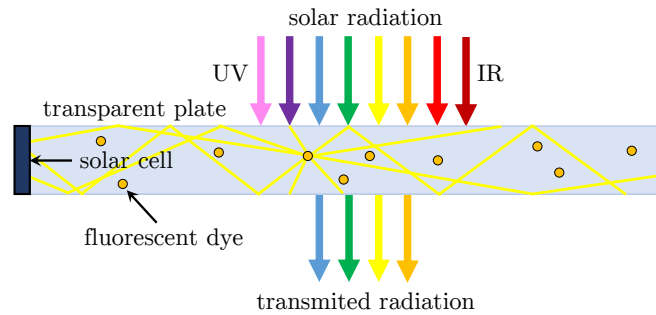


Fig. 3.7: Luminescent concentrators using glass layers.

As a low-concentration module, a concentrator using a mirror-reflector can be mentioned (Fig. 3.8). These mirrors contain a silicon-based coating because of the low loss of reflection. Their concentration ratio is given between 1.5 and 2.5. For this reason, they also do not need the use of passive cooling. They also exist with the use of silicon solar cells. Seville, Spain is the largest photovoltaic plant that also uses these reflector concentrators [31].

It is therefore clear from the above text that thin-film solar cells with high efficiency are most used in constructions with a high concentration range. These are concentrators using Fresnel lenses and parabolic concentrators, where their ratio is in the hundreds to thousands of suns. Withal, with such a high light intensity, it is necessary to take into account the side effect of heat transfer. Although there are designs that are, as already mentioned, cooled passively or actively, or even

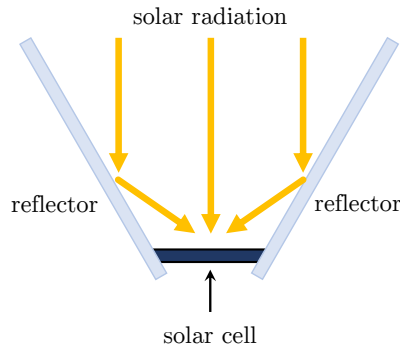


Fig. 3.8: Mirror construction as reflectors.

systems producing solar power and usable heat called concentrator photovoltaics and thermal (CPVT); solar cells in these systems are extremely stressed. The risk of their degradation thus increases sharply, and their resistance is then highly desirable. For these reasons, solar cells based on GaAs and other representatives from the field of thin-film and MJ solar cells are used in HCPV systems.

### 3.2.3 Space applications

As a result of the constant development of space technology, it is necessary to pay high importance to the applications of solar cells in space. Their use still grows in this field, as well as the demands for their function. Degradation depending on the surrounding conditions such as heat, cold, or radiation is thus a crucial key issue.

#### History and present of GaAs based PV cells in space

It is known that the Earth's atmosphere has four primary layers that protect it from harmful radiation. These layers are the troposphere, stratosphere, mesosphere, and thermosphere. However, if there was no atmosphere, the risk of ionising radiation increases several times. Since the beginning of the space race between the United States and the Soviet Union in 1957, the issue of the influence of gamma radiation on solar cells has made sense. Not only humans but also electronics require sufficient shielding from high-energy radiation from space. In 1958, the first American satellite, Vanguard 1, was launched to have solar cells installed. Thanks to solar cells, it lasted six years, ending mainly due to intense gamma radiation. At that time, solar cells were experiencing the beginning of their development, so it was not even possible to assume their increased radiation resistance, as the environment in which they worked was still not sufficiently mapped. Vanguard 1 was then equipped with silicon cells, which are not wholly suitable for space use today. Three years after the launch of Vanguard 1, the Explorer 11 orbiting satellite was launched by the

National Aeronautics and Space Administration (NASA) to measure gamma radiation precisely. The first probe to carry GaAs-based solar cells was the Soviet Venera 3 used to explore the surface of Venus. The probe was launched on November 16, 1965, from the Baikonur cosmodrome [32].

Several decades have passed since then, and dozens of different types of solar cells are currently being developed and marketed, each with its field of application. Gallium arsenide PV cells excel by cause of their radiation resistance and are thus ideal for these purposes.

One of the most famous objects using GaAs solar cells is the Hubble telescope. However, the use of solar cells in space does not only apply to satellites and other objects moving in the thermosphere. Currently, several solar system probes and other spacecraft using this type of solar cells are actively operating in space. Examples are the Venusian probe Akatsuki (InGaP/GaAs/Ge) [33], the robotic lander InSight (InGaP/InGaAs/Ge) to study the deep interior of Mars or the asteroid study probes Hayabusa2 and OSIRIS-REx [34]. Another current example is the Ingenuity helicopter equipped with solar cells, which, together with the Perseverance vehicle, are part of the cruise stage. Its entire primary part is also covered by GaAs solar cells. This mission to Mars has started at the end of July 2020.

### **Radiation intensity**

The nearest largest source of radiation in our system is the Sun. As mentioned at the beginning of this section, the Earth's atmosphere filters out dangerous radiation that protects humans from various aspects of sunlight. For the performance of solar cells; however, in terms of luminous flux, a large spectrum of energy is removed within the scattering and reflection, especially in the upper and lower latitudes. Of course, the influence of high fluctuations in available light flux also belongs to the alternation of seasons or day and night. At most, about 25 % of the solar energy did not reach the Earth's surface in clean weather and during light cirrus clouds reduce this to 50 % [35]. Beyond the Earth's atmosphere, solar cells are no longer affected by these problems, and we can achieve a wider spectrum of energy. Light flux fluctuations are thus dramatically reduced. In this case, the efficiency of the solar cell is already affected mainly by the angle of incidence of light, the distance from the Sun and an equally important factor – degradation. In some cases, where solar arrays are located on satellites, it is necessary to continually adjust the direction of their rotation relative to the Sun, which causes further loss of energy. The solution to giving access to constant sunlight can place a satellite to the Lagrange point (the point between two large bodies where the gravitational forces match up and cause the object to be in a stable or nearly stable position). In the case of the

distance from the Sun, the light emission from other cosmic objects and planets is negligible. A  $\sim 5778$  K black body approximates the Sun's spectral density of electromagnetic radiation following Planck's radiation law. The full power of solar radiation is then described by integrating across all wavelengths to give the Stefan-Boltzmann law [36]:

$$\int_0^\infty F(\lambda)d\lambda = \frac{2\pi^5 k^4}{15h^3 c^2} T^4 = \sigma T^4. \quad (3.1)$$

As mentioned, the effective temperature of the Sun is close to the 5778 K, which means that Sun's photosphere would produce an average flux of  $63.2 \text{ MW/m}^2$ . Thus, with distance from the Sun, this intensity decreases. In Earth's orbit, it is  $E_s = 1367 \text{ W/m}^2$ , which is equal to solar constant. The factor of decrease in flux is, therefore  $4.62 \times 10^4$  [37]. Concentrators are also used in space to amplify the effect of light intensity [38]. If it were necessary to calculate the solar constant on Mars, the formula would be:

$$S_C = \frac{L_\odot}{4\pi \cdot r^2}, \quad (3.2)$$

where the constant  $L_\odot$  is the solar luminosity of  $3.828 \times 10^{26} \text{ W}$  and  $r$  is the distance of Mars from the Sun, which is  $2.2794 \times 10^{11} \text{ m}$ . The solar constant on Mars would therefore be  $586 \text{ W/m}^2$ .

Because the Earth is in thermal equilibrium with this radiation equal to the solar constant, it must indeed emit the same amount. By adjusting this equality, we can approximate the effective temperature of the Earth:

$$\begin{aligned} 4\pi R_\oplus^2 \sigma T_\oplus^4 &= T_\odot^4 \frac{R_\odot^2}{a_0^2} \pi R_\oplus^2 \\ \rightarrow T_\oplus &= T_\odot \sqrt{\frac{R_\odot}{2a_0}} \approx 279 \text{ K}, \end{aligned} \quad (3.3)$$

where  $T_\oplus$ ,  $T_\odot$  and  $R_\oplus$ ,  $R_\odot$  are the effective temperatures and radii of the Sun and the Earth, and  $a_0$  is the distance of the Earth from the Sun.

Sunlight from the Earth is reflected or absorbed by the satellite and generates excess heat. The total irradiance  $E_{\text{ABS}}$  absorbed by the solar cell on the satellite can be calculated as follows:

$$E_{\text{ABS}} = T_{\text{AR}} E_s (1 - \eta) + A_{\text{BULK}} \alpha (E_s + \sigma T_\oplus^4), \quad (3.4)$$



where  $T_{\text{AR}}$  is the transmittance of the anti-reflective coating of the PV cell,  $\eta$  is the efficiency of the cell,  $A_{\text{BULK}}$  is the absorbance of the bulk cell, and  $\alpha$  is the albedo of the Earth (a diffuse reflection of solar radiation from the Sun).

### **Influence of temperature in space**

In the previous section, the possibilities of intensity of solar luminosity were explained, which is a crucial parameter for the solar cell due to its efficiency, which depends on the distance from the Sun. Another important property is its degradation occurring at different temperatures of the PV cell. Generally, it is necessary to address the issue of temperatures in space. Temperatures here are very low, but in certain situations, it is the other way around. First of all, it needs to be clarified that the term temperature of outer space is not entirely accurate. On Earth, temperature imagines kinetic activity of the gas. The universe is full of photons created during the Big Bang, called cosmic microwave background radiation (CMB) – relic radiation. However, the kinetic temperature of the gas and the temperature of the radiation of the outer space are different [39, 40]. It means that radiation and gas are not in the thermodynamic equilibrium. The black body of the background radiation can be calculated at 2.726 K ( $-270.424\text{ }^\circ\text{C}$ ), which is the current temperature of the relic radiation of the expanding universe. When a space object is rotated towards a light source (the Sun), the internal energy of the incident photon radiation can increase rapidly. For example, the International Space Station (ISS) moving in the middle of the thermosphere Sun-facing side would soar to 394 K ( $121\text{ }^\circ\text{C}$ ) and from its opposite dark side can drop to 116 K ( $-157\text{ }^\circ\text{C}$ ). In the case of solar cells, it is, therefore, necessary for them to be able to withstand extreme temperature differences, sometimes in different time cycles (if they are installed on a satellite orbiting the planet).

### **Other possible sources of energy for space use**

Satellites and space probes most often operate in a mode where their primary source of power is electricity from solar panels. If the solar panel is facing away from the Sun and is unable to power the devices, their primary source is the battery. However, some missions last for decades. In such case, considerable degradation of the battery can be expected, and the efficiency of the solar cells decreases with distance from the Sun. It was mentioned that the temperature of relic radiation in space is close to 0 K. It is appropriate to maintain thermal comfort using a heat source. Thermal comfort is essential for all electrical equipment. Suppose the duration of the space mission is assumed to be several decades. In that case, it is necessary to provide

an additional source of electricity if batteries, chemical and solar cells lose their effectiveness.

It is therefore worth mentioning that for interplanetary and out-of-Earth missions, it is appropriate to combine these resources with nuclear ones effectively. Like space radiation, GaAs-based semiconductor devices can degrade or can be damaged by radiation from some power sources. It is worth mentioning the basic overview of nuclear power sources used for space purposes, as they can indirectly affect all these semiconductor devices, which in this case is impossible to shield from dangerous radiation sufficiently.

### **Types of nuclear power sources**

- Radioisotope power sources – use the decay of radioactive nuclei. These are the most frequently used nuclear sources (already several dozen probes, especially on the outer planets).
- Nuclear reactors – use the fission of very heavy nuclei induced by neutron capture. They allow the use of high performance. They were used in Soviet radar satellites RORSAT.
- Thermonuclear power sources – use the merging of light elements. Stable process of thermonuclear reaction in the laboratory has not yet been mastered.
- Annihilation power sources – use annihilation of matter with antimatter. The biggest problem is obtaining and preserving antimatter using a particle accelerator. They have not yet been implemented or tested.

The advantage of nuclear power sources is their high efficiency of energy production and independence from the environment. They do not mind radiation, strong electric or magnetic fields. Of all energy sources, their production and price are the most demanding. In terms of safety and ecology, nuclear power sources are the riskiest. Nuclear power sources are also used as a source of energy for propulsion. Compared to chemical sources, they provide a significant difference in efficiency. However, their construction usually pays off in larger designs.

A source of radionuclide, radioactive nuclide, radioisotope or radioactive isotope (these are synonyms in all cases) releases heat during the decay of radioactive nuclei, a thermoelectric cell converts heat into electricity. It has no moving parts, so it has high reliability. It is also possible to use a Stirling engine or a gas turbine, but moving parts are already taken into account here, but the conversion of thermal energy into electrical energy is more efficient. At the same time, the decrease in the power of the radionuclide source depends on the given half-life. An example is the still active Voyager probes [41].

The most commonly used radionuclide is plutonium-238 ( $^{238}\text{Pu}$ ), with a half-life of 88 years. Its production arises from neptunium ( $^{237}\text{Np}$ ) by irradiation with  $^{238}\text{Np}$  neutrons. Its significant advantage is that it has no gamma activity so that it can be easily shielded. The disadvantage is that there is a lack of  $^{238}\text{Pu}$ . The solution to this problem is to replace plutonium-238 with americium-241 ( $^{241}\text{Am}$ ) with a half-life of 432 years. It can be obtained by chemical separation from spent fuel, so there is no irradiation in reactor. However, it is needed at  $5\times$  higher weight, as it has  $5\times$  lower activity. Its gamma activity is also noticeably more pronounced and needs to be addressed by complex shielding. Radioisotope generators are also used to distribute heat and ensure thermal comfort for devices. Such a radioisotope thermoelectric generator (RTG) is called a General Purpose Heat Source (GPHS) and is used, for example, by the New Horizons probe. There is also a reduced version called the Lightweight Radioisotope Heater Unit (LWRHU) [42].

The first nuclear reactor to serve as a source of electricity to appear in space was the SNAP-10A or SNAPSHOT, which as a nuclear powered satellite was launched by United States in 1965. Other important reactors that were also part of the RORSAT project were called TOPAZ which carried higher-orbiting satellites. The disadvantage of such satellites and probes that contain the nuclear reactor is their primary source of orbital contamination, which is considerable compared to X-rays. They pose a danger of gamma radiation both to the instruments they carry and to other satellites that sense gamma rays for astronomical purposes. The current development of new reactors for satellites is slow due to the wait for high-performance equipment where such a reactor could be used. The equipment being developed includes, for example, the Flattop reactor, which is connected to the Stirling engine, or the small Kilopower reactor [43].

### 3.3 Degradation processes

From the previous chapter, the basic properties of GaAs solar cells and the applications where they are most used were explained. From this, it can be concluded that they are very often exposed to extreme conditions, for which, however, they are intended. Naturally, we can also expect increased risks of damage to these cells and decreasing their effectiveness. This section describes the main contributors to the deterioration of solar cells. Since solar cells do not only undergo environmental degradation, they can fall into two main groups. Namely, degradation caused naturally by external influences and degradation caused by defects already during production.

### 3.3.1 Degradation due to defects caused during production

It can be said that no solar cell material is created without the defect. Defects can always be found on or in the solar cell, whether they are caused by impurities during fabrication or mechanical disorders during handling. These processes can result in increased degradation, which then results in reduced performance. In the worst case, a complete loss of functionality. The problem can be both during the production of the active layers and during the application of the anti-reflective layer. Imperfections can also arise with poorly applied contacts.

### 3.3.2 Degradation due to external conditions

Disorders can be caused not only by factors in the production of solar cells but also by environmental degradation, which is a much more common cause. It includes many other factors that affect the life of the PV cell.

## Radiation

Energy emissions in the form of waves or particles through space or matter is illustrated in Fig. 3.9, and some examples related to the topic of the dissertation are described below. The properties of the solid matter and its physical parameters are susceptible to many external factors such as pressure, temperature or various external fields. In most cases, if the source that caused this state disappears, the physical parameters of the matter will return to their original values. Also, similar behaviour occurs when other types of radiation affect the solid matter in the case of non-permanent changes in properties.

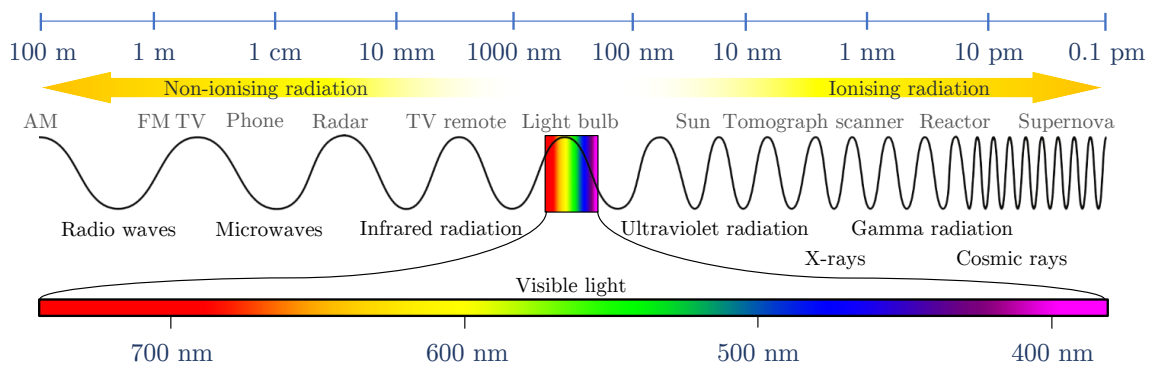


Fig. 3.9: For a basic idea, the picture shows a broad radiation spectrum. The grey text shows examples that cause radiation. The dark blue text describes the wavelength at a given point.

**GAMMA RAYS** The interaction of directly or indirectly ionising radiation with the crystalline matter has great importance in terms of recognising the properties and behaviour of particles after interaction with the matter; and changing the properties of the solid mater with which such radiation interacts. Along with the advancement of physics, chemistry and technology of crystalline semiconductors, the discovery of some of its dominant properties and its practical application in extreme conditions, the radiation resistance of these matters began to be observed.

It is known that GaAs-based solar cells have shifted the boundary of resistance to ionising radiation to higher particle or dose fluctuations. Overall, it is proven that generally, non-crystalline semiconductors are more durable and stable in high radiation environments.

Ionising radiation is any radiation that directly or indirectly ionises the environment in which it interacts. Directly ionising particles include all charged particles with sufficient kinetic energy, indirectly ionising particles (quasi-particles) without charge. Here are classified neutrons and quantities of  $\gamma$ . Each type of radiation is characterised by the type of particle (a charge, mass, energy) concerning the interacting environment and the particle flow density (fluency), in that case, the amount of energy delivered by the environment. The fluctuation of particles, together with their energy and type of radiation, is closely related to the degree of damage of the examined material.

The radiation environment is also called the environment in which any radiation and matter interact. The radiation environment is divided into:

- first level – moderate,
- second level – critical,
- third stage – aggressive.

The interaction of radiation and solids results in secondary phenomena in the material, which can be divided into two groups:

- Structural disorders – they are created by the displacement and rearrangement of atoms (molecules) in a solid. These defects usually have permanent consequences on changes in physical parameters of matter, in that case, relaxation times at the room temperature are of the order of  $10^8$  s to  $10^{10}$  s. Depending on the size of radiation fluence, is is included here gradually from interstitial (Frenkel, Schottky) defects, line defects, area defects, displacement wedges (combined with heat wedges), which may eventually overlap in aggressive radiation fluctuations and eventually lead to forming other solid structures. After thermal stabilisation of the irradiated material, the new physical parameters

are constant and depend on the fluence size of the respective radiation. Such radical changes are only capable of producing high-energy radiation with high fluctuations, where fast neutrons play a dominant role.

- Ionisation effects – arise in the reaction between the high energy ionizing particles and atoms of matter, caused the creation of ions due to detachment of electrons.

By cause of the structural disorder of non-crystalline semiconductors in terms of observing the effects of faults and their stability, structural defects play a dominant role.

As one of the most critical tests carried out on candidates of various space devices is gamma rays which confirm their suitability for space. Several institutions commonly perform radiation hardness tests on electronic compounds for space objects and other aerospace devices. For example, by the European Space Agency in its radiation testing facilities, such as in Noordwijk – Netherlands.

Cobalt-60 (Co-60 or  $^{60}\text{Co}$ ) is a by-product of nuclear reactor processes and the most common radioactive isotope of cobalt. It is established when metal structures are exposed to neutron radiation. As the radiation source is used as the agreed standard method to simulate exposure of cosmic particles in orbit for the electronic devices. Its full application finds also use for radiation therapy in the hospital during medical tests, treatments or sterilization.

Cobalt-60 decays into a stable nickel-60 ( $^{60}\text{Ni}$ ) isotope by beta particles and by two corresponding highly penetrating gamma rays as photons with energies of 1.17 MeV and 1.33 MeV (Fig. 3.10). Gamma rays are electromagnetic radiation, similar to Röntgen X-rays.

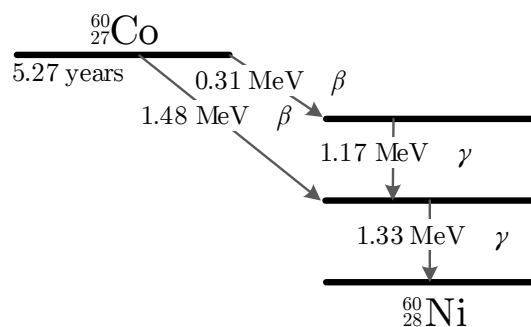


Fig. 3.10: Cobalt-60 decay scheme.

SOLAR PARTICLE EVENTS AND GALACTIC COSMIC RAYS Another particle species representatives are solar particle events (SPE) protons and galactic cosmic rays

(GCR) nucleons. These energies are much higher than gamma rays photons, as described in Fig. 3.9. As the very unpredictable, SPE can be considered. It is accelerated by the Sun flare or during coronal mass ejection (CME) shocks. Also, from the Sun or distant galaxies can originate the highly penetrating GCR. Consists of hydrogen ( $\sim 87\%$ ), helium ( $\sim 12\%$ ), and heavier nuclei ( $\sim 1\%$ ) [44].

### **Dynamic Mechanical Load**

By the term, dynamic mechanical load (DML) is meant mainly mechanical stress of cyclic flexing caused by wind. Simulated DML is performed using vacuum cups controlled by a computer that cyclically applies a pressure of about 5000 Pa to 6000 Pa to provide alternating bidirectional forces.

While properly clamped panels will not flex much, it is still enough to cause damage over time. Microcracks are frequent damage to solar cells. Such microcracks can then be studied, for example, by electroluminescence, light emission or by EBIC method.

### **Humidity and moisture**

Humidity and moisture can degrade or cause a decrease in efficiency of the PV cell in several ways. The first are water droplets, which affect the reflection of sunlight. The second is the reaction of moisture into the cell, which causes its parts to eat yellowish and corrode metal connections [45]. GaAs PV cells can be minimally encountered with this type of situation since they are used for a different purpose. Understandably, the most susceptible PV cells to moisture are from the third generation described in Sec. 3.1.3, especially perovskites.

### **Temperature influences**

As already mentioned in Sec. 3.2.3, the temperature on Earth is lower than in Earth's space orbit in direct sunlight. However, when using concentrators, the temperature conditions are many times higher. Thus, during the constant absorption of light, the energy converted into heat can be expected to have a significant effect on the solar cells. The converted and absorbed energy incident on the cell surface depends on the zenith angle of the Sun, time of the day and the latitude.

Recently, the degradation of GaAs solar cells under continuous laser irradiation was discussed by Lei Qi et al. [46] in terms of thermal-stress distributions. In this work, degradation caused by defects formed due to redistribution of aluminium and titanium components are also observed in Sec. 5.5. Light-induced degradation of silicon solar cells was reported to be connected with increasing of dislocation defects [47].

## 3.4 Possibilities of investigation and analysis

There are many methods and instruments for investigating degradation. In this section, selected methods that can provide as much information as possible about the state of the solar cell are listed further. Their mutual correlation can then confirm the resulting measurement and provide verified results.

### 3.4.1 Atomic force microscopy

Atomic force microscope (AFM) is one of the types of scanning probe microscopy (SPM). Information is gathered by “touching” the specimen surface with a cantilever with a mechanical tip. The tip is moving in raster over a surface using a moving stage and feedback loop. A laser detects the deflection of the cantilever. The method is commonly used to achieve an image of the precise three-dimensional topography. The image could be processed for better observation. The great advantage is that there is no need for special sample preparation.

### 3.4.2 Scanning electron microscopy

Electron microscopy provides a basic overview of the morphological state of a sample. Material characterisation can be extended using many other methods associated with SEM. When analysing with SEM, it should be noted that by cause of the accelerating voltage, structures up to several  $\mu\text{m}$  under the surface can be observable (Fig. 3.11).

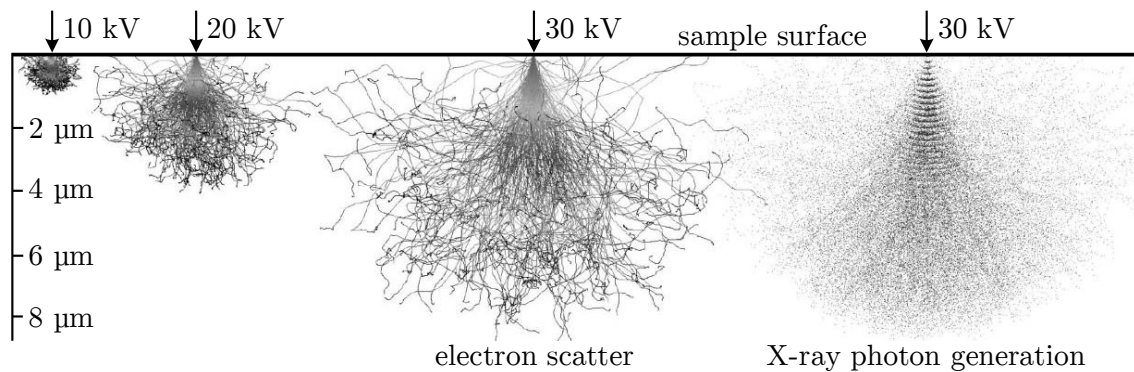


Fig. 3.11: Electron scattering and X-ray generation simulation using a Monte Carlo method on a carbon sample with density of  $2.25 \text{ g/cm}^3$  [48].



## Energy dispersive spectroscopy

It is an analytical method for elemental analysis and sample composition based on the principle of detection of characteristic X-rays by sample atoms excited by the impact of an electron or ion beam. The EDX (or EDS) detector is part of the electron microscope. Together with SEM, it is possible to create morphological and elemental distribution maps. The typical EDS spectrum is usually presented in the form of a graph of characteristic energy shells – spectral lines of the X-rays denoted as K, L, M, N, followed by  $\alpha$  and  $\beta$  which is called Siegbahn notation. The limit of EDX detection depends on many factors. In particular, these are the X-ray transition energies of each element to be detected in a sample. It also depends on the type of sample surface, where smoother surface means the lower detection limit. Major elements with a concentration above 10 wt% and minor elements with a concentration of 1 wt% to 10 wt% can be detected. Bulk materials can be detected to the 0.1 wt% [49].

## Electron beam-induced current

Electron microscopy with EBIC is mostly used for semiconductor analysis and characterization, such as surface and subsurface defect detection, contamination analysis and PN junction visualisation in sample cross-section. It can also be used to measure I-V characteristics and depletion region thickness measurements.

As its name suggests, using the electron beam when observing a sample, the induced current of the separated electrons and holes by an internal electric field flow through the circuit. If the electric field in the area of the interest is strong, for example within the depletion region of the PN junction or Schottky junction, the pair of electron-hole may be separated which will drift electrons and holes to the N and P side. The P and N sides of the sample are then connected via the current amplifier. Separated electrons and holes flow through the circuit and create the electron beam-induced current (EBIC). In the next step, the current amplifier output is used as a SEM imaging signal. When high-intensity EBIC signal is produced, it corresponds with strong image contrast.

For the sample to be connected in the circuit, the connection is releasable either directly via the cable when the connectors are out of the sample, otherwise, the sample can be connected to the ohmic contact using so-called nanomanipulators which are very thin probe tips. In the vast majority of cases, all sample manipulating and connecting takes place in the chamber of SEM under vacuum condition. The current response is then processed by the picoammeter or current amplifier as described, A/D converter (ADC) and digital signal processor (DSP) as an image part which is also illustrated in the following figure.

Samples measured by the EBIC can be observed in two ways. The first option is to use the X-EBIC mode where the electron beam is parallel to the studied junction, which is thus in cross-section view. This circuit, including the above-mentioned parts, illustrates Fig. 3.12. The second mode is called PV-EBIC, where the electron beam is in a plain view from the top, in other words perpendicular to the observed surface.

There are plenty of options for what this analytical method can be used. If we measure the semiconductor in X-EBIC mode, we can directly visualise the PN junction. By changing the bias, we can track the different changes in the junction and also measure the I-V characteristic. The typical use for plain view mode is the visualisation of grain boundaries, charge distribution and subsurface defects. EBIC can also observe electrically inactive and active impurities.

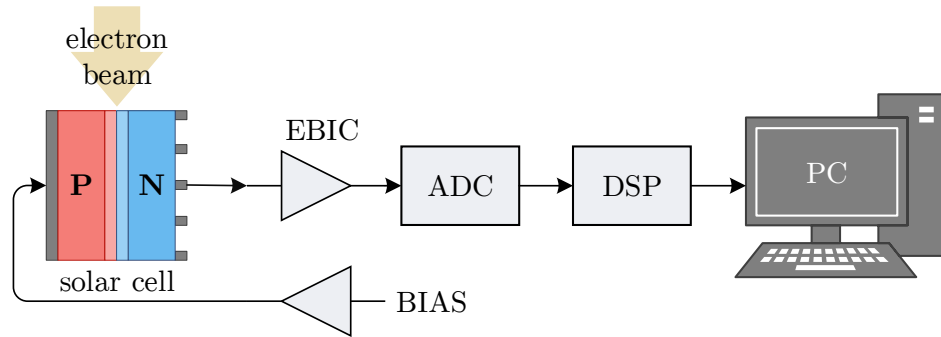


Fig. 3.12: Electron beam-induced current wiring diagram in X-EBIC mode. The diagram shows the ADC block for analogue signal conversion and the DSP block for processing the image par. (PV-EBIC mode could be also used for investigation of surface and subsurface defects. It differs only in the position of electrons incident on the solar cell.)

### 3.4.3 Raman spectroscopy

It is an optical non-destructive technique which examines inelastic scattering of photons and its vibrational excitations in the surface of the material. The shape of the spectrum is defined by the chemical composition found in the sample. Peak characteristic of different phases allows for the identification of secondary phases which are related to the process conditions of the thin-films. Also, Raman spectrometry is excellent for high spatial resolutions during surfaces mapping and analysing depth-resolved phase distributions in MJ solar cells.

The most fundamental interactions of photon and matter that occur are refraction, reflection, transmission and absorption. A part of light radiation can be scattered by the material. Elastic scattering can occur when the scattered photons

retain its energy or, conversely, inelastic scattering when the photon has lost its energy.

When light interacts with the semiconductor, the scattering of light is a direct consequence of the dielectric properties of the material. If an external electric field is applied, the atoms inside the dielectric material begin to redistribute the electric charge by polarisation (creation of an internal electric field). The newly created polarisation then compensates the external electric field. In isotropic and linear materials, the electric field of the incident radiation is linear with a polarisation response  $\vec{P}$ , according to:

$$\vec{P} = \chi \cdot \vec{E}_1 = \chi \cdot \vec{E}_1^0 \cdot \cos(\vec{k}_1 \cdot \vec{r} - \omega_1 \cdot t), \quad (3.5)$$

where  $\chi$  is the factor of electrical susceptibility of the sample, which is also interpreted as the density of electric dipoles per unit volume. The amplitude of the electric field from an electromagnetic incident wave represents  $\vec{E}_1^0$  which have wavevector  $\vec{k}_1$  and frequency  $\omega_1$ . When the applied field is oscillating, the induced polarisation field is also time-dependent, so it radiates energy according to the basic electrodynamic theory. Thanks to this, the scattering of light is interpreted based on radiation processes associated with the existence of electric dipoles at the atomic scale.

The way of atomic vibrations can be observed in the shape, intensity and frequency of the Raman bands and thus provide important information. Such properties also depend on several chemical factors, such as the chemical composition, the structure of the PV cell, impurities, stress or defects. Analysis of the Raman spectra and individual bands can then derive different physical properties of the material.

### 3.4.4 Secondary ion mass spectrometry

It is a technique responsible for the analysis of the composition of solid and thin-film surfaces by sputtering the surface by positive or negative ions using primary beam under vacuum  $<6.66 \times 10^{-5}$  Pa and collecting (analysing) the erupted secondary ions transferred to the mass spectrometer. Secondary ions emitted from the surface of the material by the "sputtering" process are used to analyse the chemical composition of the material. Notwithstanding, these particles represent only a small fraction of the particles emitted from the sample. Secondary ion mass spectroscopy is one of the most sensitive surfaces analyse capable of detecting elements, even if present only in nanometre regions.

Most trace elements can be detected when they reach a density of  $10^{12}$  to  $10^{16}$  atoms per cubic centimetre in the sample under investigation. However, this number is entirely dependent on the method used, the type of primary beam, the sample

to be analysed, and more. The sputtered area from the surface depends mainly according to the amount of the current and size of the beam from the primary ion gun. The sputtering sensitivity is also dependent on the use of an ion source ( $\text{Cs}^+$ ,  $\text{O}_2^-$ ,  $\text{Ga}^+$ , or a Bi group).

### 3.4.5 Reflectance

It is a crucial optical property of solar cells, thanks to which it is possible to observe the properties of their surface on different spectral ranges. It has a significant influence on the efficiency of the solar cell. It is possible to examine not only the differences in reflectivity but also the thickness of thin layers. Detection of wave reflection at interfaces and surfaces is used by spectrometric measurement, mostly by a probe. It measures the radiant flux reflected and absorbed by a sample. The differences then increase especially with different surface morphology, which changes depending on its degradation.

### 3.4.6 Ellipsometry

It is another a non-destructive method for determining optical parameters, especially for thin-films. For the wavelength and one beam incidence angle, two parameters ( $\Psi$  and  $\Delta$ ) describing the polarisation change upon reflection from the sample are obtained as a complex ratio of reflectance p-plane and s-plane (parallel to the plane of incidence and perpendicular to the plane of incidence) of the polarisation component (Fig. 3.13).

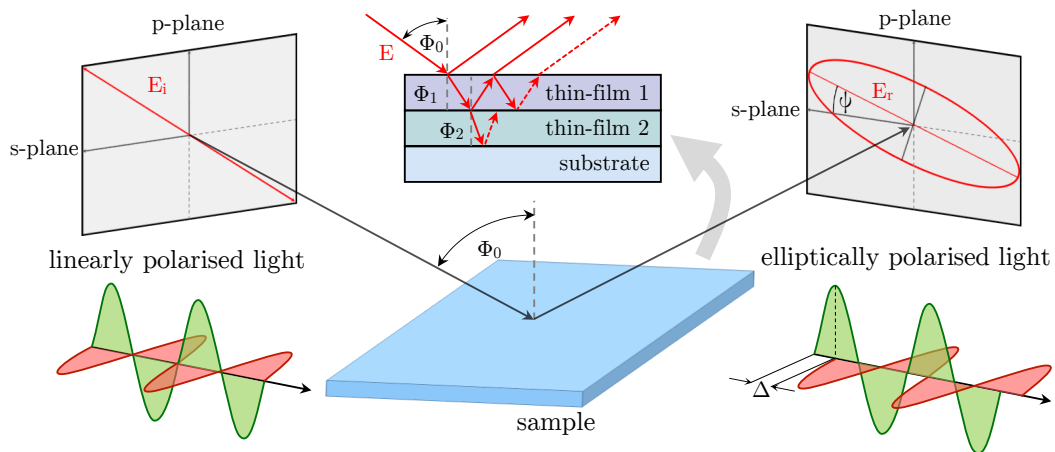


Fig. 3.13: The main principle of ellipsometry. After the impact of linearly polarised light onto the sample, it turns into elliptically polarised light with the required parameters. The penetration of light through the sample thin layers is also illustrated.

Using multiple wavelengths, the method is called spectroscopic ellipsometry. Aforementioned method also increases the accuracy of the sample thickness determination. Unlike spectrophotometry, ellipsometry does not require reference measurements. Thanks to the use of polarised light, the advantage of ellipsometry is its low sensitivity to signal fluctuations and does not require diffuse light protection. In practice, measurements at different angles of incidence are also often used.

### 3.4.7 Electroluminescence

This method makes visible the distribution of currents in a given solar cell and highlights inhomogeneities and possible local defects. Electroluminescence consists in emitting of light from the surface of the solar cell. The indicated phenomenon occurs when an electric current of a specific minimum value is allowed to flow through the PV cell. The wavelength of the emitted light depends on the material of the PV cells. Most semiconductor solar cells emit radiation in the near-infrared region. This radiation is outside the visible spectrum and is recorded by a specially adapted CCD camera. Using given method, defects can be detected inside the PV cells that might not otherwise be visible. The results of this test are grayscale images of the cell, where darker spots show worse conversion efficiency or lower current density at that point. Both indicate a defect. For fully functional samples, light colours are homogeneously distributed. This method also detects micro-cracks that can have a significant effect on the function of a part of the solar cell.

The following defects can be detected by electroluminescence:

- cracks and micro-cracks,
- electrically inactive solar cell parts,
- interrupted metallization,
- other inhomogeneities – various technological errors, diffusions.

### 3.4.8 Electrical characteristics

In electrical engineering, an equivalent electrical single diode model (Fig. 3.14), sometimes referred to a five parameter model ( $R_p$ ,  $R_s$ ,  $I_0$ ,  $I_{ph}$ ,  $n$ ), is used to understand the behaviour of a simple semiconductor solar cell.

The current source corresponding to the given solar flux and the real diode  $D$  in parallel represent an ideal solar cell model. However, such a model would not give a correct I-V and P-V characteristic. No PV cell is ideal, and therefore a resistive element called series resistance  $R_s$  is added to the model, which is the resistance of bonds between the cell and its wire leads and resistance of PV solar cell. The second

resistive element that causes power losses is a parallel leakage or shunt resistance  $R_p$ . The resulting current  $I_{pv}$  is then:

$$I_{pv} = I_{ph} - I_0 \cdot \left( e^{\frac{V_{pv} + I_{pv} \cdot R_s}{n_s V_T}} - 1 \right) - \frac{V_{pv} + I_{pv} \cdot R_s}{R_p}, \quad (3.6)$$

where  $I_{pv}$  is output current of PV cell,  $I_{ph}$  is generated photocurrent,  $I_0$  diode saturation current,  $V_{pv}$  is output voltage of PV cell,  $R_s$  is series resistance,  $R_p$  is shunt resistance,  $n_s$  is number of cells in series, and  $V_T$  is thermal voltage.

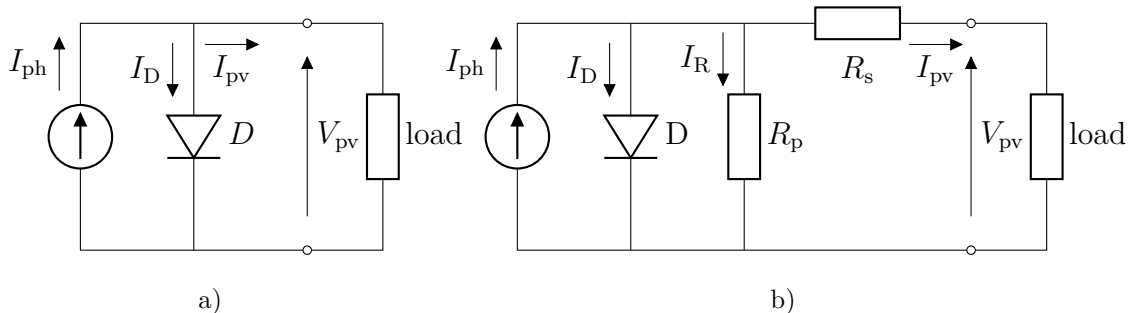


Fig. 3.14: Equivalent circuit of a) an ideal PV cell single diode model and b) with series and shunt resistance.

There is also a more complex model with a second diode in parallel, representing the effect of recombination. It is used at lower values of irradiance and low temperatures. The simulations are then more sharp and accurate. Each diode has a different ideality factor  $n^1$  [50].

Since the solar cell produces about 0.5 V, a building block called a solar panel or module with a typical number of 60 or 72 solar cells in series with a total value of 24 V is used [51].

It is worth to note that AlGaAs/GaAs PN junctions are widely used in high electron mobility transistors (HEMT). Like HEMT structures using FET transistors, an almost triangular potential well is created due to the different material bandgaps. A so-called two-dimensional hole gas (2DHG) is a model of hole gas that moves in two dimensions and is confined in the third. Thanks to the typical widths of the wave function about 10 nm, there are still observable finite-size effects, mainly in high magnetic fields. The highest curvature can also be observed from the wave function in Fig. 3.15 at the lowest point of the triangular well and the inflection point at its edge. Such structures are still in the center of interest of fundamental physics and have a potential in design of 2DEG-2DHG photovoltaic cells [52].

<sup>1</sup>Ideality factor varies from 1 to 2. The ideal diode has the value  $n = 1$ . It is an interface defect associated.

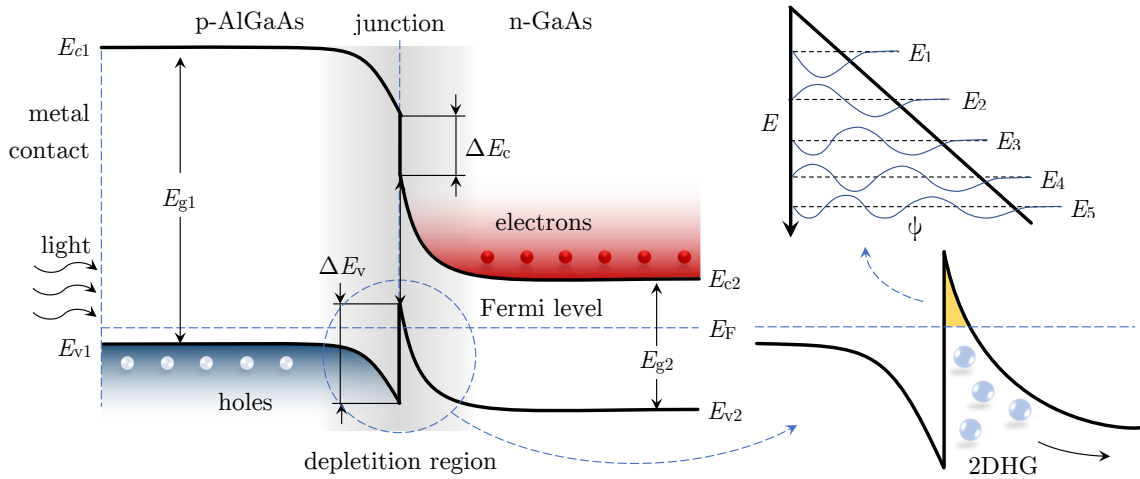


Fig. 3.15: p-AlGaAs/n-GaAs energy band diagram and formed two-dimensional hole gas.

### Dark IV curves

The primary use of dark I-V measurements is to study the diode properties. There are no light fluctuations, like in illuminated I-V measurements, where is a significant amount of noise. This is a more accurate method, where no solar simulator is used but the injection of carriers. It is a method for determining the quality of junction and contact resistivity [53].

Measurements of in forward ( $V > 0$ ) and reverse ( $V < 0$ ) bias are used. Forward biasing means positive voltage connected to the anode (p-type) and negative voltage to the cathode (n-type), which decreases the potential across the semiconductor and depletes region width and electric field (Fig. 3.16).

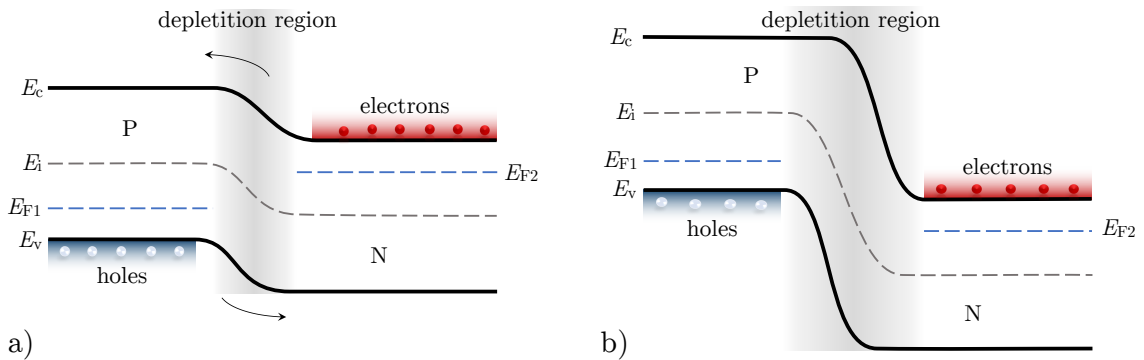


Fig. 3.16: Energy band diagram of a PN junction in a) forward and b) reverse bias.

Injection of minority carrier occurs, where electrons flood from the n-type region and holes flood from the p-type region (Fig. 3.16a). Reverse biasing means the connection of negative voltage to the anode and positive voltage to the cathode,

which increases the potential across the semiconductor, and the depletion region widens. An offset appears in the energy bands. Ideally, there is no current flow, only minority carrier can drift across the junction (Fig. 3.16b) [54].

### Illuminated IV curves

These characteristics are also often referred to light I-V measurements. As standard, a solar cell is irradiated with broad light spectrum, with a value of  $1000 \text{ W/m}^2$ . Calibrated lamps parametrically as close as possible to natural sunlight are used as a solar simulator. The most commonly are used xenon, metal halide or quartz tungsten halogen lamps. The power strongly depends on the lighting and the angle of the incident light. Therefore, the power of the cells is measured under defined conditions:

- Power density of solar radiation  $1000 \text{ W/m}^2$ .
- Radiation spectrum AM1.5.
- Solar cell temperature of  $25^\circ\text{C}$ .

The supercontinuum laser becomes a part of solar simulator when traditional lamps or light-emitting diodes are not suitable as a result of low spatial coherence of radiation [55].

Light I-V characteristics are mainly used to determine the performance and efficiency of a solar cell. The most frequently mentioned quantities are  $I_{sc}$ ,  $V_{oc}$ ,  $I_m$ ,  $V_m$ ,  $P_m$ ,  $FF$ , and  $\eta$ , where  $I_{sc}$  is short-circuit current,  $V_{oc}$  is open-circuit voltage,  $I_m$  is maximum current,  $V_m$  is maximum voltage,  $P_m$  is maximum power,  $FF$  is fill factor, and  $\eta$  is the efficiency of the solar cell.

At first, the open-circuit voltage is measured, which means the voltage at the output of the terminals at zero current – without load [56]. The equation for  $V_{oc}$  can be calculated as:

$$V_{oc} \approx \frac{nkT}{q} \cdot \ln \left( \frac{I_L}{I_0} + 1 \right). \quad (3.7)$$

Short-circuit current means that the terminals are short-circuited, and the measurement is performed at zero voltage. Since the maximum current depends on the area of the PV cell, the maximum current density  $J_{sc}$  is given instead of  $I_{sc}$  by default:

$$J_{sc} = \frac{I_{sc}}{A}, \quad (3.8)$$

where  $A$  is the area of the solar cell.



Next, the measurement is performed under load according to a given step. After recalculating and multiplying  $I$  and  $V$ , a performance P-V characteristic is created from the illuminated I-V curves and used to mark the point on the I-V curve – maximum power point (MPP). At this point in the characteristic, the solar cell delivers the maximum power.

When light hits the solar cell, the photon can be transmitted or reflected off the surface. According to Fig. 3.17, light can also be absorbed, and the majority and minority carriers will be generated. If the photon energy is the same as the value of the bandgap ( $E_{\text{ph}} = E_g$ ), this is an ideal case where there is an effective conversion and generation of electron-hole pair. When the photon's energy is lower than bandgap energy ( $E_{\text{ph}} < E_g$ ), it usually does not have enough force to excite the electron from valence band  $E_v$ . When the energy of the photon is higher than the value of bandgap energy ( $E_{\text{ph}} > E_g$ ), not only the formation of the electron-hole pair occurs, but also 1) thermalisation of electron, when the electron is excited to a higher level of energy states in the conduction band, and then it relaxes. Relaxation also occurs at the holes in the conduction band. The difference between  $E_{\text{ph}}$  and  $E_g$  is converted into heat as phonon – lattice vibration. However, an essential process is when 2) the electron from the valence band  $E_v$  will be excited to the conduction band  $E_c$ . The electric field will then 3) direct the electrons to the n-type region in conduction band  $E_c$ , the holes to the p-type region in valence band  $E_v$ , and an electric potential will begin to form [57, 58].

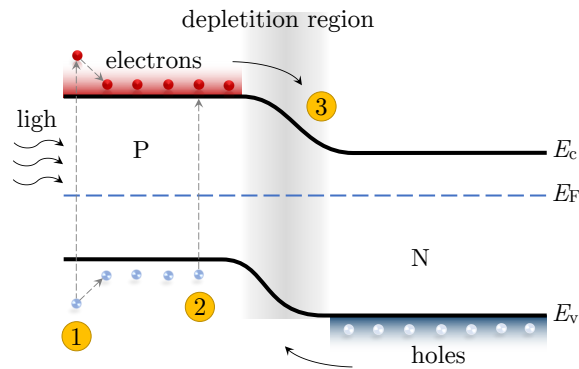


Fig. 3.17: The process of creating an electron-hole pair when irradiated with light. The energy band also shows the thermalisation of electron excess energy.

As a summary, the main issues of the cause of influencing the effectiveness of the PV cell are:

- recombination of electron-hole pair instead of its conversion into electricity,
- reflection or transmission,
- excess electron energy lost as heat,
- series and shunt resistance,
- lattice defects.

### Fluctuation processes

Noise diagnostics of solids is another method that can be used to investigate imperfections and defects in solar cells or their microphysical processes in various conductivity mechanisms. For the study of noise fluctuation and transport mechanisms a power spectral density, a spectroscopic analysis is used. Thanks to this method, it can be detected kinetic processes of charge carriers and observe different types of noise from thermal, generation-recombination to  $1/f$ , and shot noise. This information will help to determine the solar cell health state related to long-term degradation. There are several fluctuation processes, and as the most common ones that make sense in the PV cell to observe are the following [59]:

**THERMAL NOISE** Also known as Nyquist or Johnson noise, is classified as white noise and is caused by thermal agitation of electrons. Since electrons do not normally reach a quiescent state, the occurrence of this noise is constant, independent of voltage, current or frequency. For material with electrical resistance  $R$  and temperature  $T$ , thermal noise can be expressed by spectral power density  $S_u$ :

$$S_u = \frac{\overline{U_{\text{th}}^2}}{\Delta f} = 4kTR, \quad (3.9)$$

where the index  $u$  denotes the voltage fluctuation,  $U_{\text{th}}$  is the noise voltage,  $\Delta f$  is the frequency bandwidth and  $k$  is Boltzmann's constant. The current spectral density  $S_i$  equation would then look similar, where the electrical resistance  $R$  replaces the material conductivity  $G = 1/R$  and noise voltage  $U_{\text{th}}$  replaces the noise current  $I_{\text{th}}$ :

$$S_i = \frac{\overline{I_{\text{th}}^2}}{\Delta f} = 4kTG. \quad (3.10)$$

**GENERATION-RECOMBINATION NOISE** This type of noise causes fluctuations in electrons and holes in the semiconductor due to generation and recombination. It is much more common in materials with a heterogeneous structure and an increased number of defects and impurities. The detection of this noise reflects information about the density of the state of the traps occurring in the forbidden zone. It is thus possible to obtain information on the approximate number of carriers and their time of capture at the traps' levels and the activation energy.

**MICROPLASMA NOISE** It is a type of impulse noise resulting from an avalanche breakdown of the PN junction in very small fields. Thus, its occurrence indicates an intense degradation of the solar cell, indicating the destruction of the PN junction. It manifests itself as a rectangular impulse. However, it is not widely used as a diagnostic tool for cell degradation [60].

**AVALANCHE NOISE** Exists in reverse-biased PN junctions near or during avalanche breakdown. This appears during high energy carriers' impact from a strong electrical field with the crystal lattice when another electron-hole pair is generated.

**SHOT NOISE** Called also as Poisson noise, it was first observed in vacuum tubes. This noise mainly describes the potential barrier or study of the contacts and their interfaces in solar cells. It is often observed with thermal noise. Arises by cause of the discrete nature of the electric charge and random transitions through the potential barrier of the PN junction.

**FLICKER NOISE** Often referred to as pink noise or  $1/f$  noise, it arises for many different reasons, and their unambiguous determination is not easy. It is often measured for the reliability and quality of equipment. Its level is usually assessed as increasing with the number of defects. Thus, its occurrence may be due to the defects in the damaged crystal lattice, poor material contact, contact, or interaction between the charge carriers and the semiconductor's surface energy states. To examine  $1/f$  noise, it is necessary that its level is sufficiently far from thermal noise by reason of identification. It is observable between  $10^{-4}$  Hz to  $10^5$  Hz.

### **3.4.9 Thermal observations**

With the use of infrared thermography, the defect localization and thermal characterization can be observed. Samples can be measured in a steady state where they are powered in their nominal operation mode and investigated with the thermal camera. However, for more precise localization of heat sources manifesting as

stressed parts of solar cells and defects, the lock-in method is often used, known as phase-sensitive modulation thermography. The lock-in method principle is to apply a modulated bias to the sample that induces periodic thermal emission. This method serves as an excellent basis for the basic visual identification of the affected area provided as a thermal map. In combination with other morphological and analytical methods, it perfectly complements and verifies the results. The limitation of this technique occurs in the case of thermal signature defects, like open circuits. Nonetheless, current-biasing is used for PV cells. Another necessity is to compensate for emissivity issues. Emissivity is a parameter that indicates radiation emitted from the sample compared to a black body at the same temperature. That means the camera needs to be calibrated before every measurement [61].

### **3.4.10 Fourier transform infrared spectroscopy**

The infrared spectroscopy technique measures an absorption of infrared radiation of different wavelengths by the analysed material. Infrared radiation is electromagnetic radiation in the range of  $12\,800\text{ cm}^{-1}$  to  $10\text{ cm}^{-1}$ . The most commonly used is the central area of  $4000\text{ cm}^{-1}$  to  $200\text{ cm}^{-1}$ .

The principle of the method is the absorption of infrared radiation when passing through or reflecting from the sample, which causes the rotational, vibrational energy states of the molecule in dependence on changes in the structure of the molecule. The analytical output is an infrared spectrum, which is a graphical representation of the functional energy dependence, usually expressed as a percentage of transmittance or absorbance units over the wavelength of the incident radiation.

## 4 Methodology

The methodology firstly describes the tested samples in detail, then the processes by which they were stressed, and in the last part of the chapter are listed methods that were used to observe changes in the parameters of processed solar cells. This part is to introduce all technical parameters and methods used in the measurement.

### 4.1 Used specimens

As photovoltaic solar cells, GaAs-based samples were tested. This type of sample was chosen because of its high resistance to radiation and other external influences. Another reason for choosing these types of cells was their frequent use on space objects. Identically the same type of solar cells used was implemented on Iridium satellite constellation. Compared to conventional silicon PV cells, these III-V compound semiconductor units have different fabrication, coating application and substrate material. They are classified in the category of thin-film PV cells for special applications.

The exact dimensions of the solar cell are described in the images captured by an optical microscope in Fig. 4.1. The electron microscope was used for further and more accurate measurements and results. Worth to note, the relatively small width of the contacts and their pyramid shape<sup>1</sup> by virtue of the PV cell's largest possible area. The third image from Fig. 4.1 shows a cross-section and the most visible Ge substrate, which is the largest part of the solar cell. The contact is also visible here<sup>2</sup>.

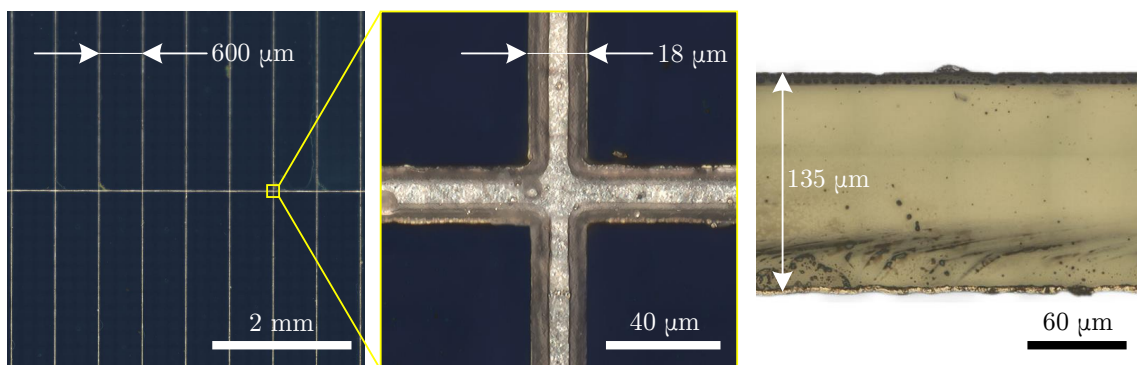


Fig. 4.1: Plain view and cross-section of the GaAs solar cell captured by optical microscope. Thanks to thin contacts, hits the surface more light, and higher efficiency is provided.

<sup>1</sup>The shape of the contact was observed on SEM in Fig. 5.11

<sup>2</sup>The cross-section of the solar cell obtained by SEM microscope is shown in Fig. 5.3

A simple description of the layers of the solar cell for a basic idea is shown in the model in Fig. 4.2, where the dimensions of individual layers and their material are described<sup>3</sup>. The total height and width of the solar cell sample were adjusted for the needs of measurements and measuring instruments.

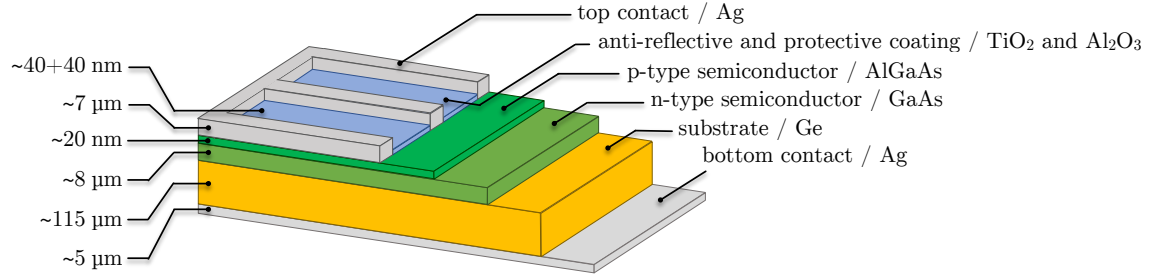


Fig. 4.2: Solar cell layer distribution, and structure. On the surface, there is the anti-reflective layer to absorb as much light as possible and the protective layer to protect against external influences. The lower layers are insulated from the air and the possibility of oxidation. A heterojunction between AlGaAs and GaAs follows this. The substrate reinforces the PV cell, and the last is a uniform layer of silver contact.

Used solar cells described in this dissertation contain a single-junction layer with silver contacts and silver backside. Thin layer of Al<sub>2</sub>O<sub>3</sub> and TiO<sub>2</sub> about 40 nm each serves as anti-reflection coatings (ARC) as well as protection against radiation from space.

The most important part of the used solar cell in this work is the AlGaAs/GaAs interface called heterojunction. The term heterostructure refers to two different materials with two different bandgaps.

The GaAs layer thickness is about 8 μm, the rest being a substrate and a bottom contact. As a substrate is used n-type germanium (triple or more junction PV cells use p-type Ge wafer – depends on solar cells design). Germanium is used mainly due to its very high mechanical strength. This parameter is important for the use in space by virtue of the production of very thin wafers and thus a reduction in weight and material consumption. The total PV cell thickness is about 135 μm.

## 4.2 Experimental methods

High demanding conditions were performed to simulate accelerated ageing. The selected solar cells were exposed to a wide range of temperatures and radiation at which their degradation is expected. This section then describes in detail the main four processing methods and how they were realized.

<sup>3</sup>The thin-films were observed using a transmission detector in Fig. 5.27.

### 4.2.1 Heating to high temperatures

Thermal processing was the relatively aggressive method, which can be simulated the difficult conditions and degradation of the samples. The heat sensor was placed approximately 2 mm from the sample, so it can be monitored the exact temperature in the vicinity. The entire process was automated. The temperature was set to 350 °C. The required furnace temperature rose from 23 °C during 30 min. Subsequently, it was stabilized for 240 min. After that, next 30 min program waited as soon as it dropped back to room temperature of 23 °C. During the thermal processing, the stress temperature of 350 °C was chosen as a limit value that, for the period of 240 min, the solar cells were able to withstand and continue to operate without complications. Thanks to that high temperature it is more distinctive to observe the degradation and processes occurring both on the surface of the cell and its electrical properties. These processes in such a short time of thermal stress and room temperatures may not always be measurable. All the measurements did not take place during the processing but before and after it. Processing was performed in the air at normal atmospheric pressure. Slight oxidation can be expected.

### 4.2.2 Cooling to low temperatures

Sample cooling was performed in a sample analysis chamber (SAC) of the XPS setup under vacuum  $<5 \times 10^{-7}$  Torr ( $<6.66 \times 10^{-5}$  Pa). Thus, no undesired oxidation or condensation occurred. Dry nitrogen was used as the coolant. The temperature was controlled using the temperature control unit (TCU), which was an original part of the XPS system. The solar cell was placed on the sample holder in good contact with the cooled molybdenum plate. In the excitation setting, the emission current was set to 15 mA for all measurements.

The sample cooling process proceeded in several ways. The first method was cooling to a specific temperature and subsequent in situ measurement of the XPS spectrum at that given temperature, as described in Fig. 4.3. There were 8 measurements, which represent points A to H. For the accuracy of the measurement, all points in one measurement cycle were performed from one surface location and one solar cell. First, the sample was gradually cooled in the order of 23, -10, -40, -70 and -100 °C. The aim was to observe the behaviour of the sample and its elemental composition during a constantly decreasing temperature. It can also be seen from the figure that the measurement started only after the temperature stabilised. Thus, the temperature was set, and after reaching this temperature, another hour waited, and only then was the XPS measurement started. After completing the measurement, a further temperature change step followed. The lowest temperature in this measurement method was set to -100 °C. Then, the temperature was

increased stepwise in steps  $-100$ ,  $-70$ ,  $-40$  and  $23$  °C. This method aimed to determine whether the state of the sample returns to the previous point before cooling or whether the state of degradation is permanent. The whole measurement following these steps lasted for 15 hours.

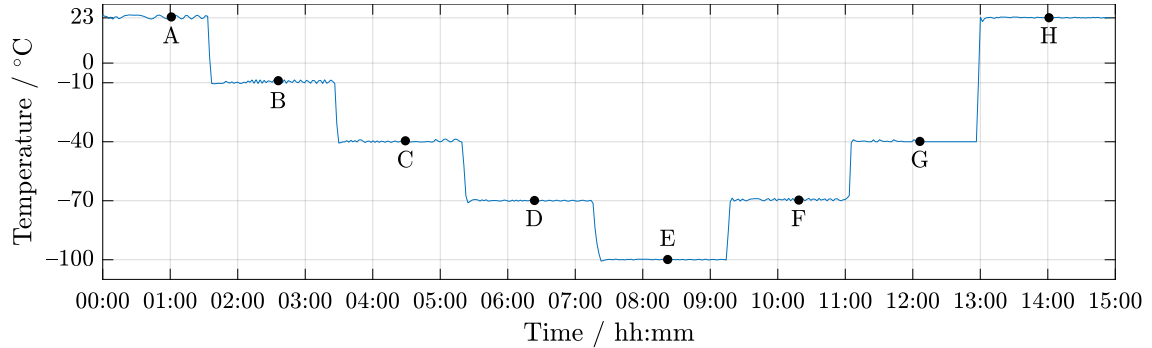


Fig. 4.3: The exact cooling process of one cycle of solar cell measurement using XPS is described by letter from A to H. A total of eight measurements were made during this process. The aim was to examine the state of the solar cell at decreasing temperature and whether the solar cell can return to its original state after the completion of the cycle. During each measurement, several essential elements in the high resolution were examined.

Another way of measuring in SAC using XPS was in situ measurement with a temperature change from  $23$  °C to  $-120$  °C, and back to  $23$  °C. Compared to the previous method of measurement, this type of measurement lasted a total of 7 h. The solar cell was cooled to  $-100$  °C in 1 h and to  $-120$  °C in 2 h. Subsequent return to temperature of  $23$  °C took 20 min, as described in Fig. 4.4.

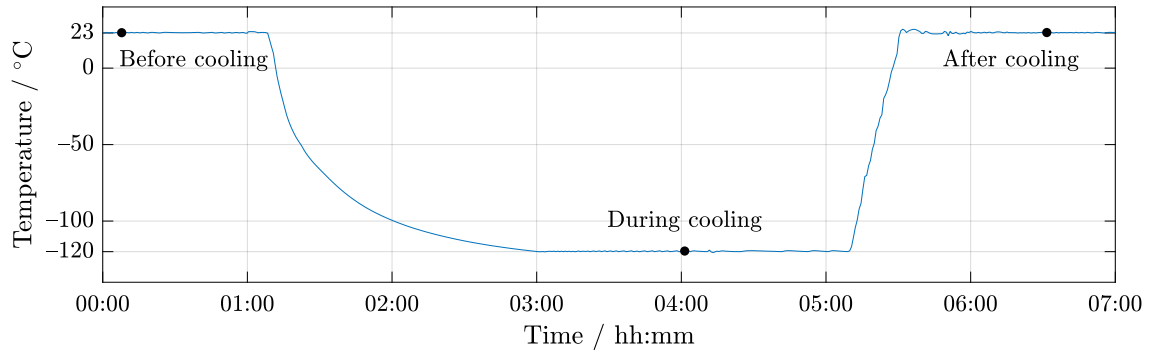


Fig. 4.4: The temperature curve measurements in relation to time during rapid cooling. A total of three measurements were made during this process. XPS was performed before cooling, during  $-120$  °C and after return back to room temperature.

As in the previous case, after reaching the target temperature point, an hour was allowed for the sample to stabilize. It is thus clear that the sample was exposed



to much more demanding conditions. The aim was to compare these two methods of measurement with each other and what effect it has in terms of elemental composition and degradation on the solar cell.

Solar cells before and after cooling were also evaluated using other methods such as Raman spectroscopy, reflectance and electrical properties of the cell. This evaluation was already performed at normal air condition (23 °C) and pressure (101 kPa). In this way, not only the thin-films but also the overall performance of the solar cell were examined.

### **4.2.3 Irradiation with gamma rays**

Cobalt-60 isotope with energies of 1.17 MeV and 1.33 MeV and current activity of 380 TBq described in Sec. 3.3.2, was chosen as a emitter. A dose of 500 kGy was applied for irradiation of the PV cell. The irradiation was performed in the cobalt-60 irradiation facility in Roztoky, Czech Republic at a standard air condition and room temperature. Within 21 days of continuous irradiation, it was simulated exposure by accelerated ageing, which typically occurs within a many years. Several tens of solar cell samples were irradiated at a direct distance and without any additional shielding from the emitter.

To illustrate, the dose of gamma radiation when the astronauts stayed on the Moon during Apollo mission was approx. 500 mGy. Another example illustrated the very first measurement of radiation on the Moon published in 2020 when the average dose rate in silicon of 13.2  $\mu\text{Gy/h}$  was measured [62]. This dose was measured by the Chinese lander Chang'e 4 on the Moon's far side.

### **4.2.4 Irradiation with broadband light source**

Supercontinuum laser (SL) used for experiments is a Leukos Samba 450 optical system with a measured spectral range of 450 nm to 2400 nm and the total average power output 188 mW without collimator. For a basic idea of power at a given wavelength, spectral power density from manufacturer is illustrated in Fig. 4.5. The system is capable of operating in single mode and multimode, the latter being needed for full-scale spectrum coverage.

The samples were exposed to radiation during 67 days at a distance of 67 mm. The laser power was set to maximum 188 mW. Spot size is 5.73 mm<sup>2</sup> at the 200 mm<sup>2</sup> square samples. No cover glass to the solar cells and no bias were applied.

The SLs combine the efficiency, power and coherence of lasers with broad-spectrum coverage of conventional broadband light sources while being able to exceed their brightness by several orders of magnitude without losing the option of being used for delicate optical microscopy applications. Currently, they are a unique

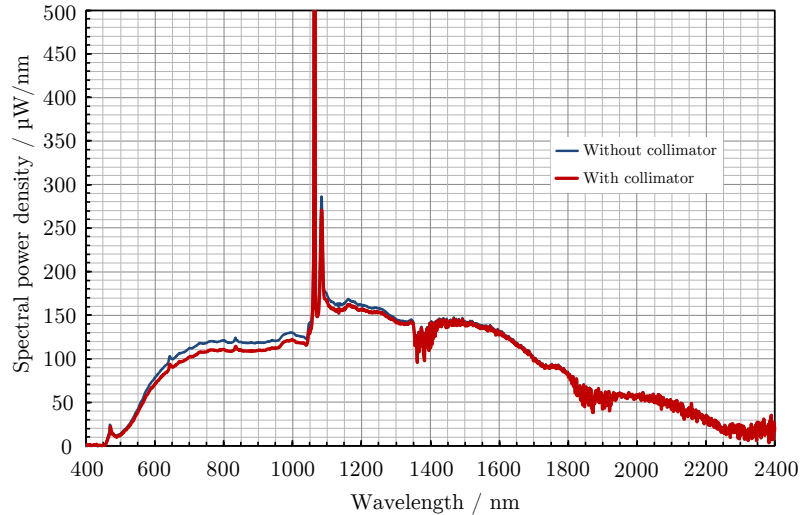


Fig. 4.5: Declared spectral power density depending on wavelength for SL.

technology, providing high power and the broad spectrum of light with very short pulse duration. They are used for a wide variety of purposes, especially in medical and biological fields. Applications of SL include, but are not limited to, fluorescence lifetime imaging and confocal microscopy, optical coherence tomography, measurements within plasmonics and metamaterials, carbon nanotubes, quantum dots and others. The properties of SL are a huge asset in many fields, using its coherent white light as a source for optical coherence tomography [63], optical communication [64], or a probe for excitation in chemistry and biology [65], to name a few.

### 4.3 Examined properties of the solar cell

Based on the knowledge of the methods listed in Sec. 3.4, it was possible to characterise the material, making it better to understand its behaviour after such strong temperature stress and radiation processes. It was thus possible to examine the optical, morphological, and electrical properties of the solar cell and determine which parameters correlate with each other or the differences between them and between the used processing methods. For easier orientation in the experiments, Tab. 4.1 summarizes and assigns all performed measurements<sup>4</sup>. The exact types of devices used are listed in Sec. 5.5. The table does not include a column for monitoring fabrication defects which are created during production in Sec. 5.1, as this is not essentially the processing method originated in this work.

<sup>4</sup>In the electronic version of the document, clicking on the checkmark ✓ redirects to the text of the given measurement.

Tab. 4.1: A brief overview of the analysis and measurement of GaAs based solar cell.

Instrument / analysis	Thermal processing	Cooling	Gamma irradiation	Laser irradiation
AFM	✓		✓	
SEM	✓		✓	
EDS	✓			
EBIC			✓	
Raman spectroscopy	✓	✓	✓	✓
XPS		✓	✓	✓
FTIR			✓	
Elipsometry			✓	
Reflectance		✓	✓	✓
Infrared camera	✓			
SIMS			✓	✓
Electroluminescence			✓	
Dark I-V characteristics	✓	✓	✓	✓
Light I-V characteristics	✓	✓	✓	✓
PSD	✓		✓	

### 4.3.1 Structural morphology and material properties

Surface morphology was investigated using atomic force microscopy and NTEGRA Prima microscope. The aim of this measurement was to track changes in surface topography in the order of units of nanometres. A semi-contact mode with single crystal silicon NSG01 probes was chosen. Probes have a curvature radius of the tip of 10 nm. Average scan rate was 8.04  $\mu\text{m}/\text{s}$  for all measurements before and after thermal stress and gamma irradiation. Several structure areas were scanned to reduce the probability of random formations like spikes and unusual objects.

Roughness analysis with several important surface parameters was also provided for better orientation in surface parameters. The cell surface was summarised in a histogram of the so-called features, representing a typical bell curve shape. Features are in roughness analysis called surface irregularities. The average height of features from the scanned area of  $10 \times 10 \mu\text{m}$  was selected as a parameter describing surface morphology; average roughness  $S_a$  describing the total topology scale; skewness  $S_{sk}$  and kurtosis  $S_{ku}$  parameters represent a deviation from the normal distribution of all measured height points.

For SEM observation after thermal stress, solar cells and its contacts were imaged by backscattered electrons (BSE) detector on 120  $\mu\text{m}$  view field at 15 kV accelerating

voltage. Using EDS, it was performed an elemental microanalysis of the sample surface (not contact) at an accelerating voltage of 22 kV. This method analysed the surface appearance and composition without any special preparation of the samples (cleaning or metallisation). The duration of the EDS analysis was 60 min. The used electron microscope was Tescan's LYRA3 with X-Max 50 EDS detector from Oxford Instruments.

Although the effects of intense gamma irradiation that have been applied can have a severe and visible impact on the material, scanning transmission electron microscopy was performed for detailed analysis and understanding of radiation effect. The STEM detector was chosen for a very detailed inspection of the sample structure across several  $\mu\text{m}$  in depth. The structure was examined before and after irradiation. The lamellas with a thickness of 15 nm were prepared, and the GaAs layer was examined. For this purpose, FEI Helios NanoLab 660 microscope was used to conduct examination. This microscope was used for both lamella preparation and STEM detection system observation. Bright-field (BF) mode has been selected for image generating. Generally, this is one of the most used observation modes. An unscattered electron beam is selected by objective aperture, and scattered electrons are excluded. Surface areas, where are electrons absorbed, appears to be darker. Where are the electrons transmitted from the area, appears to be brighter. During the observation, the high voltage was set to 30 kV and the current to 80 pA.

Elemental and molecular information about the sample was given by Time-of-Flight (TOF) SIMS using instrument IONTOF TOF-SIMS 5. For this analytical technique, a solid surface is bombarded by primary ions. Collision cascade is generated after the primary ion energy is transferred to atoms via atomic collisions. Resulting erosion speed differs on various factors such as material type or sputtering energy. For the excellent mass resolution, it can be  $<0.1\text{ nm}$  per min. Main investigated peaks are:  $\text{Ga}^+$ ,  $\text{Al}^+$ ,  $\text{Ti}^+$ ,  $\text{As}^+$  and  $\text{O}^+$ . These elements appeared mainly in the form of positives ions, so the measurement was done in positive mode. As a primary beam, a ions of  $\text{Bi}_1^+$  with the energy of 60 keV was chosen. As a sputter beam, a reactive species of Cs with the energy of 2 keV and  $100 \times 100\ \mu\text{m}$  crater size were used. The same SIMS setting was used for the gamma irradiation and the supercontinuum laser method.

The surface sample before and after the thermal stress was showed using an infrared camera. The picture shows a thermal difference of  $0.8\ ^\circ\text{C}$ . The type of used camera was Micro-Epsilon TIM 160 with a resolution of  $160 \times 120\ \text{px}$ . The specimen was connected to the Agilent E3649A power supply and set the value of 7.3 V under reverse-biased condition. In this way, the exposed location on the sample could be observed. The current flowed through the sample for 3 s. After that, an image was taken, and the circuit was disconnected for another 3 s for the sample to cool off.

This process was performed 480 times and all images were averaged to eliminate the noise and other image errors.

Electroluminescence served as the next method for defects detection of irradiated specimen by gamma rays. A cooled G2-3200 Mark II camera from Moravian Instruments was used for imaging a low light source for this purpose. The camera uses Kodak KAF-3200ME full-frame CCD sensor with high quantum efficiency and linear light response. The sensor has a resolution of  $2184 \times 1510$  of photoactive pixels and  $14.85 \times 10.26$  mm of active imager size. The camera, along with the sample, was in a darkened box. The sample was measured in the forward and reverse current. Keithley 6220 was used as a very sensitive current source.

Raman spectroscopy was performed to control the presence of structural defects and free charge carriers. Considering the relative intensity of localized vibrational modes provides information about nature of the defects. Confocal Raman imaging for all realised methods<sup>5</sup> was obtained by WITec alpha300 R system. The experiment was performed using objective 100 $\times$ , exposure time was 7 s and the number of accumulations 20. A green laser of 532 nm as the light source was set to 5 mW for thermal stress, cooling and SL irradiation method, but for gamma irradiation 15 mW power was selected.

Depth measurement has been used, which in this case, is desirable for collecting information about the specimen. The deep profiling measurements for gamma irradiation method were made to a depth of 5  $\mu\text{m}$ . From the center of this depth, accordingly 2.5  $\mu\text{m}$  up and 2.5  $\mu\text{m}$  down. The area was measured as a 5  $\mu\text{m}$  line<sup>6</sup>. Three spectral regions, which are about 800 nm above each other, were taken from this depth measurement. The middle area was chosen within the strongest GaAs TO mode. For a better explanation, pictures with the color-coding occurrence of the spectrum as a cross-section were published. By another Renishaw inVia spectrometer was measured results confirmed.

Examining the elemental composition on the surface has also been preformed using X-ray photoelectron spectroscopy for the precise and exact definition of the chemical bonds on the surface. Survey spectra were taken with the following parameters: monochromatic XPS source with emission current of 15 mA, spectra between 1200 eV to 0 eV and step of 1 eV. The wide spectrum was always measured on each sample as the first part to give an idea of the complete elemental composition on the sample surface. From the resulting wide spectrum, the regions that were most interesting and important for the given sample within its processing were then identified

---

<sup>5</sup>This measuring method was performed only for samples processed by second cooling process to  $-120^\circ\text{C}$ . As this is a more aggressive method, larger changes are expected.

<sup>6</sup>Raman spectroscopy is most commonly measured in spots, but for this measurement, it was performed in the line.

by elemental binding energy. The spectra has been swept several times for higher accuracy (several identical consecutive measurements). The studied elements were carbon, oxygen, aluminium and titanium. All the XPS spectra were calibrated to the carbon peak of 284.6 eV. Method was used for cooled, gamma and SL irradiated specimens.

Spectral features of both FTIR and ellipsometry spectra are complex since they were taken in reflection mode. They contain information about layers forming an anti-reflection coating, PN junction, and substrate. Therefore, this data illustrates the changing of thickness according to the different distances between interference maxima.

Ellipsometry was measured by NIR-UV spectroscopic ellipsometer J.Å. Woollam V-VASE (WOOLLAM-VIS). Hyperion 3000 FTIR microscope was used in reflection mode for the collection of spectra. The spectral range of FTIR was chosen from  $4000\text{ cm}^{-1}$  to  $1000\text{ cm}^{-1}$ .

### **4.3.2 Optical properties**

Reflectance spectra were measured in the range from 200 nm to 1000 nm. The spectrum of ultraviolet light (UVA) in the range of 200 nm to 380 nm, visible light (VIS) in the range of 380 nm to 740 nm, and near-infrared light (NIR) in the range of 740 nm to 1000 nm were measured. All these three measurements were realised by Optical Spectrometer Ocean optics JAZ 3-channel. The solar cell was irradiated with light, which is partially absorbed by sample. A thin gold-coated wafer was used as the calibration sample. This non-destructive contactless method provides rapid evaluation of properties, including doping of the materials. Reflectance measurement method was used before and after cooling<sup>5</sup>, gamma irradiation and supercontinuum laser irradiation.

### **4.3.3 Electrical properties**

All dark and light electrical characteristics were measured before and after all conducted methods<sup>5</sup> at temperature of 25 °C. During the measurement of I-V characteristics under illumination, a standardised light source calibrated to an output of  $1000\text{ W/m}^2$  was used to simulate sunlight activity. From the characteristics of illumination was also calculated P-V characteristic with the maximum power point. As a measurement system unit was used NI PXIe-1073 with the PXI-4130 SourceMeter and the PXI-6224 data acquisition module. This module can measure voltage, current, temperature and other electrical or physical parameters depending on the peripherals connected.

The dark I-V measurement setup consisted of a shaded and darkened box with a Keithley 2510-AT AUTOTUNING TEC SourceMeter with an automatically controlled temperature. The Peltier plate with a water-cooled radiator was controlled and maintained by a temperature system. For measuring the characteristics the computer-connected Keithley 2420 power supply was used. Electrical characteristics for irradiation with SL were taken for five exposure sessions in order to study changes in performance – before the irradiation, and after 7, 20, 32, 42 and 57 days<sup>7</sup>.

Noise current spectral density  $S_i(f)$  was measured from 1 Hz to 1000 Hz range. It is a non-destructive spectroscopic analysis for the study of noise fluctuation and transport mechanisms. As the supply wiring, it was used double-shielded coaxial cables with Agilent E3631A power supply. Noise signal was detected at the end of the circuit closed by a  $5.517 \Omega$  resistor. Rohde & Schwarz FMU36 high sensitivity baseband analyser was used. This device for analogue and digital baseband signals can analyse extremely weak signals at low frequencies. Wired signal to the analyser was amplified using the ultra-low noise preamplifier Ametek, model 5184. Noise fluctuations were measured in reverse-bias at voltage levels which corresponded to the knee of the I-V characteristic.

---

<sup>7</sup>Please note that the whole experiment with SL took 67 days, as mentioned in Sec. 4.2.4, but electrical measurement took 57 days.

## 5 Experimental results

The experimental results below show the changes and degradation of GaAs solar cells. The chapter is divided according to selected experimental methods in Sec. 4.2. A subsection examining the expected degradation that occurs during the fabrication and handling process has also been added. For each experimental method, the observation was chosen by such an instrument, which would be the most suitable to analyse the manifested changes.

### 5.1 Mechanical stress and fabrication defects

For the illustration, Fig. 5.1 and Fig. 5.2 showing the GaAs solar cell do not overlap each other, so the difference between SEM and EBIC is apparent. This pair of Fig. 5.1 and Fig. 5.2 represents the layer with PN junction and the silver contact of the solar cell. Delamination is already noticeable from Fig. 5.1, but for Fig. 5.2 the accurately damaged and delaminated parts are clearly visible. Variation of bias allows investigation of the structure. It can be observed that the distribution of carriers close to the contact is different.

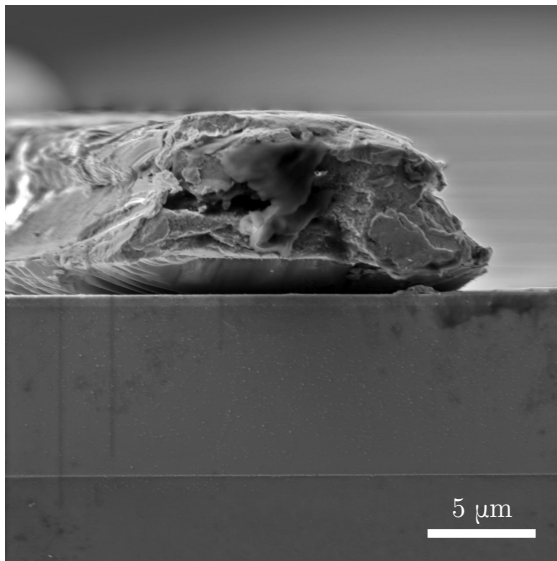


Fig. 5.1: Image of cross-section of a GaAs solar cell and its contact from SEM without applying the EBIC method.

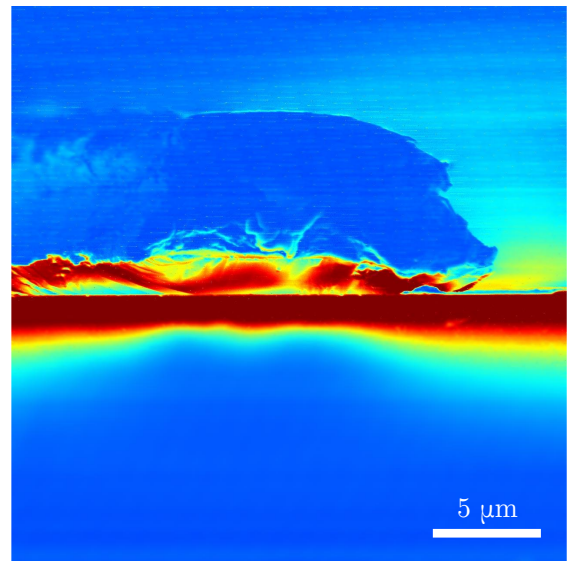


Fig. 5.2: Applied EBIC method on the solar cell shown in Fig. 5.1 without SEM image overlay. Area is the same. The exact charge distribution and PN junction can be seen.

The next measurement was performed on the GaAs solar cell where Fig. 5.3a shows the connected PV cell using nanomanipulators in cross-section mode as described in Sec. 3.4.2. The electron beam-induced current is not applied to the cell



(Fig. 5.3a–c) and measurement has proceeded only with SEM microscope. While observing cell with a larger magnification (Fig. 5.3b) its top contact is visible which is guided longitudinally relative to the image and it touches the upper nanomanipulator. However, this nanomanipulator is beyond the visible area from Fig. 5.3b.

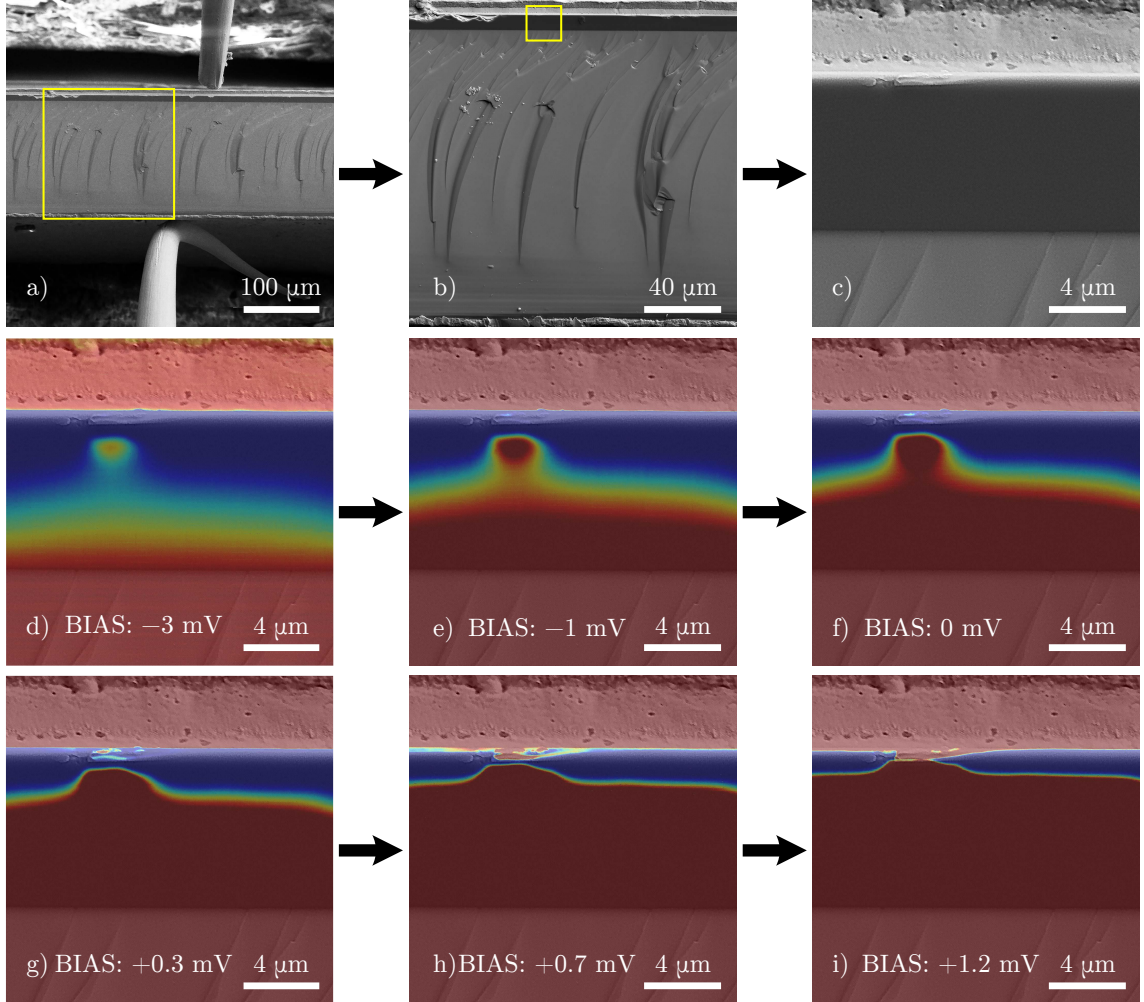


Fig. 5.3: Electrically active impurity near the junction of GaAs based solar cell in cross-section mode. Images a–c show the subsequent focus on the area of interest, followed by other images d–f where the EBIC method is applied and gradually increased bias from  $-3$  to  $1.2$  mV.

The full cross-section of the solar cell is now completely visible where is the predominantly germanium serving as the substrate. On the target area where the GaAs layer lies (Fig. 5.3c), the difference of the carriers can be seen when applying the EBIC method (Fig. 5.3d). Starting with this image, all other measurements are done using the EBIC method and the images shown by the SEM microscope are slightly overlaid with the coloured EBIC picture. Also from Fig. 5.3d an electrically active impurity is visible in this layer. The origin of these impurities is not clear but most likely, this impurity is fouled during fabrication. During the subsequent

increase in the bias from  $-3$  to  $1.2$  mV, which represents Fig. 5.3d–i, it is evident that thanks to this, impurity begins to appear tunnelling of charge carriers. It is also important to mention that this is not a permanent condition, and there is no permanent damage after the biasing is reduced. As the bias increases further, the potential barrier begins to decrease and due to the influence of impurity it becomes to tunnelling from the bias voltage of  $1.2$  mV. Electrons may then tunnel from one material to the other giving the significant rise to a current.

The EBIC showed that no structural defects in the form of long longitudinal cracks leading to inactive parts occurring on the surface of the GaAs cell were observed on any sample. Conversely, for silicon solar cells, this is a relatively common problem, along with point defects. Below, from the EBIC measurement results in the set in Fig. 5.4 a silicon solar cell (mc-Si) placed on the holder with a conductive carbon tape can be seen. The connection with the nanomanipulators was through the top contact of the cell and through its holder. If the PN junction is not ideal and contains some resistive impurities or leads, the induced current may decrease. Fig. 5.4b shows the contrast between the silver contacts and the silicon surface, and the induced current between the two interfaces. It can also be seen that the cell surface is not completely homogeneous and indicates the occurrence of various failures and other impact of degradation and impurities.

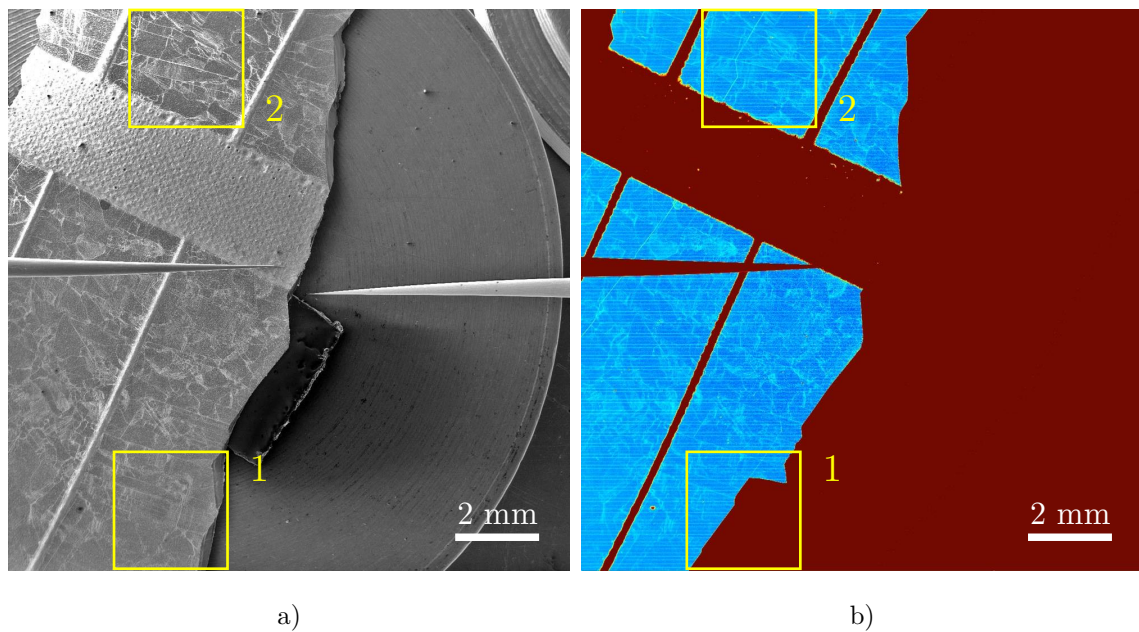


Fig. 5.4: Silicon solar cell scanned by a) SEM microscope using b) a coloured EBIC method.

Two points of interest, which are marked by a yellow frame, can also be noticed in the picture. If we focus on frame number 1 and compare its contents between Fig. 5.4a and Fig. 5.4b, it can be observed the completely inactive part of the solar

cell surface, which is presented by EBIC by a strong cut. However, this part of the surface is not visible in Fig. 5.4a from SEM at all. The second yellow frame with the number 2 then represents the Fig. 5.5 for better illustration. In addition to the small impurities on which the white circles show a subsurface crack can be observed across the cell surface, which is also not evident from the first Fig. 5.5a. These cracks resulted in multiple parts of the solar cell, and their uniformity and rare appearance confirm that they cannot be confused with grain boundaries.

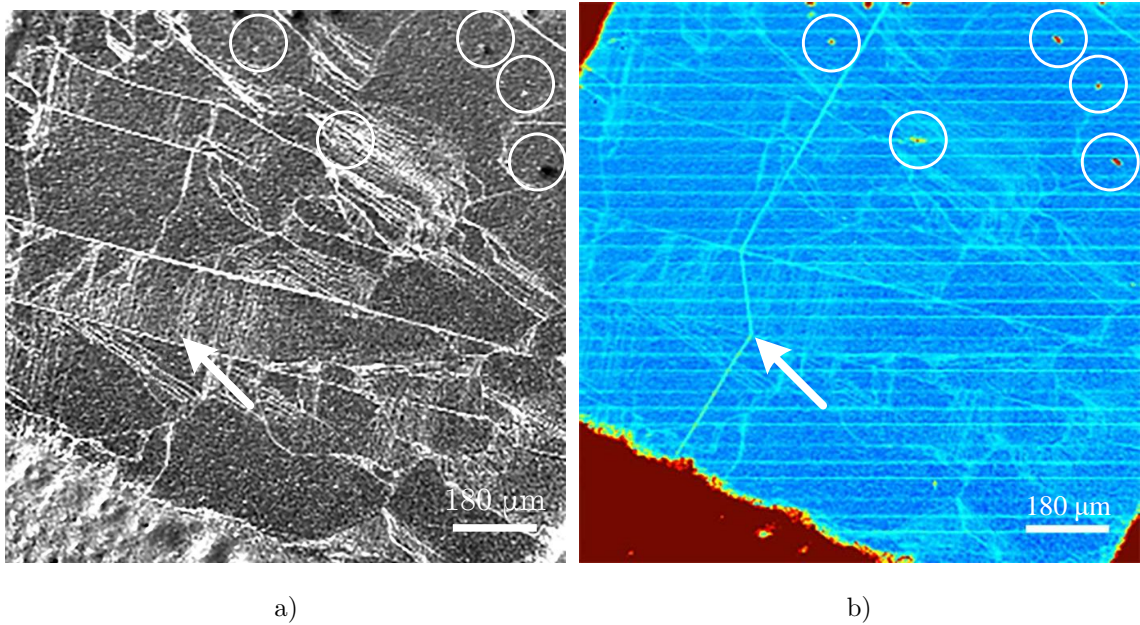


Fig. 5.5: Detail of the solar cell surface and b) one of the subsurface and other defects measured by coloured EBIC which cannot be clearly seen in figure a) from electron microscope.

## 5.2 High-temperature processing

During 350 °C temperature a slight degradation in GaAs cell was observed. It has been verified that if the temperature was raised up to 420 °C, nearly 90 % of the measured samples were no longer functional within 30 min. The loss of their functionality has manifested itself in the form of an electrical breakdown.

Atomic force microscope showed with no exceptions and in all cases, the more indented surface structure of the cells after processing. Differences can be seen on the non-annealed specimen in Fig. 5.6a as compared to the annealed sample in Fig. 5.6b. These figures also show the structure in both the 2D and the 3D imaging. Such a structure may, in some cases, influence a better absorption and less reflection of light, thus gloss of the photovoltaic cell. Slight growth of features of an average height of 15.73 nm is observed after processing. That is the change over 8 nm compared to



the non-annealed characteristics of an average height of 7.16 nm in Tab. 5.1. The histogram also demonstrates a clear pattern of surface features in Fig. 5.7, which confirms their growth after stress [66]. The processing thus influences the course of degradation.

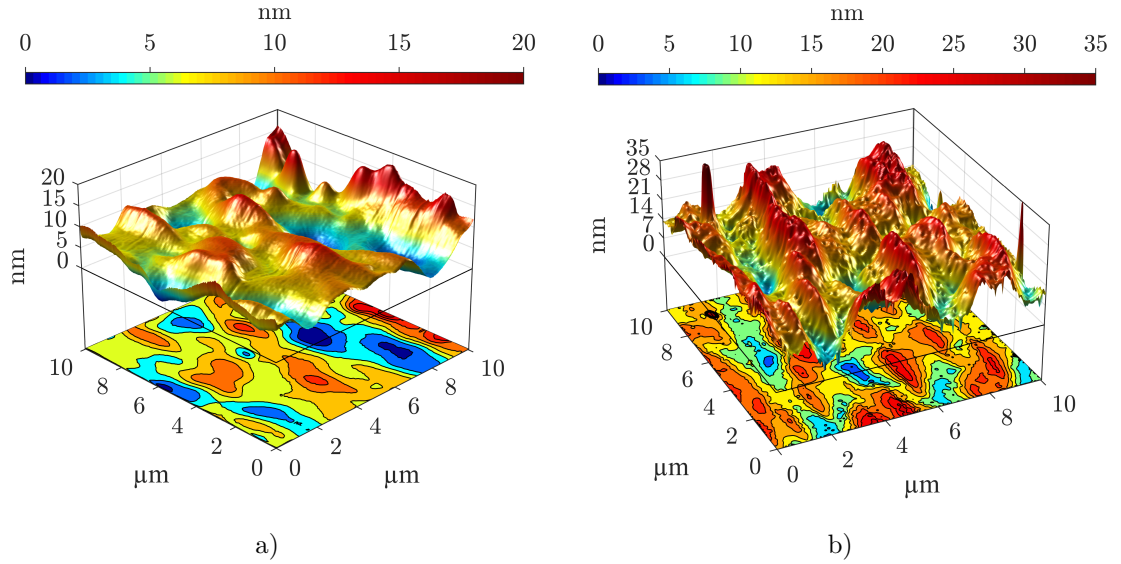


Fig. 5.6: Solar cell a) before and b) after thermal processing scanned by AFM. The picture in 2D shows the contours of the surface model in 3D for better clarity. Heights are colour-coded. At first glance, height and structural differences can be seen between figures a) and b).

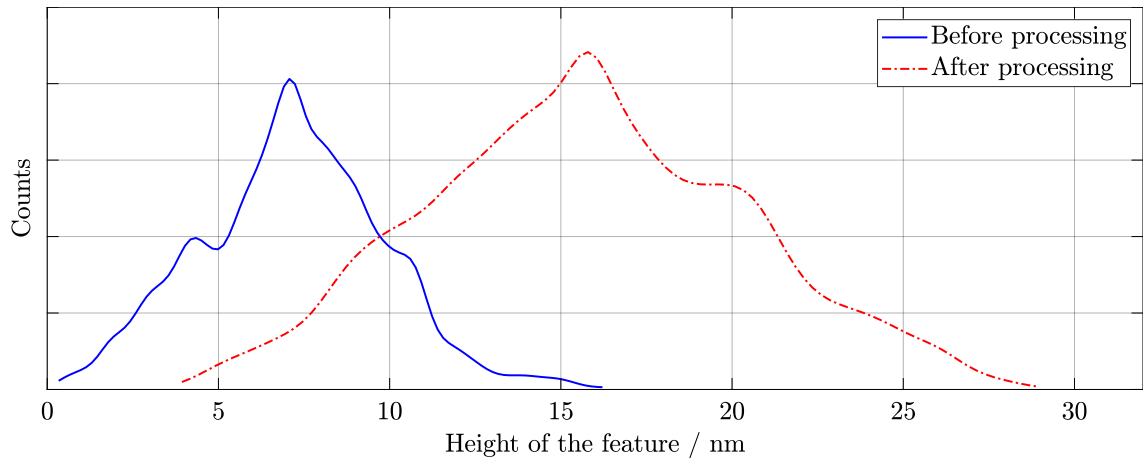


Fig. 5.7: Histogram of heights before and after thermal processing scanned by AFM. Depending on the height distribution, higher structures are visible on the processed sample.

There were also evaluated  $S$  parameters of average roughness ( $S_a$ ), surface skewness ( $S_{sk}$ ), and coefficient of kurtosis ( $S_{ku}$ ). An increase of  $S_a$  after processing also

confirms the more rugged structure and on the contrary the decreasing parameters of  $S_{sk}$  and  $S_{ku}$ , signifying larger symmetry and surface changes.

Tab. 5.1: Surface roughness parameters for thermally processed PV cells.

	Average height / nm	$S_a$ / nm	$S_{sk}$ / -	$S_{ku}$ / -
Before processing	7.16	2.133	0.133	0.085
After processing	15.73	3.781	0.132	-0.227

In Raman spectroscopy, the bonds that were formed before and after the thermal stress can be evaluated. Thus, symmetry of the molecules and the individual vibrational movements strongly influences the appearance of these spectra.

Main area of interest of experimental Raman spectrum in  $170$  to  $700\text{ cm}^{-1}$  are two characteristic peaks on  $268$  and  $271\text{ cm}^{-1}$ . These peaks indicate the typical GaAs structure before and after thermal processing in Fig. 5.8.

The intensity change is visible on GaAs LO and AlAs LO main peaks, which indicates changes in structure of the material, formation of dislocations and the type of radiation-induced structural defects resulting from processing. It is the purity of the material that can be observed by the frequency of shift of a certain Raman line. Frequency shift between these spectra was approximately  $4\text{ cm}^{-1}$ , which can be considered as a relatively small change. The full pulse width at the middle of the maximum (FWHM) expresses the structural distribution. This is related to the life of the phonon reflected in sharper peaks that indicate better crystalline structure of the sample. The presence of defects in the sample structure will shorten phonon life and extend the peak.

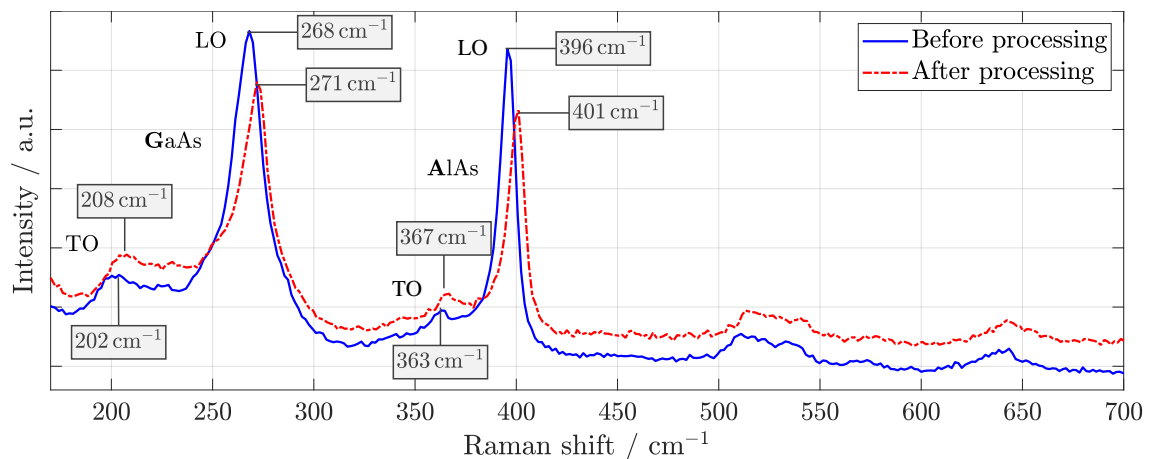


Fig. 5.8: Raman spectrum of GaAs sample before and after thermal processing.

At about 7 V in a reverse bias, it can be seen a break in the characteristic before processing in Fig. 5.9a. This significant change most likely indicates a defect. It can be holes in the surface, dislocations, microplasma defects, mechanical damage of the surface, inhomogeneity of the sample or melted zones. It is also possible to isolate the defects in a standard way using the focused ion beam, which also influences the shape of the I-V curve in reverse bias.

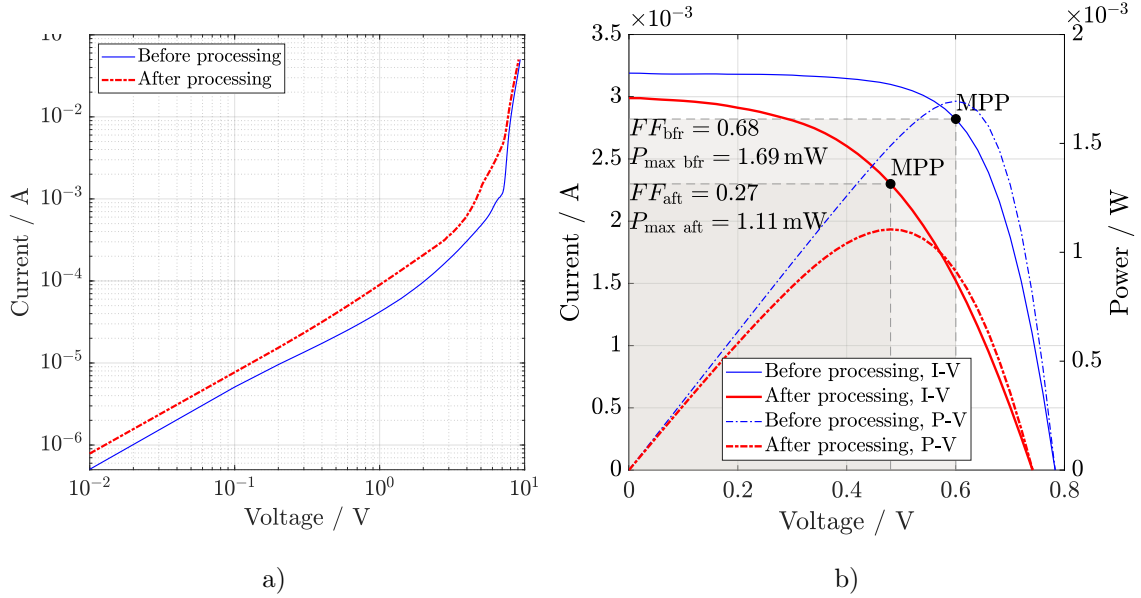


Fig. 5.9: Comparison of I-V characteristics before and after thermal processing. From the a) dark characteristic, a break can be seen, which represents a defect. A sharp decrease in power was observed from the b) light I-V curve.

The same break after thermal processing was not very noticeable, but the slope of the characteristic has declined. Processing temperature was so high that the properties of the solar cell could not be fully improved, even though it was short-term processing.

That is why the deteriorating electrical properties of the cell can be confirmed, which was verified even in the case of the characteristics under illumination. A reduced short-circuit current  $I_{\text{sc}}$  was observed from 3.19 to 2.99 mA and reduced open-circuit voltage  $U_{\text{oc}}$  from 0.78 to 0.74 V in Fig. 5.9b. The maximum working point (MPP) of the PV cell determined from the power characteristic has dropped after processing. As well as the maximum power  $P_{\text{max}}$  from 1.68 to 1.11 mW and fill factor  $FF$  from 0.68 to 0.27 have decreased.

Thermal radiation has appeared on several samples in other places than before after the thermal stress (Fig. 5.10). Moreover, the radiated places existing before the processing were no longer present. It is obvious that while some of the defects ceased to exist, other appeared instead. This is confirmed by dark curves in Fig. 5.9a in the

reverse bias, where the break on the curve after processing has changed. Deformation of the defect or its disappearance during treatment could lead to the different shape of break.

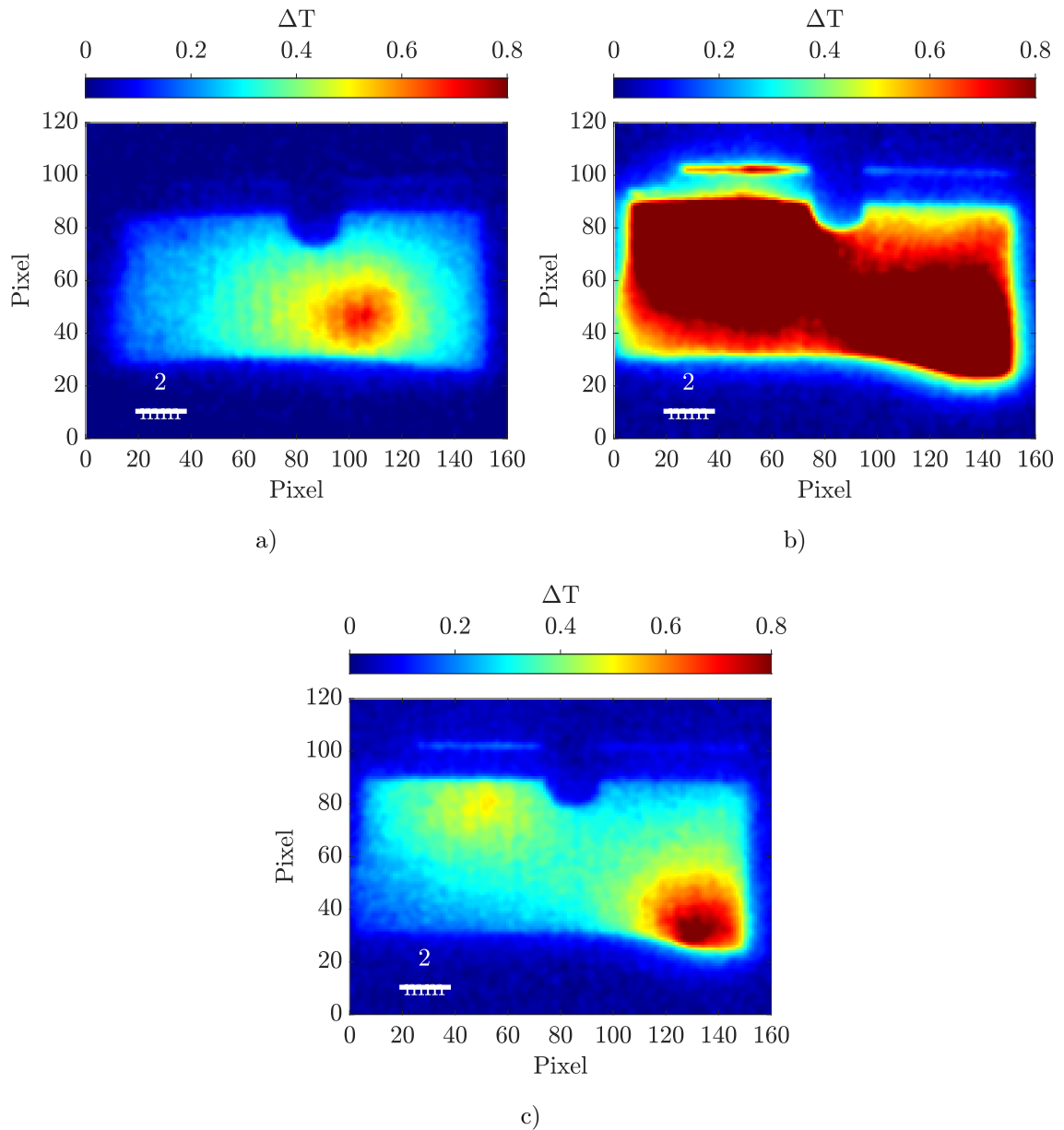


Fig. 5.10: Photovoltaic cell under infrared camera at a voltage of 7.3 V a) before and c) after the thermal processing and its heat-generating location. At the same voltage the difference compared to a cell a) before previous processing was very noticeable. The previous defects in several photovoltaic cells have disappeared. Conversely, different new defects arose after thermal stress. On the given sample in Fig. b), it was necessary to reduce the voltage to 5 V due to its degradation and better localization of stressed places.

Changes in defect dislocation were confirmed by infrared camera. It was also verified this by rotating and tilting the specimen and camera from different angles

to prevent camera reflection. This phenomenon can be seen in Fig. 5.10a–c, where after processing the stressed parts have been created in other places. In order for these new defected parts to be visible, it was necessary to reduce the voltage from the original 7.3 to 5 V. The influence of degradation was extensive so it could not be observed under the previous conditions.

Most of the other samples have already been manifested by the increasing intensity of radiation from the same area after thermal processing. This was the expected phenomena which can be attributed to the degradation of the cell.

Surface of the sample showed less signs of degradation. The contact on the cell was kept firm after processing. Its separation was not observed, and only moderate oxidation of the silver appeared. The differences are visible in Fig. 5.11.

During the high temperature stress of the given GaAs surface the atoms of silver can diffuse into the structure of semiconductor. It is a desirable aspect that can improve the electrical properties of the solar cell. Withal, it must be counted with the undesirable appearances that will change some properties of the semiconductor and the conductor thermally e.g. a degree of thermal expandability.

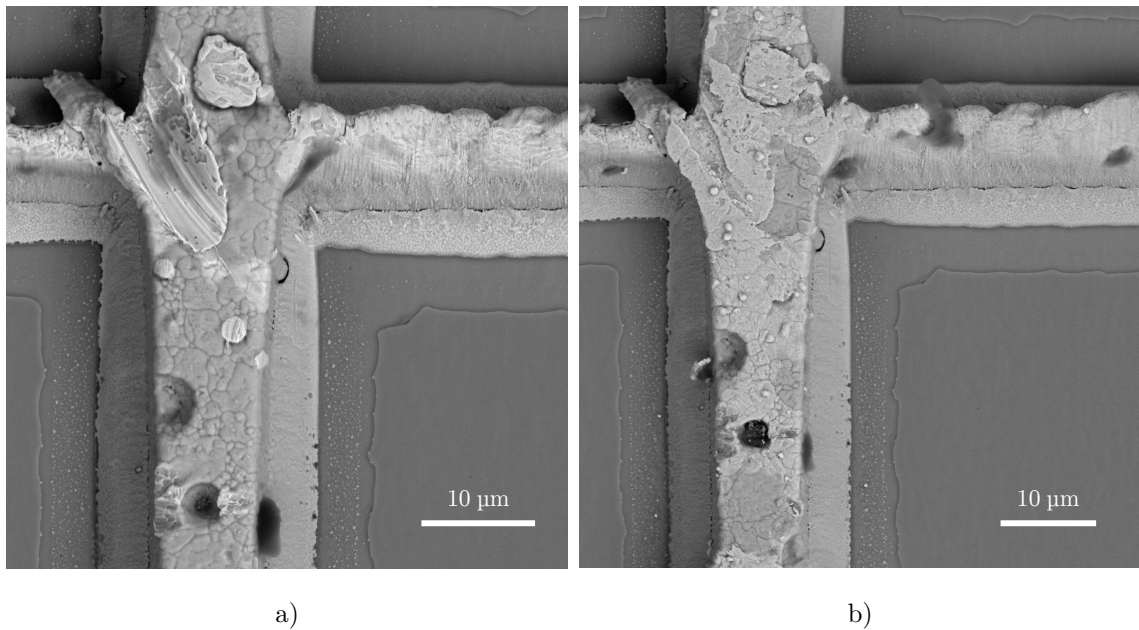


Fig. 5.11: The contact and surface of the GaAs solar cell scanned by SEM using a BSE detector a) before and b) after thermal processing. The GaAs solar cell exhibits slight changes in the form of oxidation on the surface of the contact after processing. Changes on the surface of the cell are not noticeable.

SEM investigated surface degradation of the contact. EDS was focused only on the GaAs surface and confirmed the excellent material stability. On the spectrum in Fig. 5.12, there are almost two overlapping curves with marked elements. The



weight of the individual elements and their comparison after thermal stress are also expressed as a percentage. For a broader overview, changes and differences in element distribution after processing are highlighted in Fig. 5.13. This is the subtract of EDS spectra before and after thermal stress. The difference in intensity was observed in the order of thousands of counts, which is almost negligible, as can be seen in Fig. 5.12. Similarly, there are weight differences of the elements from the additional bar graph in Fig. 5.13. Mainly loss of aluminium and titanium is observed.

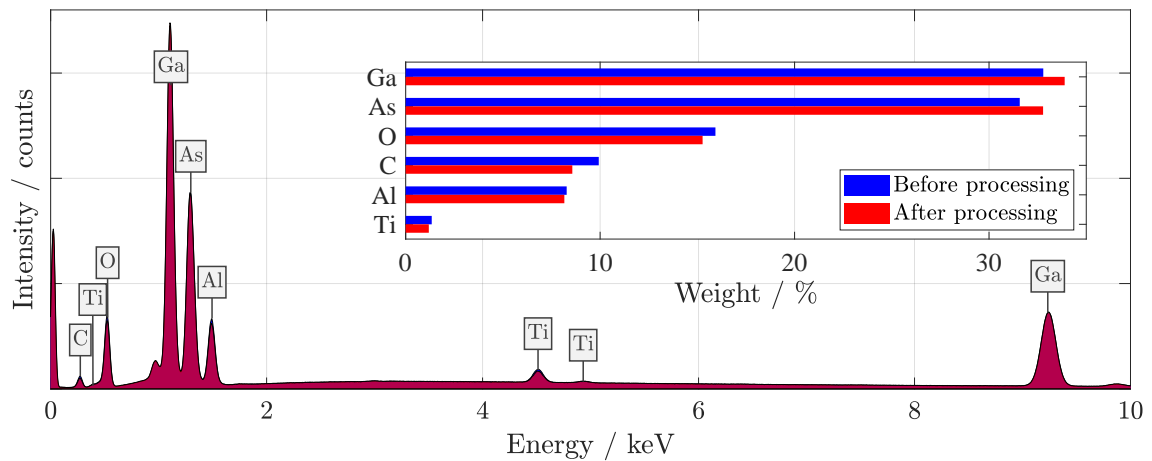


Fig. 5.12: Comparison of the elemental composition after thermal stress. The changes in the graph are negligible, so an additional bar graph quantifying these changes was plotted.

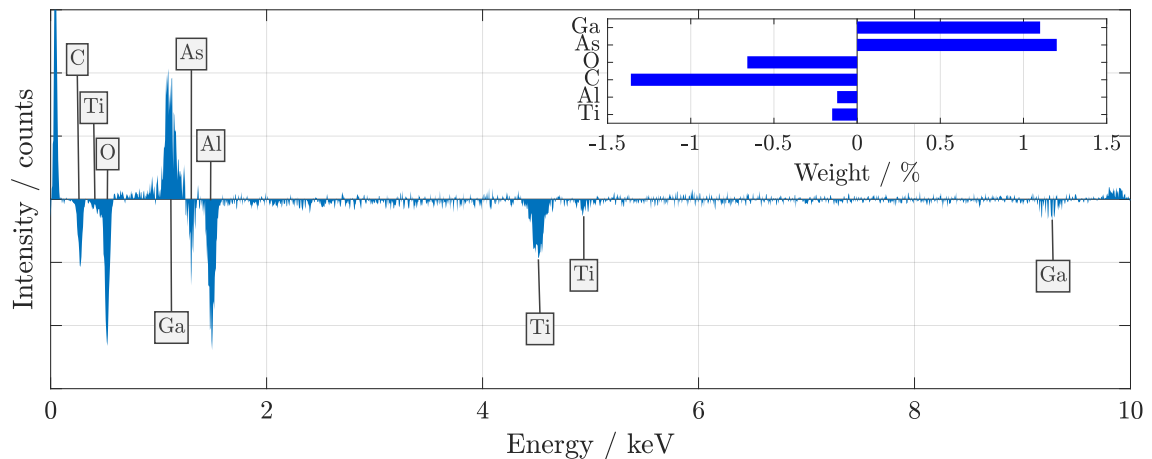


Fig. 5.13: Difference spectrum intensity in elemental structure of the cell after thermal processing.

Noise fluctuation measurements were indicated as the flicker noise which was described above in Sec. 3.4.8. The noise power is approximately inversely proportional to the frequency at whole spectrum. Along with increasing voltage, the noise spectra

magnitude grew with almost identical slope of the PSD after thermal processing in Fig. 5.14a.

Solar cell noise grew by almost one order and at higher voltages changed the slope to  $f^{-1.57}$  for the thermal treatment in Fig. 5.14b. It can be observed that, except for the voltage of 6 V, which is still in front of the knee of I-V reverse-biased curve, the noise at all remaining voltages shifted to a relatively uniform level. There are much smaller noise spectra magnitude ranges contrary to the noise before processing [67].

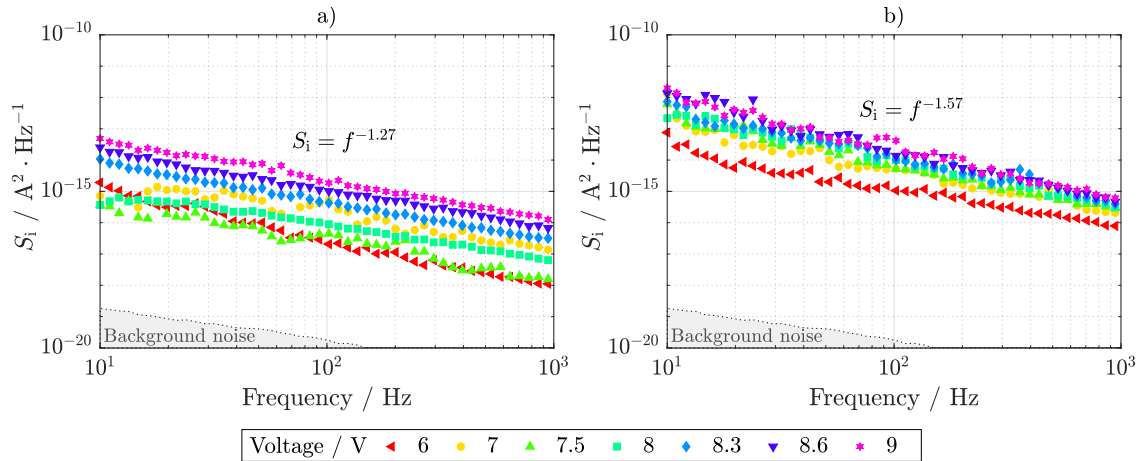


Fig. 5.14: Flicker noise is visible on all measured voltages. Curves with a voltage that extends behind the knee of the reverse-biased characteristic have a very similar character and the slope of index of 1.27 in figure a) before thermal processing. A smaller range and a higher noise spectra magnitude shift between the individual voltages and a greater slope with the index of 1.57 was observed b) after processing. This applies in particular to voltages above 7 V or higher.

### 5.3 Low-temperature processing

The reflectance spectrum of the solar cell after rapid cooling ( $-120^{\circ}\text{C}$ ) in Fig. 5.15 shows an almost unchanged character, mainly in the VIS and NIR region. The measurement curves clarify a minimal change in the structure of the surface, as its reflectivity is very similar to that before cooling, morphological analysis using AFM, therefore, appears to be unnecessary.

Sharp peaks of specific longitudinal (AlAs LO) and transverse (GaAs TO) optical modes in Fig. 5.16 express the well-preserved crystalline structure even after cooling. The composition of these peaks shows a slightly different ratio in the form of (GaAs TO):(AlAs LO) after cooling. Ratio results in the difference of 1.449:1 compared to the previous 1.847:1.

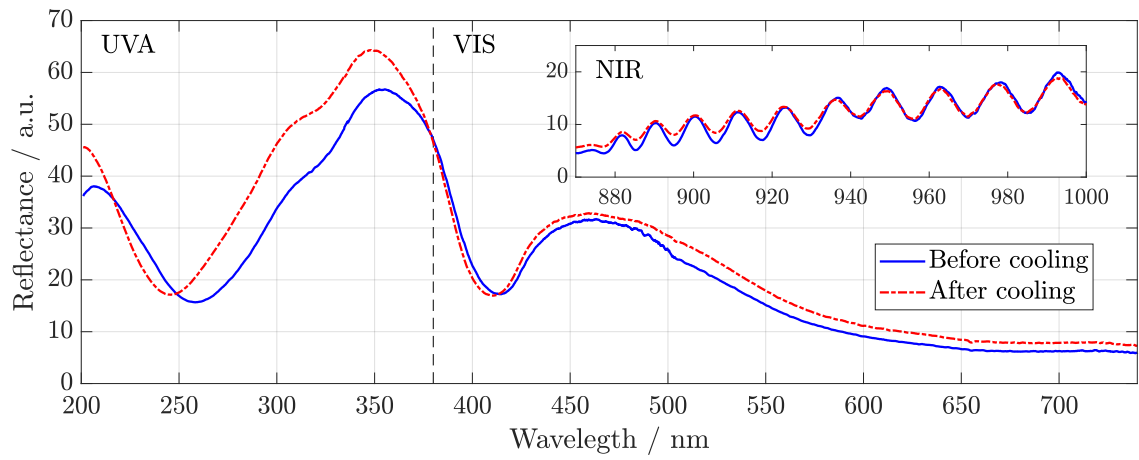


Fig. 5.15: Differences in reflectance after cooling. The excellent resistance of thin layers and surface to low temperatures is shown.

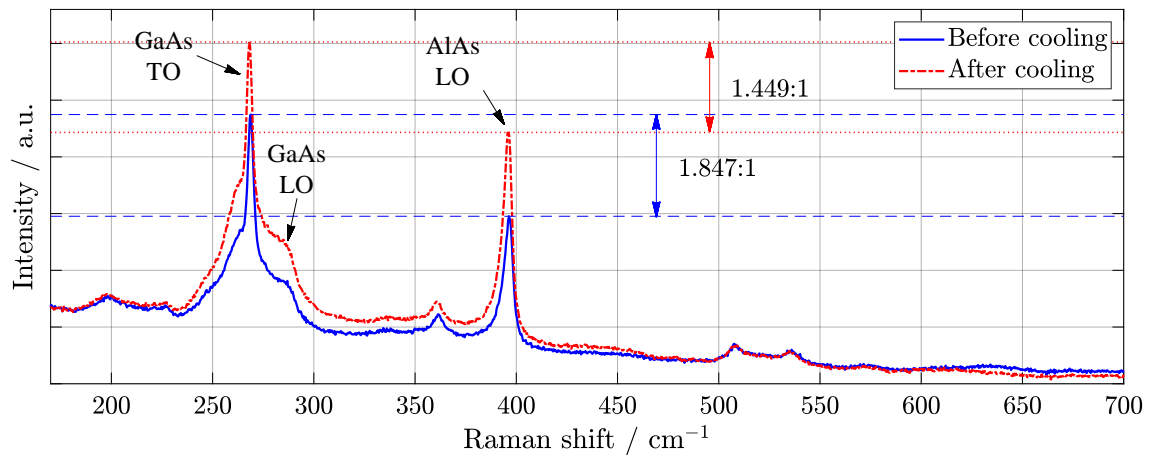


Fig. 5.16: Raman spectroscopy curves after cooling. Growth of peaks after cooling and a slight increase in AlAs LO mode are observed.

Although the previous results of optical properties and Raman spectroscopy gave relatively unchanged characteristics before and after cooling and the GaAs cell appeared stable, the elements were examined by XPS during cooling for this purpose. Because of the extensive amount of measurement, results from XPS have been moved to the appendix (Fig. A.2–A.5).

The dark and light electrical characteristics in Fig. 5.17, which were measured before and after cooling to  $-120^\circ\text{C}$ , showed a significant decrease in the curves of both measurements, which could occur considering the sharp negative temperature expansion [68] without changes of chemical bonds between the elements. The power drop of the solar cell is from 3.7 mW to 2.48 mW.

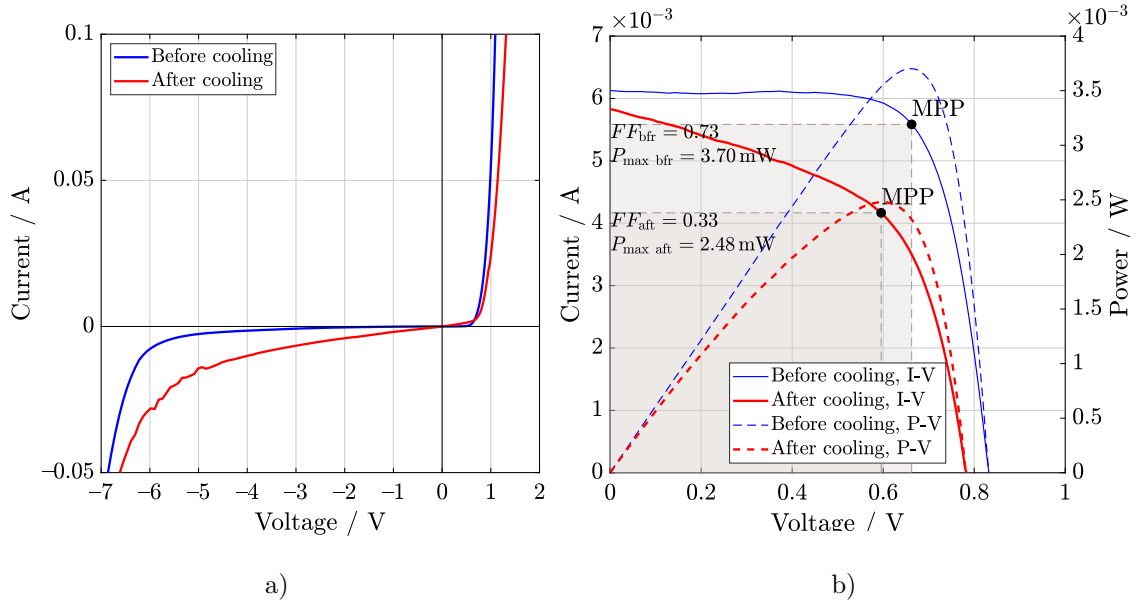


Fig. 5.17: Dark and light I-V curves after cooling experiment. Despite the relatively good reflectivity properties in Fig. 5.15 and the elemental composition from the Raman spectra in Fig. 5.16, there was a comparatively significant decrease in power, which is confirmed by both a) dark and b) light I-V characteristics.

With slow cooling and stabilization at  $-100^\circ\text{C}$ , the declining character of the spectra of elements C1s (Fig. A.2) and O1s (Fig. A.3) can be seen. In the binding energies of Al2p region (Fig. A.4), it is visible that the element bonds are relatively stable at a given temperature. When the temperature rises back, the spectra return to their original shape but not fully recovered. A much more distinctive decrease of the C1s, O1s and Al2p spectra in Fig. A.5 is seen in the case of more rapid cooling to the temperature of  $-120^\circ\text{C}$ , which has a significant effect on the state of the sample. Again, the effect of temperature for Al2p is less noticeable compared to other measured elements, and it was confirmed that the previous state, when returning to room temperature, is not entirely restored. The higher degradation

of the sample for lower temperatures is also evident due to the negative thermal coefficient, which occurs at very low temperatures and can lead to negative thermal expansion and damage to the atomic structure of the cell [69]. It is also necessary to realize that each material has a different thermal coefficient and may otherwise affect the sample. Here, only the top protective layers are examined due to the application of a given method, which allows elemental analysis to a depth of few nanometers.

## 5.4 Ionising radiation processing

Atomic force microscopy measurement of the morphology on the sample after exposure (Fig. 5.18b) manifested itself in the form of higher surface segmentation. These surface changes described in Tab. 5.2 may affect the differences in the optical parameters, but it depends mainly on its extent. The most considerable differences against measurement in Fig. 5.18b were observed in the case of higher skewness  $S_{sk}$  and kurtosis  $S_{ku}$  parameters. In histogram in Fig. 5.18 can be seen a slight decrease in height on average. It can be assumed that this change will not affect the optical properties on a larger scale. It is important to realize that the changes in the surface area are in order of units of nanometres.

Tab. 5.2: Surface roughness parameters for irradiated PV cells.

	Average height / nm	$S_a$ / nm	$S_{sk}$ / -	$S_{ku}$ / -
Before irradiation	9.122	2.357	0.316	0.247
After irradiation	5.561	1.521	1.046	2.233

In roughness analysis, it was mentioned when changing the surface parameter differences in Tab. 5.2, some optical properties may change. One of the essential properties of a solar cell is its reflectance. This reflectance is described by the light spectrum in Fig. 5.20, which is composed of three parts. As can be seen, the two curves of the sample almost overlap both before and after irradiation. Thus, it can be stated that gamma radiation minimally affects the performance of the cell in terms of reflectance. The most sensitive spot can be considered in the near-infrared spectrum, where there was a decrease in reflectance in units of per cent from 800 nm. The detected interference in the NIR region indicates the occurrence of the existing thin layers described in Sec. 4.1. Intensity change and curve shift results by reason of different thicknesses of the coating layers before and after irradiation. In the UVA light region is a visible shift. The difference is apparent within 5 to 10 nm. Shift of the curve results in a change in refractive index.

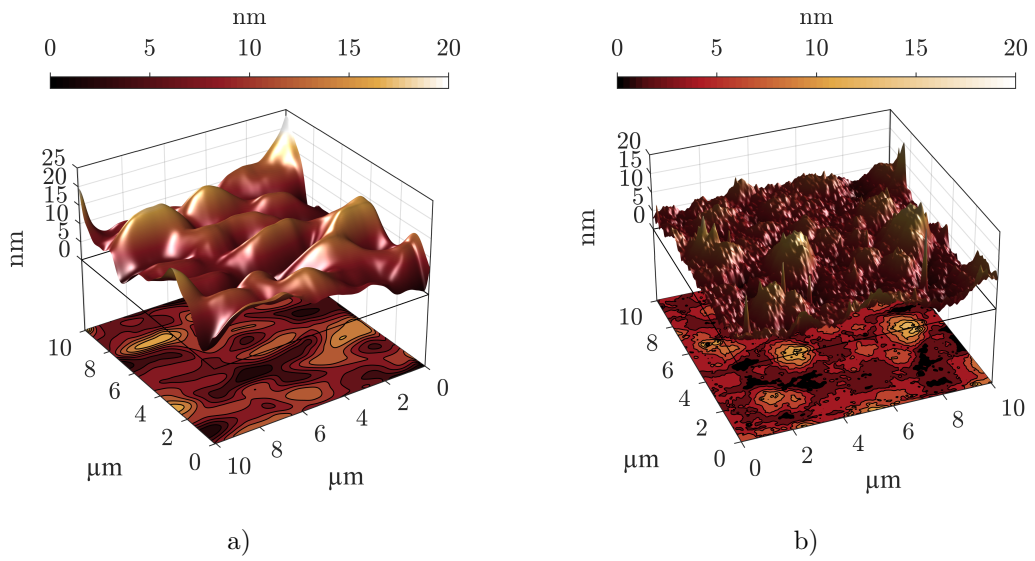


Fig. 5.18: a) Non-irradiated surface of GaAs solar cell in 3D and 2D view using an atomic force microscope. The cell has a typical shape and morphology with a relatively smooth surface compared to other types of solar cells. But b) after irradiation its structure shows a noticeable difference from the non-irradiated cell in Fig. 5.18a.

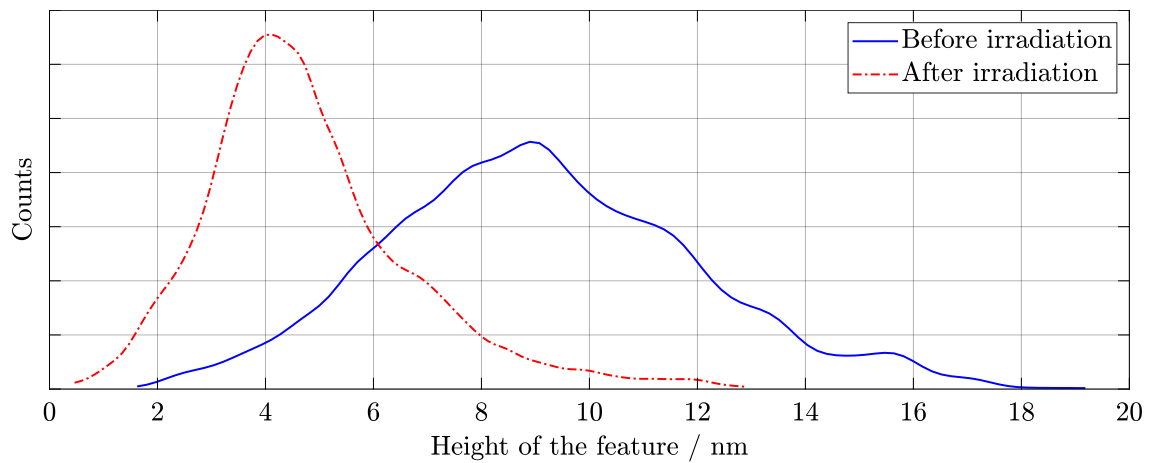


Fig. 5.19: Histogram of solar cell surface height distribution before and after irradiation. Statistical data is calculated from the surface of dimension  $10 \times 10 \mu\text{m}$ .

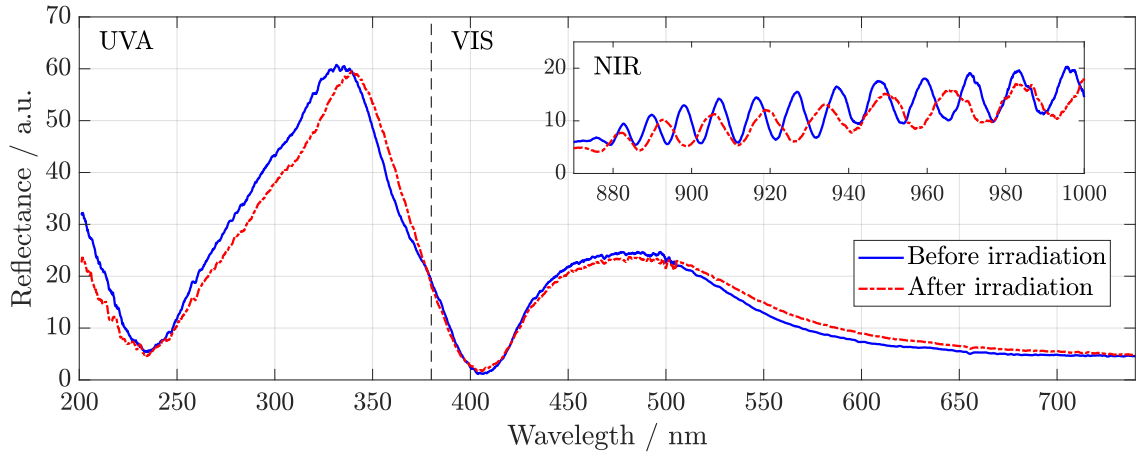


Fig. 5.20: Electromagnetic spectrum divided into three areas of light – ultraviolet, visible and near-infrared. The reflectance of the solar cell before and after irradiation is shown in the spectrum.

Measurement with SIMS of the irradiated sample was divided into two parts before and after irradiation for better clarity. The first part (Fig. 5.21 and Fig. 5.23) shows the top layer of the solar cell. The second part shows the interface to the Ge substrate (Fig. 5.22 and Fig. 5.24). Fig. 5.21 and Fig. 5.23 shows that a considerable amount of aluminium was found on the very surface. Thanks to this layer, the cell also maintains its stability and its degradation is slowed down. The peak of  $\text{AlO}^+$  was also added which correlates perfectly with Al peak suggesting that Al exists in the form of oxide mostly. The second part of the GaAs-Ge interface in Fig. 5.22 and Fig. 5.24 indicates that the material composition has not lost its stability.

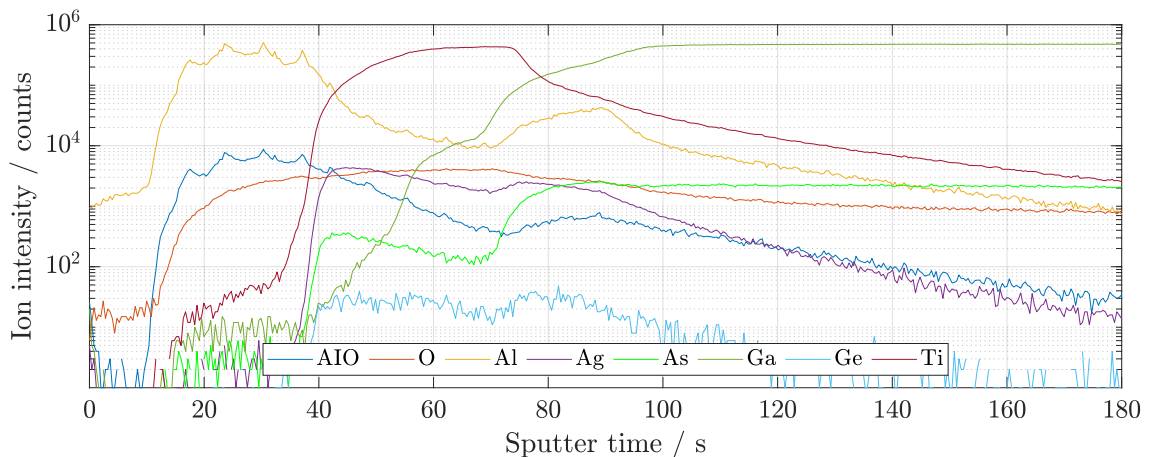


Fig. 5.21: The process of ion bombarding of the solar cell top layer before cobalt-60 irradiation. Several elements are visible in the plot. These elements indicate the protective and anti-reflection layers and the subsequent growth of the GaAs layer as the sputtering progresses further into the depth.

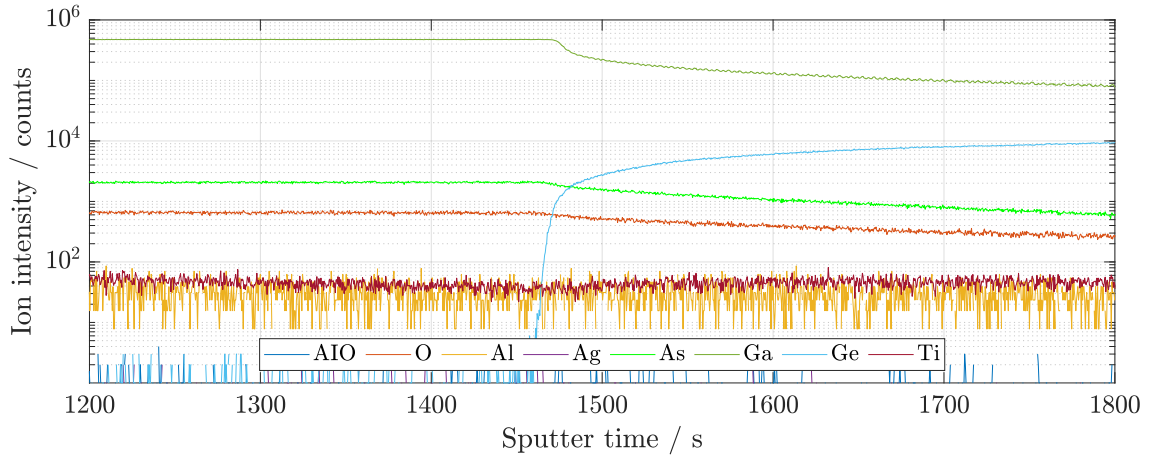


Fig. 5.22: Detail of transition between GaAs layer and Ge substrate before cobalt-60 irradiation analysed by Secondary Ion Mass Spectroscopy.

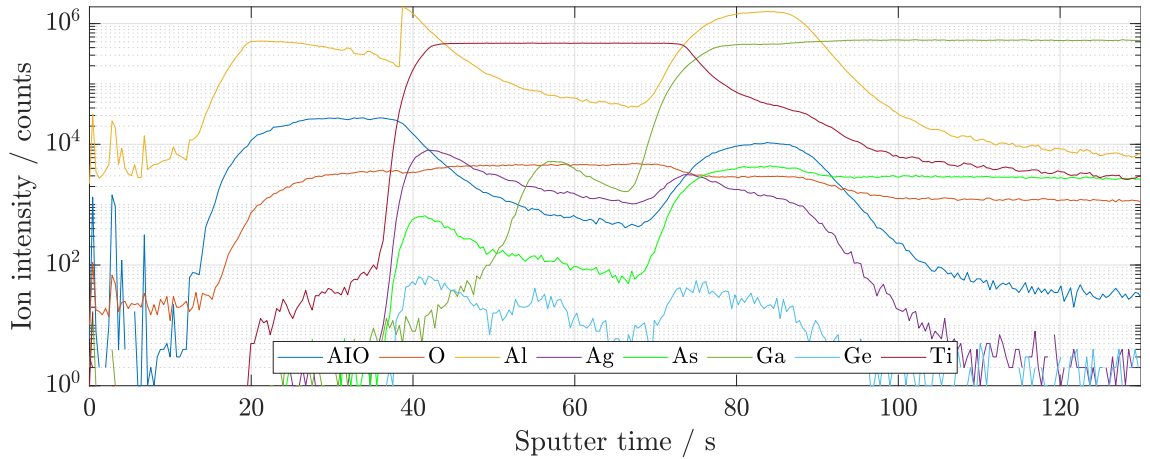


Fig. 5.23: The process of ion bombardment of the solar cell top layer after cobalt-60 irradiation. A higher increase in diffusion of the elements into the GaAs material is observed.

It is evident from Fig. A.6 and A.7, and A.10 that in most cases between a) and b) did not undergo significant changes for gallium, arsenide, and germanium after irradiation, and the solar cell thus retained its elemental composition for the most part<sup>1</sup>. Slight difference can be seen in the loss of Ga and As in the top layer in Fig. A.6 and A.7 a) before and b) after the irradiation. This loss can be confirmed by the different distribution of the thin layer of Al (Fig. A.8) and especially Ti (Fig. A.9) layer, where the difference is most noticeable and where after irradiation, there is a

<sup>1</sup>All three-dimensional images from the SIMS measurement after irradiation were moved to the appendix (Fig. A.6–A.10) for greater clarity of the dissertation.



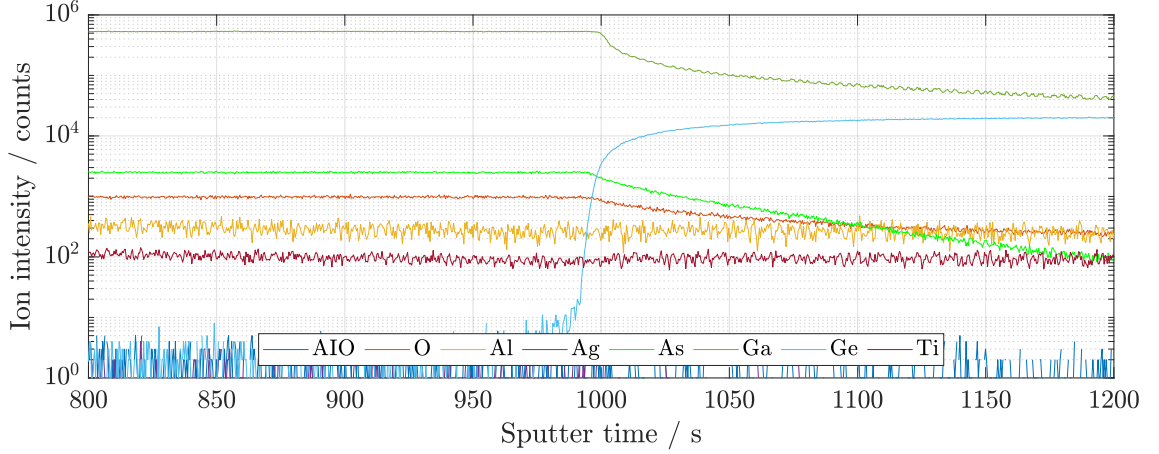


Fig. 5.24: Detail of transition between GaAs layer and Ge substrate after cobalt-60 irradiation analysed by Secondary Ion Mass Spectroscopy.

significant diffusion of the titanium layer into the material.

For the Raman spectroscopy depth profiling method, several differences were noticed before and after irradiation and within different depths. The profile images in Fig. 5.25a and 5.26a show the occurrence of a particular mode at different depths from the surface, which is colour-coded according to the intensity of the mode. The coloured area is a  $40\text{ cm}^{-1}$  wide region selected around the GaAs LO mode. It is evident in Fig. 5.26a, the distribution of this occurrence is broader, while in Fig. 5.25a, it is located more centrally. Also, a slight shift from occurrence in Fig. 5.25a has been observed against Fig. 5.26a.

If we focus on plots of three different spectra depending on their position (A, B, and C) in the range of about 800 nm apart in the surface, we see differences from the Fig. 5.25b and 5.26b again. Moving deeper from position B to A and from position B to C in Fig. 5.25b will result in almost the same decrease in GaAs LO. However, the same movement dramatically changes the ratio between AlAs TO and AlAs LO. It can be argued that the differences in the structure below from A to B position results in the aluminium containing layer mainly.

Fig. 5.26b shows a different situation. The decrease in GaAs LO mode appears between the A and C positions. Also, there is a continuous decrease in AlAs TO mode from A to C position. Nevertheless, if we focus on GaAs LO and AlAs LO in position B, peaks remain the sharpest. Also, the ratio between AlAs LO and AlAs TO is the highest in the same position [70].

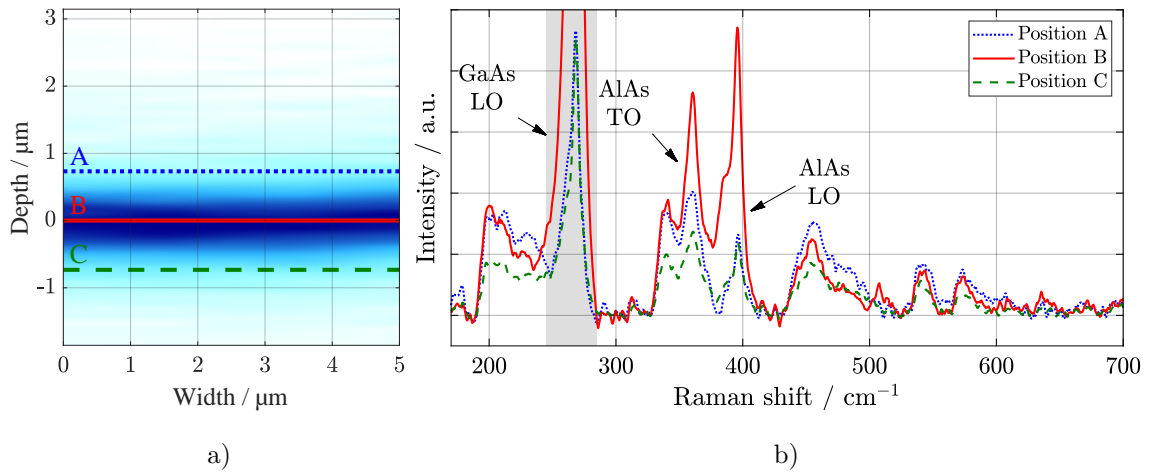


Fig. 5.25: Depth profiling of unprocessed GaAs solar cell using the Raman spectroscopy. Picture a) shows a profile map of a specific band selected and marked in plot b). This band is  $40\text{ cm}^{-1}$  wide.

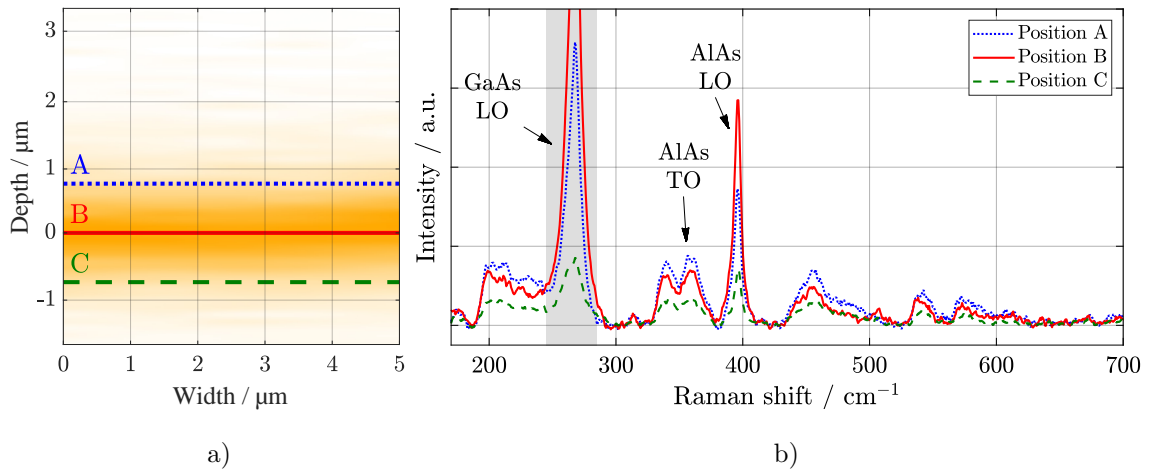


Fig. 5.26: Depth profiling of irradiated GaAs solar cell investigated by the Raman spectroscopy. Again, picture a) shows a profile map of a specific band selected and marked in plot b). The band position is the same as in Fig. 5.25b, from  $245\text{ cm}^{-1}$  to  $285\text{ cm}^{-1}$ .

An excellent result after irradiation can be marked in changes which is shown in Fig. 5.27a and Fig. 5.27b measured by SEM with STEM detector. As is evident in a given scale, the degradation of the material is minimal, and it can be said that the stability of the material is high. Both figures show a cross-section of a thin lamella over several layers. On the top side of the cell – the lightest layer – is carbon, which served only as a protective layer from the creation of the lamella. The other layers do not show visible signs of degradation.

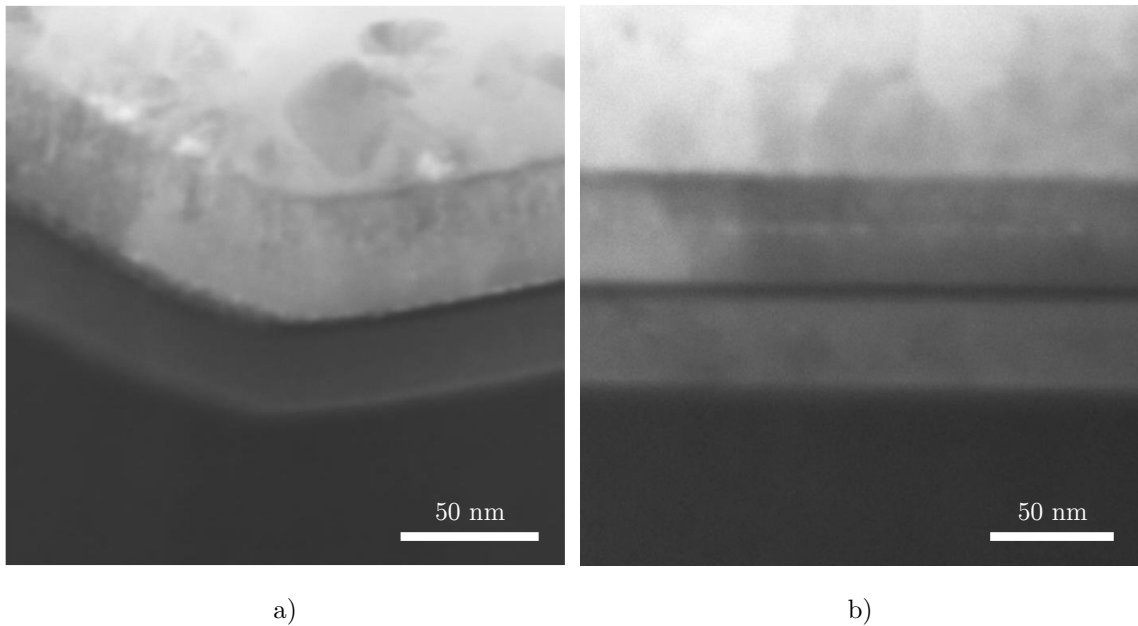


Fig. 5.27: Observation of the a) non-irradiated and b) irradiated solar cell by electron microscope with STEM detector. The picture shows a cross-section of a thin lamella and several surface layers.

Using the electroluminescence showed in Fig. 5.28a, where is the solar cell before irradiation in the forward direction, several micro-cracks and defects are visible on the surface. These microcracks cannot be considered to have a significant impact on the function of the solar cell and, just as the occurrence of point defects in Fig. 5.28b, this number of defects within the solar cell is typical, as all measured samples showed a similar condition.

If we compare the solar cell before and after the irradiation (Fig. 5.28 and Fig. 5.29) in the a) forward and b) reverse direction by electroluminescence, we can see that, especially in the forward state, the number of defects remains about the same density. Some cases showed an increased number of point defects on silver contacts (Fig. 5.29b). As mentioned, this interesting phenomenon did not manifested in all cases, and therefore further investigation is needed.

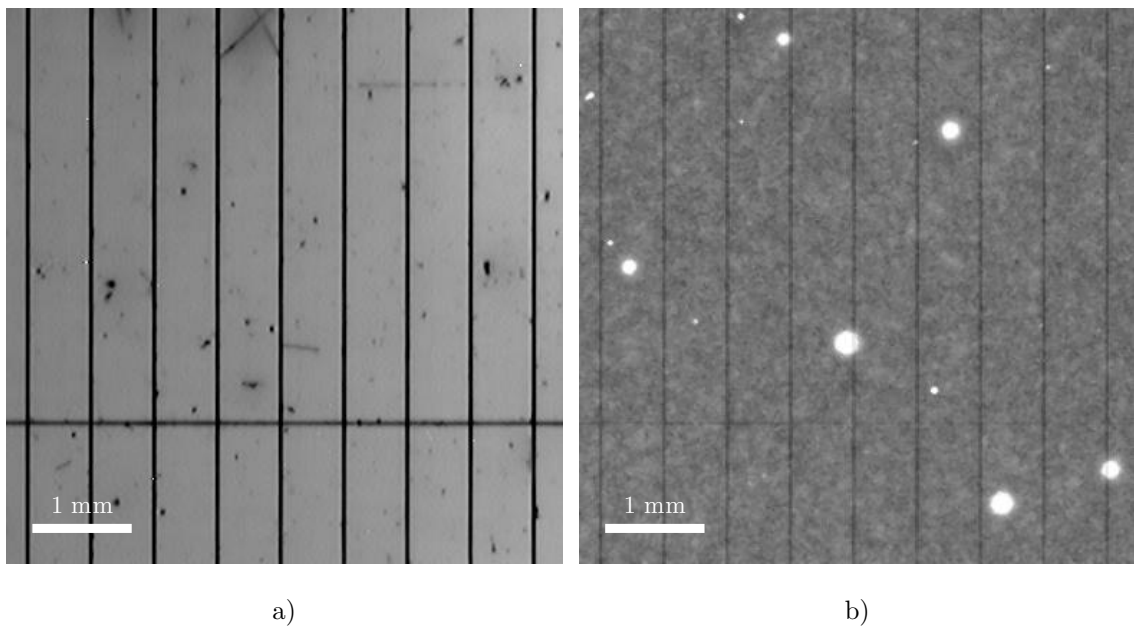


Fig. 5.28: Defect visualisation using electroluminescence before irradiation. The solar cell was connected in a) forward and b) reverse direction. In particular, cracks are visible in Fig. a), but point defects in Fig. b).

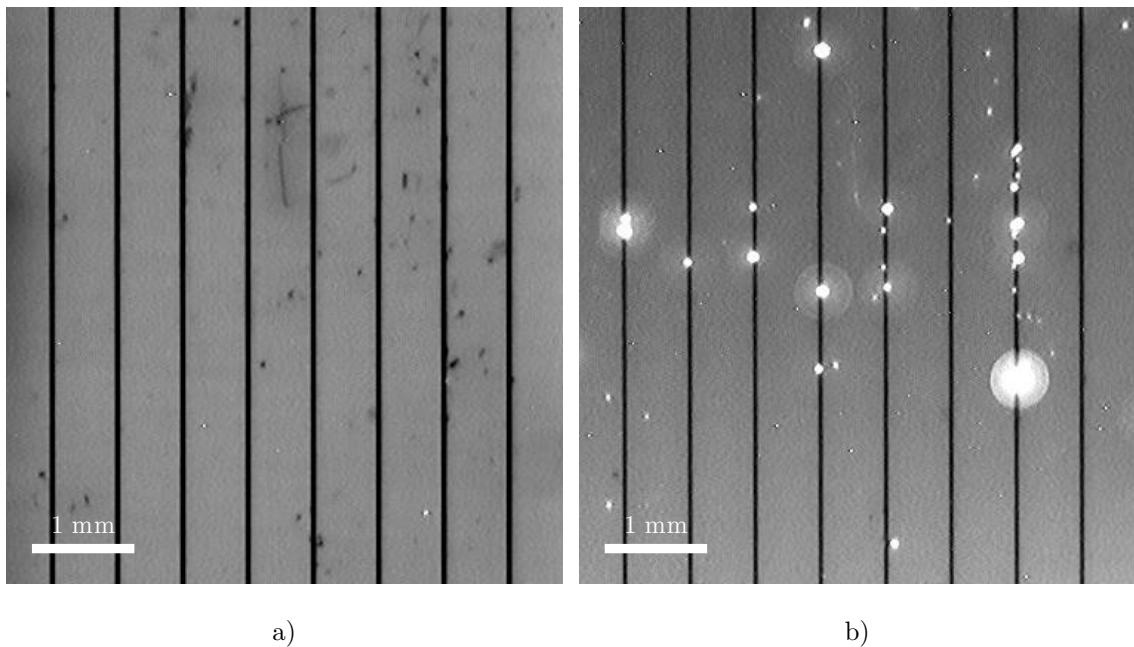


Fig. 5.29: Defect visualisation using electroluminescence after irradiation. There is an interesting case where there are several point defects on the PV cell contact in Fig. b).

Further investigation of defects was carried out in the form of the EBIC method and its examination of charge carriers on material and its surface. During observation in PV-EBIC mode, small changes were recorded at the surface contact interface. Extensive top view of the solar cell surface (Fig. 5.30) was realized to examine not only the contacts but also the surface and sub-surface defects around it. Defects on the PV cell surface do not appear here in the context of different charge carriers. The difference in the surface-contact interface may also be by reason of the defects affecting the contacts described in Fig. 5.29b during electroluminescence.

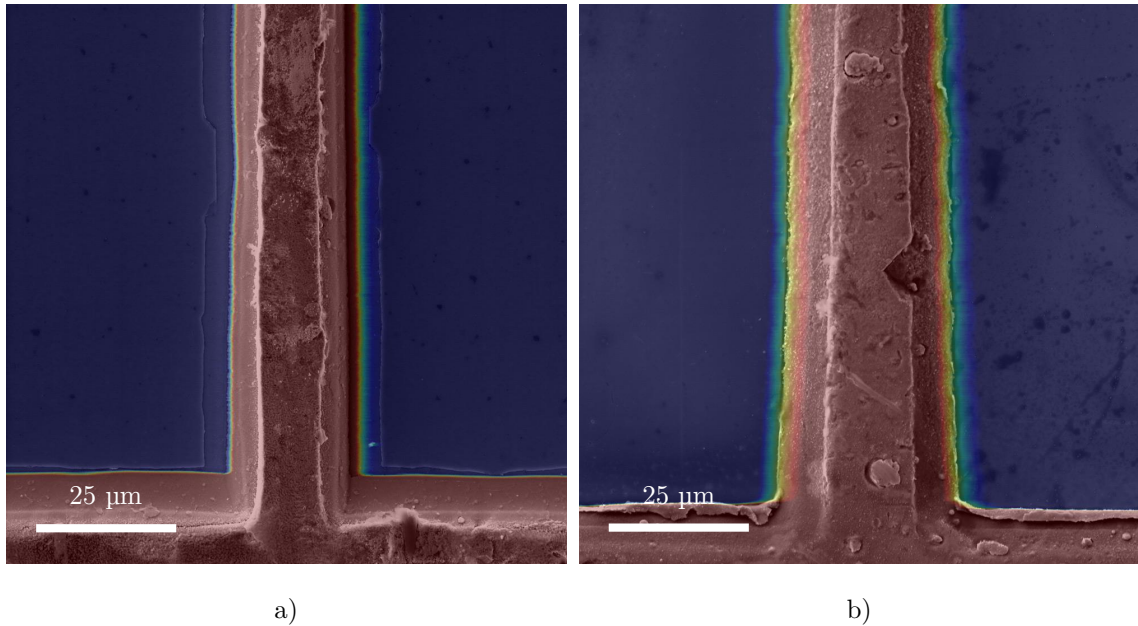


Fig. 5.30: Top view of the contact and solar cell surface a) before and b) after irradiation in PV-EBIC mode.

A detailed view of the contact extending into the surface of the material in PV-EBIC mode is provided in Fig. 5.31. The functional interface between the two materials demonstrates the hardness of the PV cell to a high radiation dose.

A noticeable difference between the carriers can be seen when applying the EBIC between the non-irradiated (Fig. 5.32a) and irradiated (Fig. 5.32b) samples in the X-EBIC mode. The different regions of the PN junction can be caused by the previously mentioned changes in the upper layers of the PV cell. Another interesting thing revealed by the SEM microscope is the crystallization of the germanium substrate in some parts of the solar cell. The occurrence of the crystallized region is well visible in Fig. 5.32b in the bellow part.

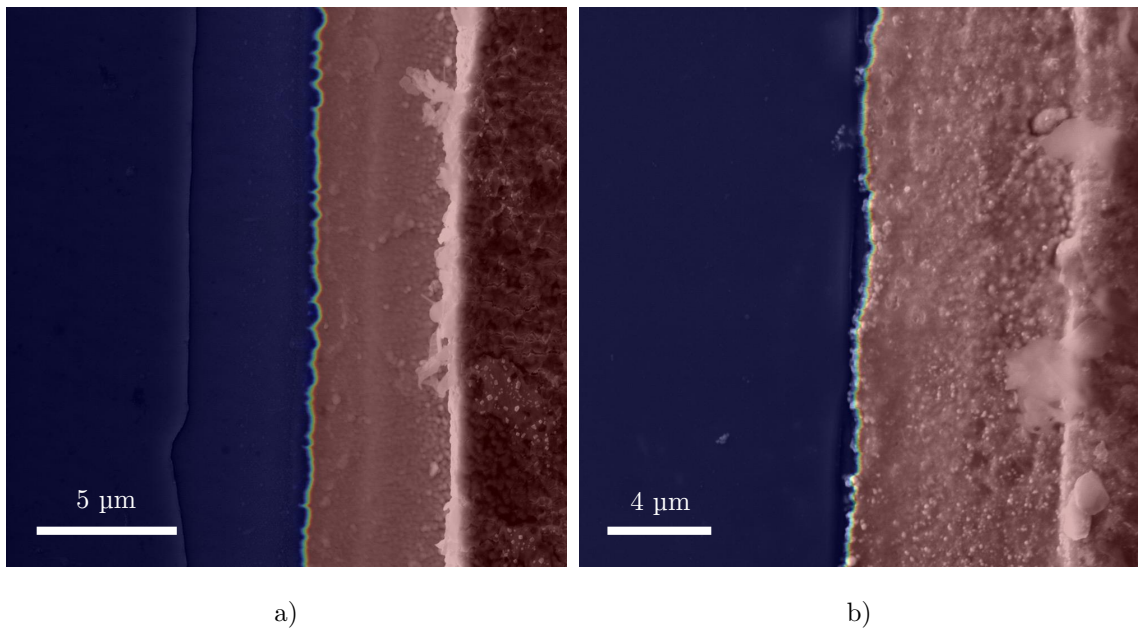


Fig. 5.31: Detail from the top view of the contact and solar cell surface a) before and b) after irradiation in PV-EBIC mode.

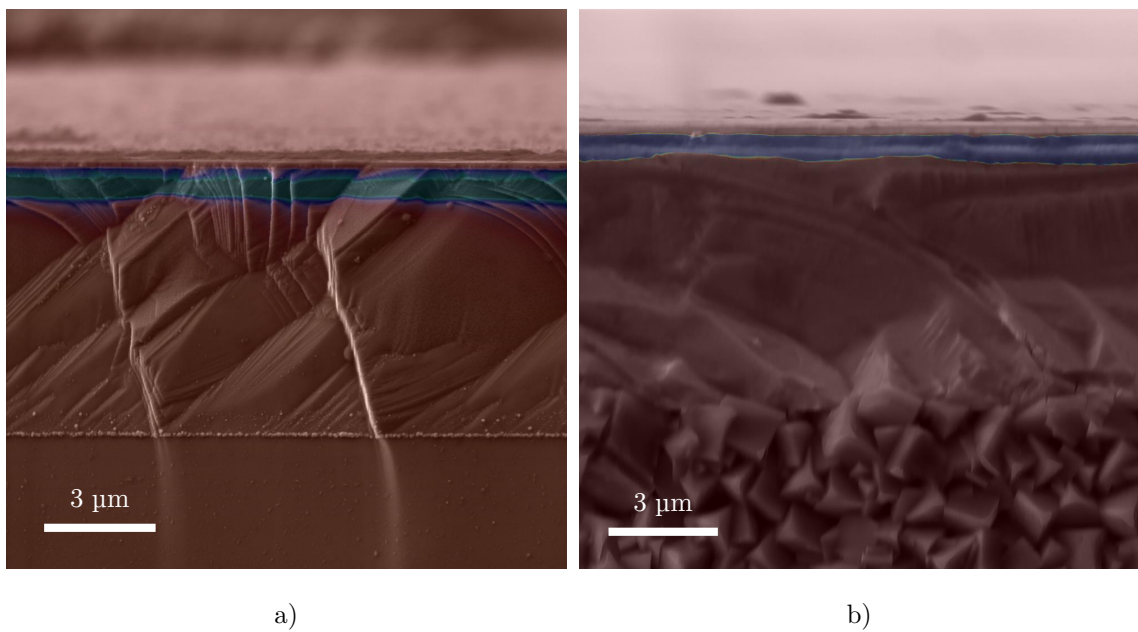


Fig. 5.32: Cross-section of GaAs-based PV cell a) before and b) after irradiation in X-EBIC mode.

Initially, the crystalline Ge substrates are used for the direct growth of high-quality epitaxial GaAs. Radiation-stimulated solid-state recrystallization was caused because gamma irradiation supplies additional energy to the crystal and could be compared with irradiation by fast neutrons. Caused by irradiation point defects, strain in the crystal lattice, atomic displacements lead to the appearance of irregular patterns at the substrate.

The remaining optical measurements using FTIR and spectral ellipsometry indicate that interference fringes in the plot of dielectric function (Fig. 5.33) have different periodicity. The difference indicates the changing layer thickness caused by the diffusion of the metal component from the anti-reflective coating into the active layer of solar cells. The shift of the maximum of dielectric function is attributed to the occurrence of disorder caused by radiation. This structure related to a phenomenon is confirmed by FTIR measurements (Fig. 5.34), where the same trend interference maxima narrowing is observed. A possible consequence of diffusion may occur by breaking oxygen bonds by gamma radiation in the metal oxide, as reported by authors of Ref. [71].

The change of the oscillation period at FTIR spectra confirms incorporation of the metals coming from anti-reflective coatings, contacts, and doped regions into the structure of the PN junction.

Besides the interference fringes, ellipsometry shows the shift of permittivity. Movement of both imaginary and real part of permittivity to lower energy range is evidence of changing of electronic structure and optical constant as the refractive index as well.

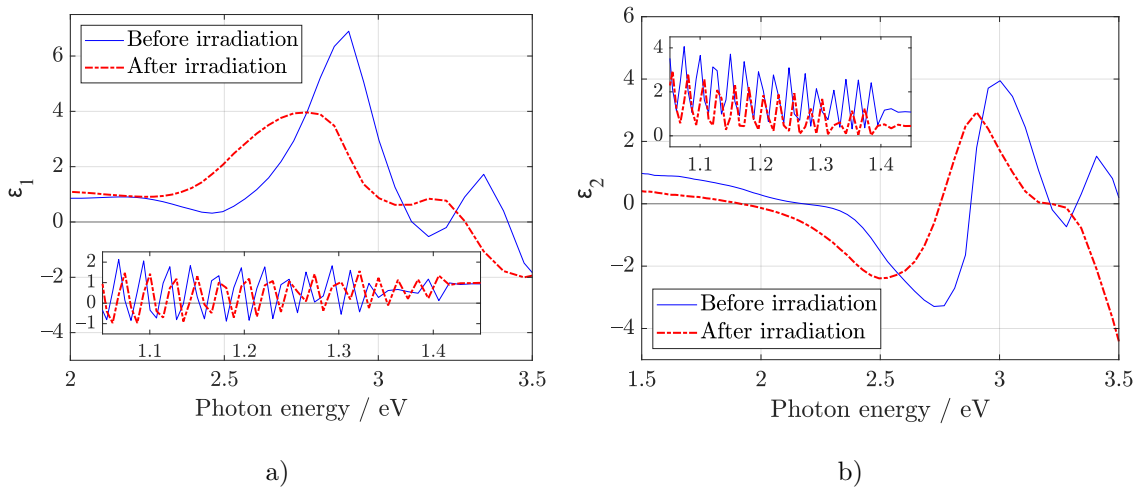


Fig. 5.33: The character of dielectric function of a) real  $\epsilon_1$  and b) imaginary  $\epsilon_2$  part. The variation of real and imaginary parts of  $\epsilon$  is attributed to additional light scattering at the irregular surface and near-surface area.



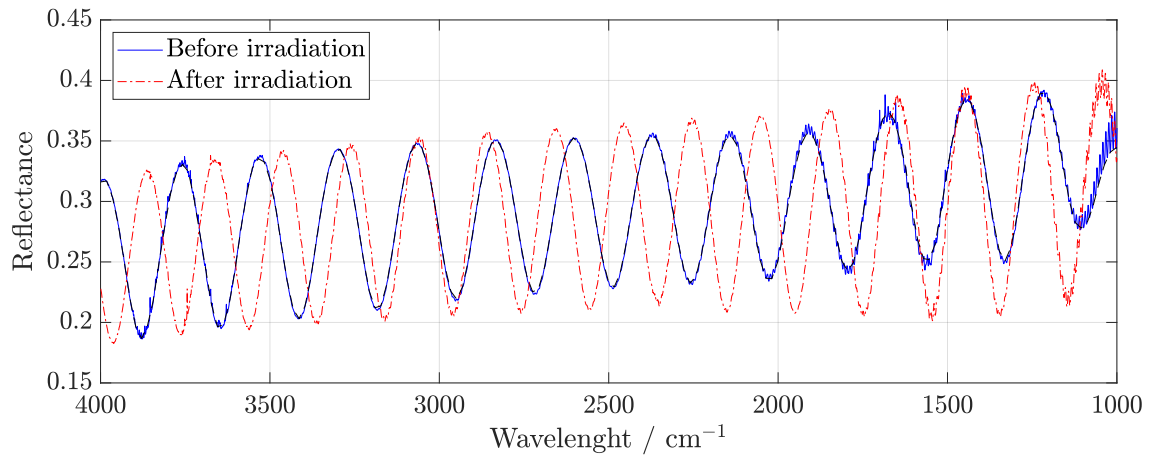


Fig. 5.34: Different interference in PV cell before and after irradiation indicates a different thickness of layers.

From the I-V characteristics measured in Fig. 5.35a and Fig. 5.35b, the solar cell power loss can be observed. This power loss was predicted and could be caused by the degradation of the structural bonds mentioned, for example, in part of Raman investigation and by the change in the optical parameters of the cell (reflectance investigation). In the dark I-V characteristic in Fig. 5.35a, the change is reflected behind the knee reversed and forward bias in decreasing steepness. In Fig. 5.35b, P-V characteristics, the output of the irradiated cell decreased by 0.32 mW, and the fill factor decreased by 0.24.

As in I-V curves, deteriorated electrical properties after particle penetration by the radioactive isotope  $^{60}\text{Co}$  were assumed. The most significant impact of increased power spectral density occurred in the lower voltage range, where noise increased by order of magnitude, mainly for 2, 3 and 4 V. From this limit, the noise value of the sample after irradiation has not changed, and the noise in the area approaching the curve knee about 4.5, 5, 5.5 and 6 V has remained stable (see Fig. 5.36).

Nearly every sample which has been exposed to the atmosphere typically contain from  $(0.6 \pm 0.2)$  nm thick adventitious carbon surface contamination [72]. These are common contaminants that may be removed by argon sputtering. In this case, the behaviour of the carbon after irradiation is also monitored and therefore it is not desirable to clean it. In Fig. 5.37b, a typical C1s spectrum of oxygenated carbon with the adventitious carbon (C – C bonds) is visible at 284.8 eV binding energy. After irradiation, these bonds decreased, but also increased C – O – C bonds at binding energy 286.2 eV which are partially overlapped by C – C structure. Also, contamination of O – C = O components has emerged at 288.5 eV. According to XPS and this peak, it can be seen that oxygen is part of aluminium.



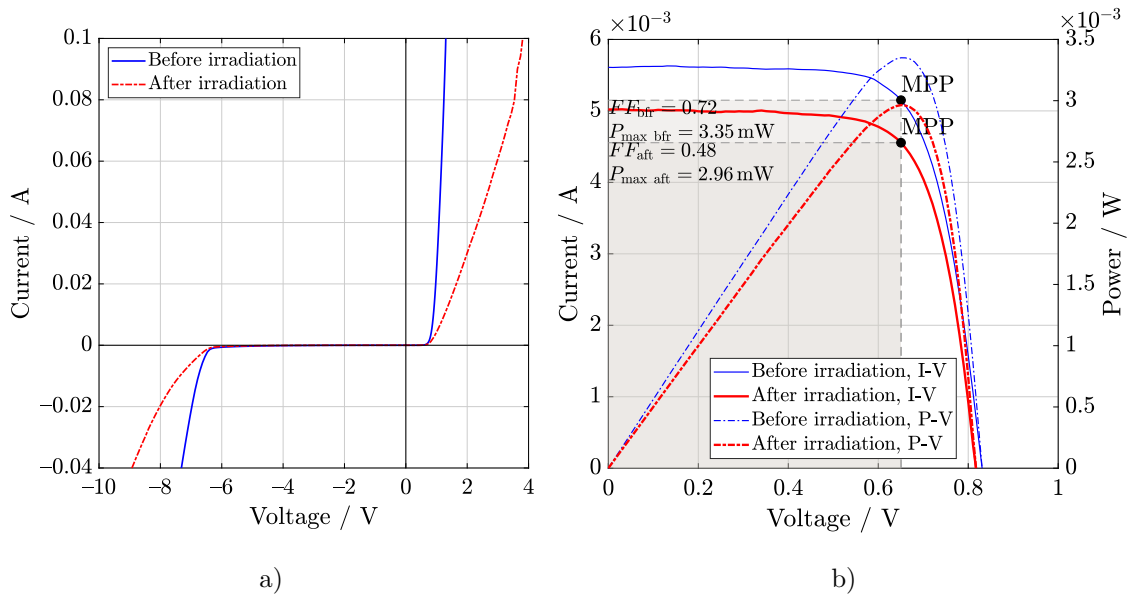


Fig. 5.35: In a) first figure are two overlaid dark I-V curves in lin-lin scale. The blue line indicates the characteristic of the non-irradiated solar cell, and the red line represents the irradiated solar cell. In b) second figure are illuminated I-V and P-V characteristics of the same sample before and after irradiation of  $^{60}\text{Co}$ . The maximum power point is marked in the characteristic, which indicates the highest efficiency point of the solar cell. The plot also shows the fill factor and the maximum power of the cell before and after irradiation.

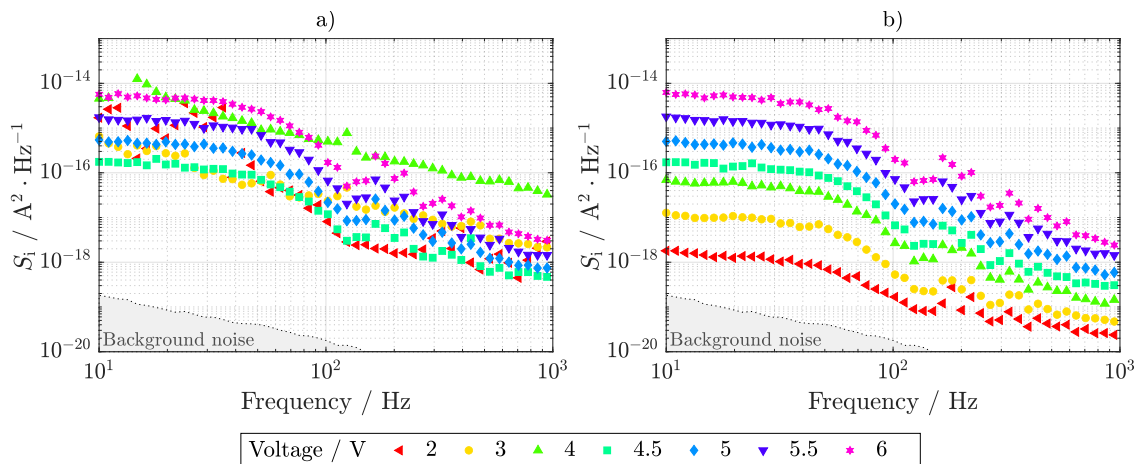


Fig. 5.36: Comparison of two plots from measured power spectral density data. The figure on the left side represents the PSD of the sample before irradiation, on the right side, the PSD of the same sample after irradiation. Both plots are also supplemented with background noise.

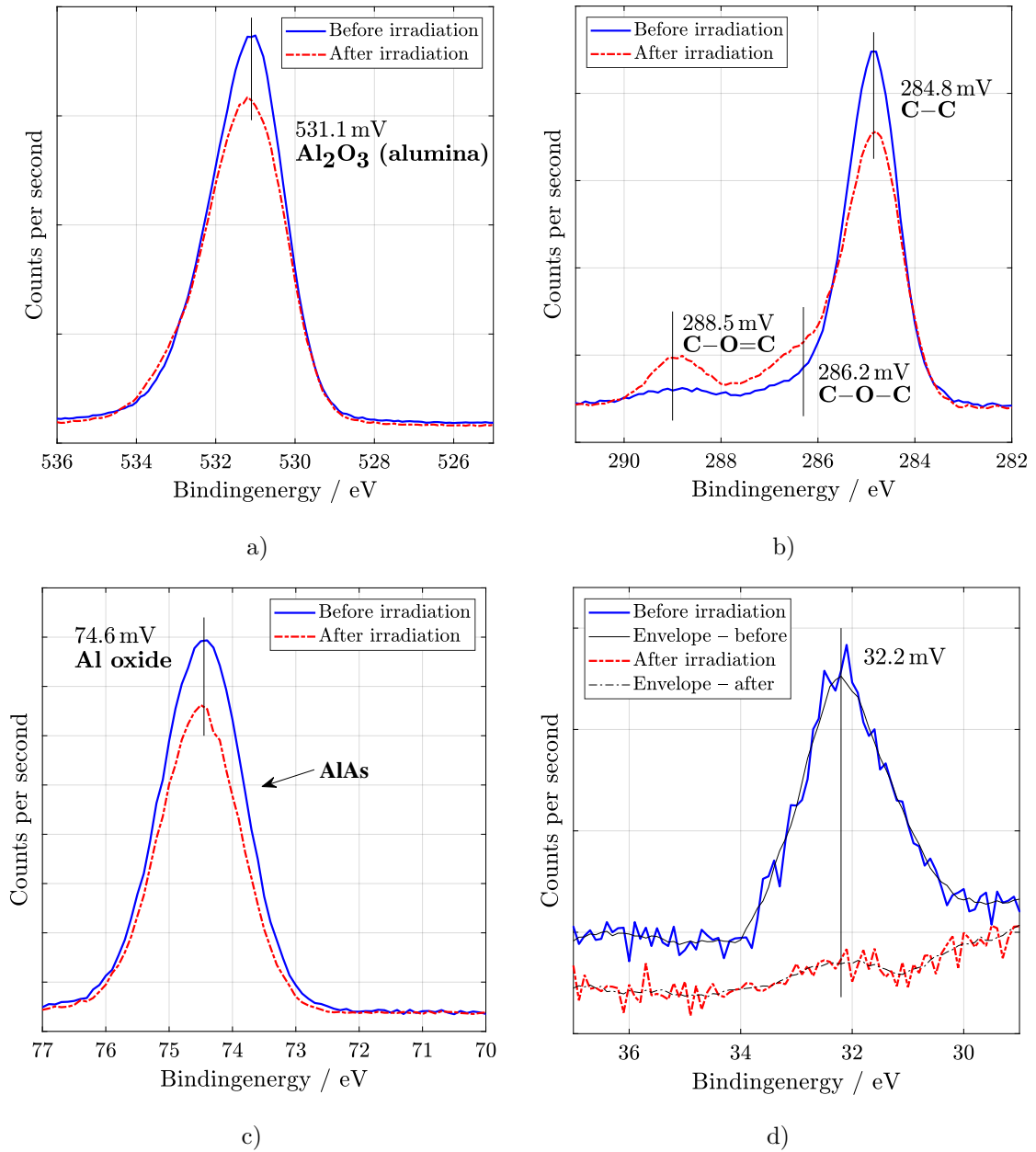


Fig. 5.37: Photoelectron spectra's after and before gamma irradiation. a) O1s, b) C1s, c) Al2p and d) Ti3p regions are observed.

## 5.5 Exposure to the supercontinuum light beam

It is known that  $\text{AlO}_x$  is used for passivation of solar cell surfaces [47] by virtue of the excellent protective and anticorrosive properties of aluminium oxide [73]. XPS broad spectra in Fig. 5.38 show the presence of aluminium and oxygen peaks that belong to the coating. Before evaluation, the spectra were calibrated to C1s peak at 284.6 eV. Both Al2s and Al2p peaks (Fig. 5.42 and 5.41) were deconvoluted to  $\text{Al}^{3+}$  and  $\text{Al}^{x+}$  oxidation states. The amount of aluminium suboxides bonds [74] is lower after illumination.

Nevertheless, a slight displacement of the Al peak indicates the degradation of the film. A change of the binding energy indicates a relative loosening of the structure because the elements from the anti-reflection coating diffused into the depth. Slight increase of C – O bonds could be observed at C1s peak (Fig. 5.39). The components of O1s (Fig. 5.40) binding energy are associated with bonding with carbon and aluminium and in agreement with Al2p, Al2s and C1s peaks fitting.

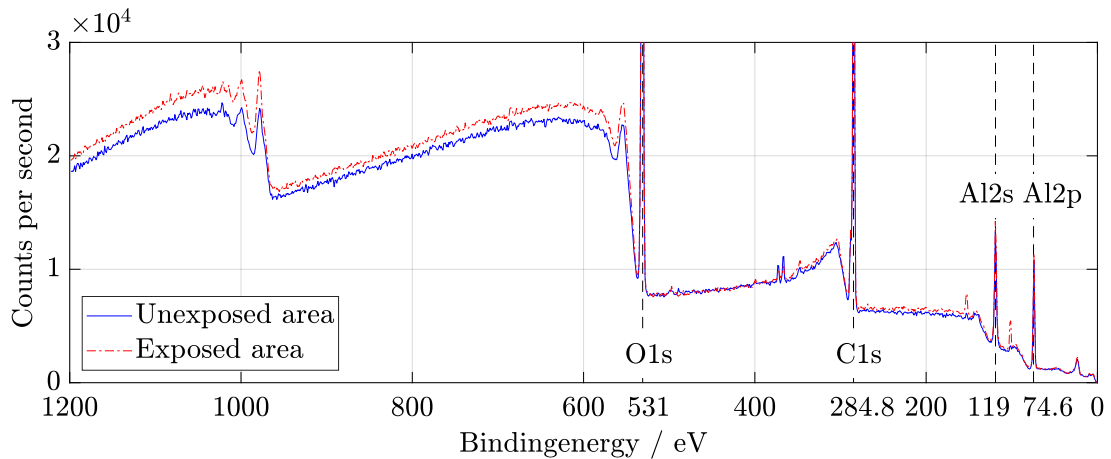


Fig. 5.38: Wide XPS spectra from supercontinuum laser irradiation. Marked are four significant peaks: O1s, C1s, Al2s and Al2p.

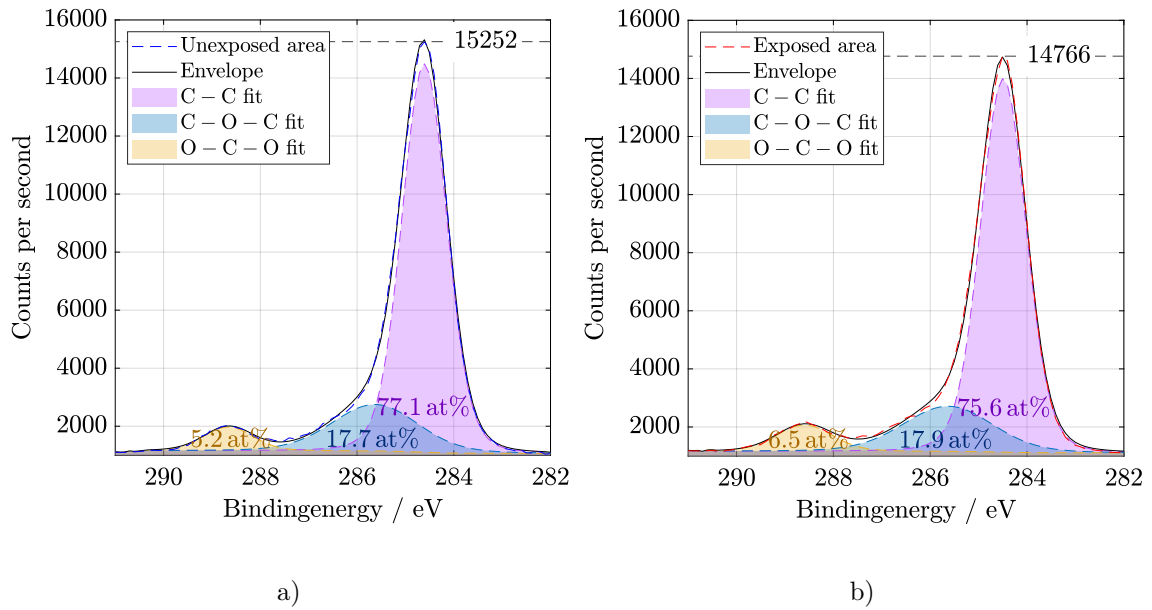


Fig. 5.39: High resolution of C1s region from XPS a) before and b) after SL irradiation.

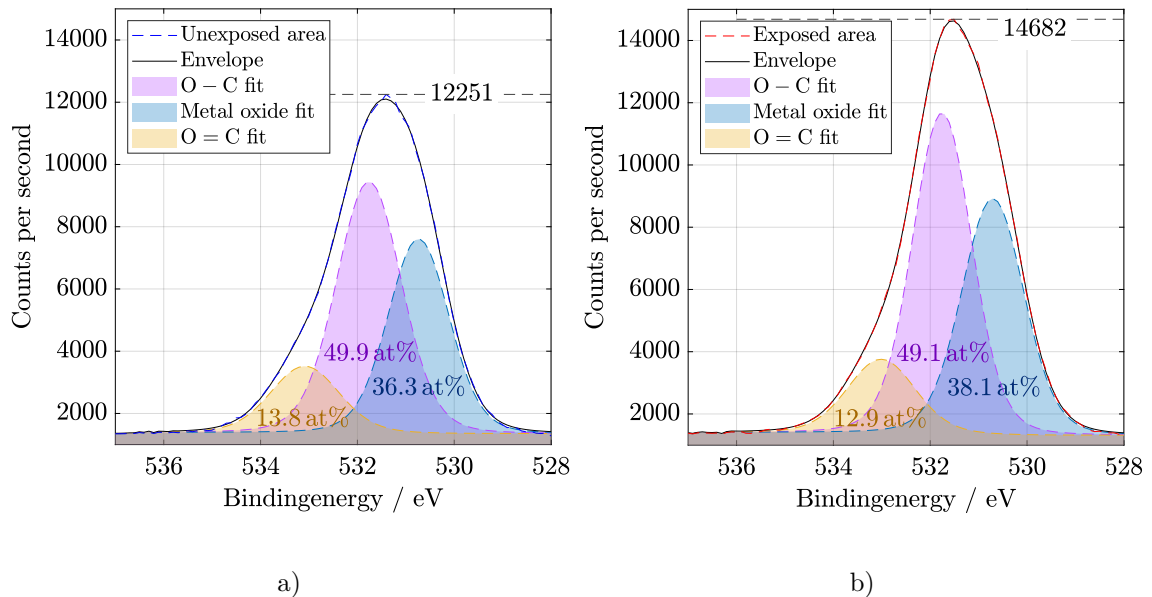


Fig. 5.40: High resolution of O1s region from XPS a) before and b) after SL irradiation.

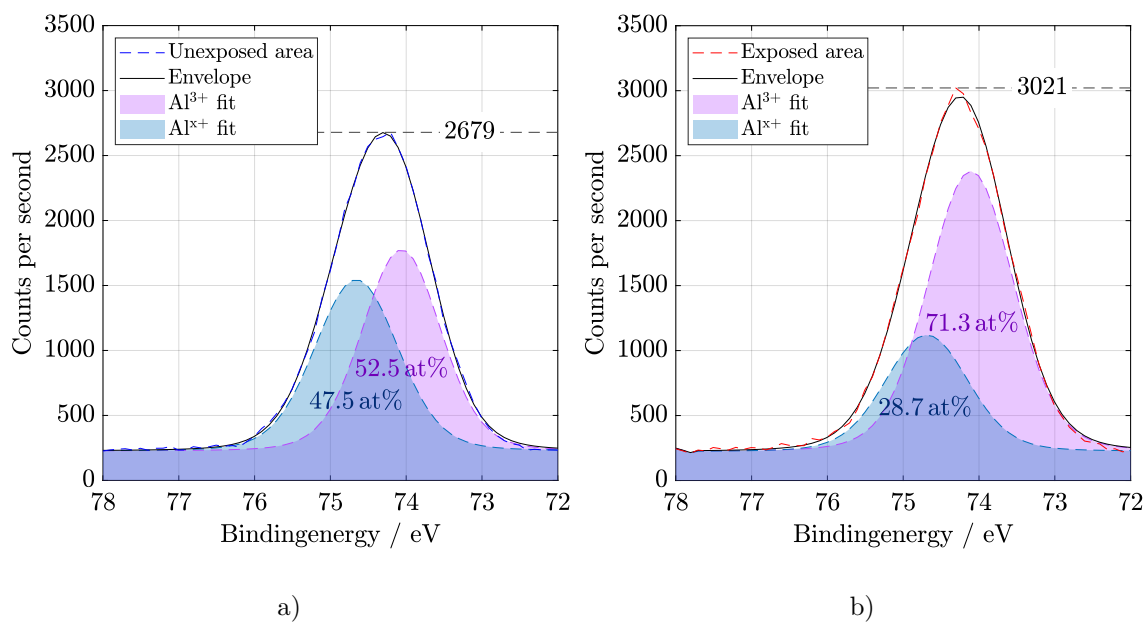


Fig. 5.41: High resolution of Al<sub>2</sub>p region from XPS a) before and b) after SL irradiation.

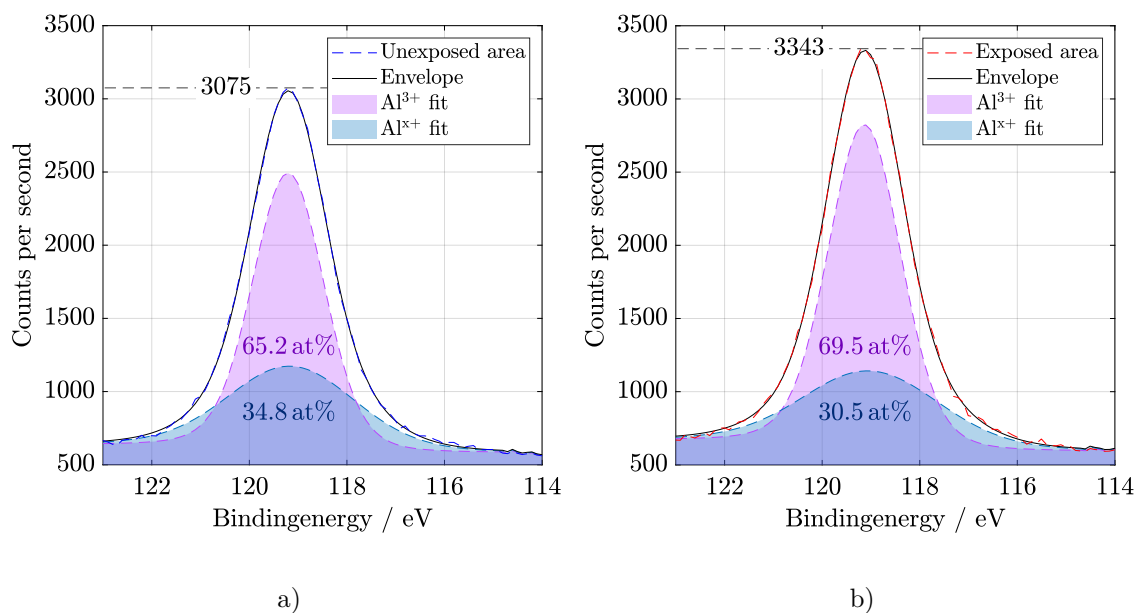


Fig. 5.42: High resolution of Al<sub>2</sub>s region from XPS a) before and b) after SL irradiation.

Scattering at longitudinal optical phonons and changes in layer thickness as a result of aluminium diffusion can cause energy losses. The decrease of these phonons' intensity, as shown in Raman spectra in Fig. 5.43, may explain the temporary improvement in the performance of solar cell under illumination (Fig. 5.45). Change of local vibrational modes at Raman spectra can also be associated with deep donor levels referred to as DX centres. The TO phonon of GaAs stays similar asymmetric form before and after SL irradiation. It is possible to observe the small difference in relative intensities of AIAs phonons indicates that displacements may occur at As sites. Low-intensity broad peaks around 500 to 580  $\text{cm}^{-1}$  belong to second-order GaAs-like TO and LO phonons [75].

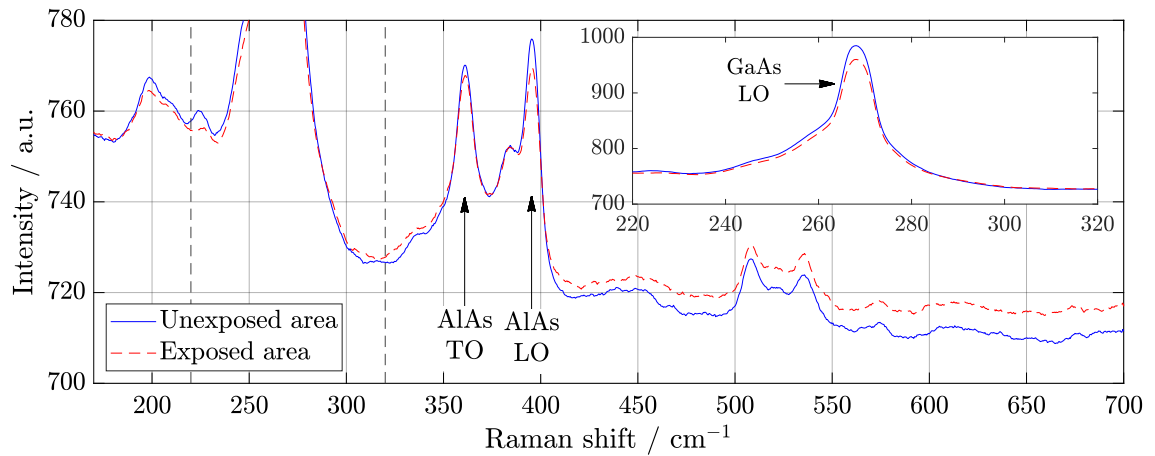


Fig. 5.43: Raman spectroscopy from supercontinuum laser irradiation. Due to the height of the transverse-optical mode of GaAs, in order to preserve detail, the peak was plotted in a separate graph.

The results in Fig. 5.44 of reflectivity in VIS are negligible; the interference fringes in NIR show a difference. Number and amplitudes of the fringes slightly differ, and a small shift to higher wavelength is observed. Larger intensity is related to the degradation of antireflective coating of the samples.

The number of fringes increased due to changing of the layers interface areas and their thickness, and the same time the shift of the spectra confirms it as the result of damages induced by radiation is consist in displacement and interdiffusion of Ti and Al atoms. The results of the reflectometry are in correlation with element profile studied by SIMS (Fig. 5.48).

Light exposure produces the defects caused by the displacement of atoms. It influences a charge distribution at the interfaces of the PN junction. The SIMS analysis was carried out several times in order to avoid the effect of local defects on the results [76]. Fig. 5.47 shows the distribution of elements along with all PV cell and shows the changing of the distribution of the elements at the GaAs/Ge interface.

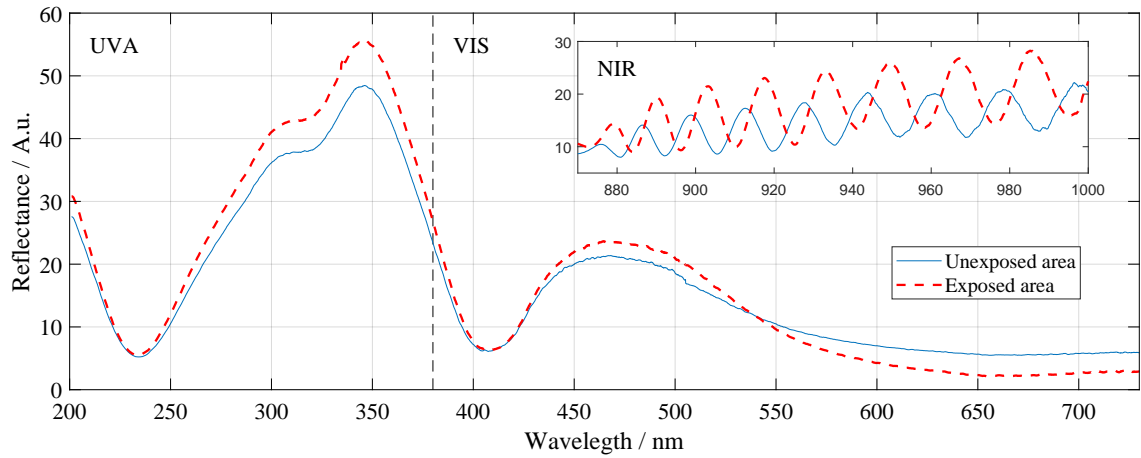


Fig. 5.44: Reflectance measurement from supercontinuum laser irradiation. There is a significant change, especially in the NIR region, indicating differences in thin-films.

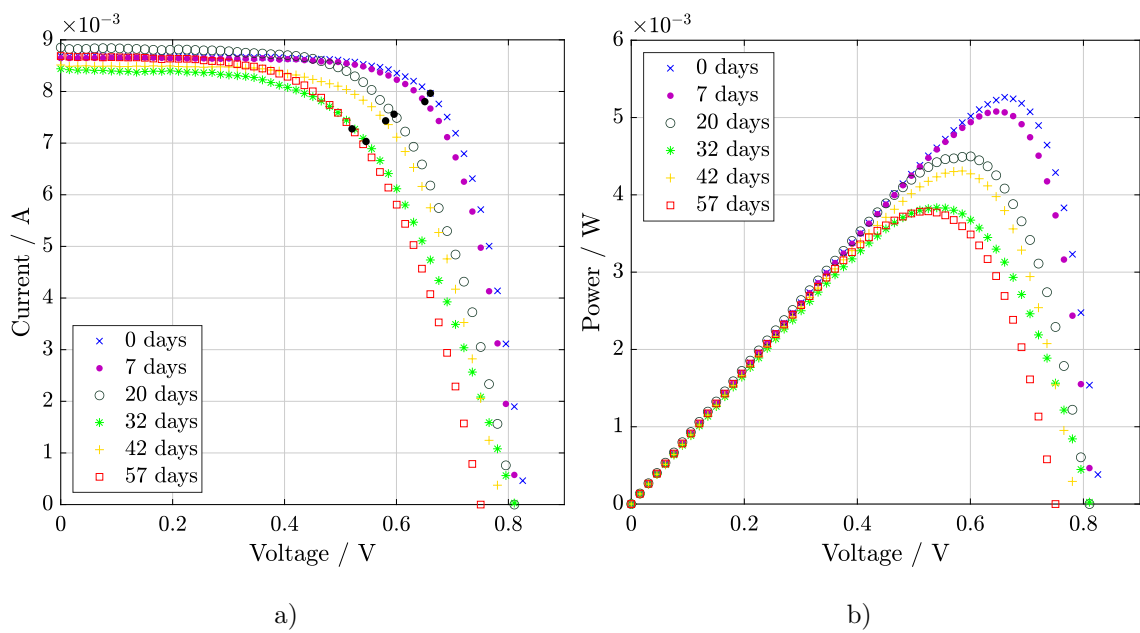


Fig. 5.45: Light I-V curves from supercontinuum laser irradiation. In a) I-V characteristics are MPPs indicated. In b) power characteristics, a slight increase in performance may be observed during 42 d.

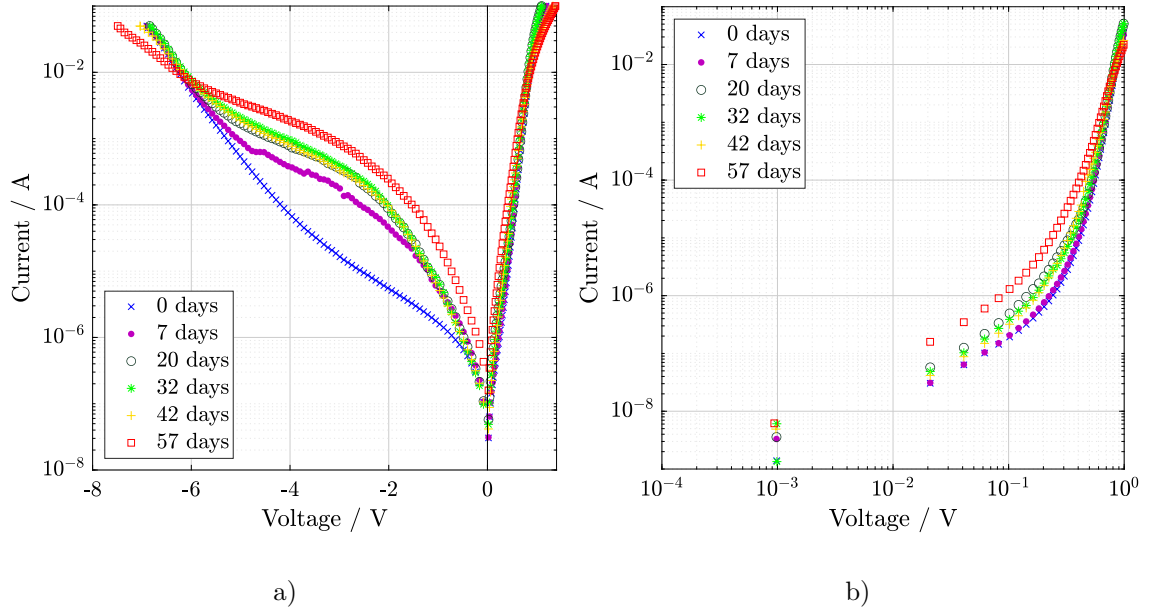


Fig. 5.46: Dark I-V curves from supercontinuum laser irradiation in a) semi-logarithmic and b) log-log scale. Slight relaxation and improvement during 20 to 42 d is observed.

Nevertheless, the most significant changes that influence electrical behaviour belong to the thin surface layers. Thin-film layers were also visualised three-dimensionally before irradiation in Fig. A.11. The detailed spectrum is shown in Fig. 5.48. The character of Al and Ti diffusion is mostly anisotropic and tends to AlGaAs layer, changing the concentration of aluminium creating displacement defects. Kinetics of Ti-sinking to GaAs compounds was intensively studied in Ref. [77, 78] before.



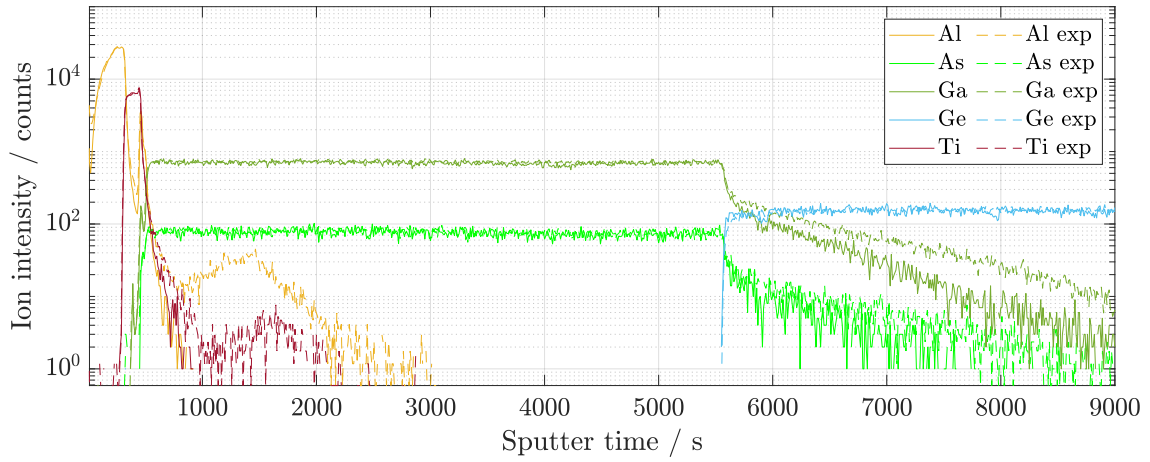


Fig. 5.47: The whole etching process using SIMS in time dependence. The graph is in semi-logarithmic representation. The etched was exposed (dashed line) and unexposed area.

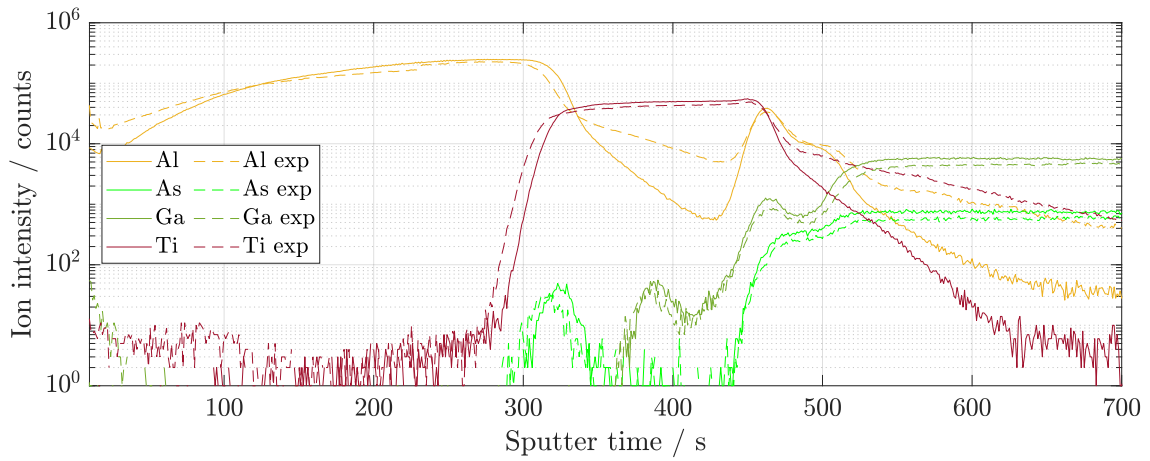


Fig. 5.48: The first few etched tens of nanometers of the solar cell surface in detail using SIMS. The change in Al is especially visible.

## Conclusion

A comprehensive measurement of degradation of GaAs photovoltaic cells has been performed. Surface morphology, material, electrical and optical properties were studied. All evaluation methods were selected to complement each other. Each measurement provides different information and varies in used method.

Prior to the use of the methods by which GaAs solar cells were stressed, surface and cross-section inspections and the occurrence of subsurface cracks and point defects were investigated using the EBIC method. In contrast to silicon cells, GaAs PV cells are very resistant to surface cracks, which were present in substantial quantities in silicon cells. It was seen from the cross-section of the GaAs sample that electrically active impurities could be introduced into the thin layers during production and thus affect their function.

The results from thermal processing confirm the excellent stability of the material structure regarding such high temperatures. In particular, the ratio of the elements from EDS remained almost unaltered after processing and their weight differences varied within a percentage of units. Slight oxidation of contacts has been observed, but it can be assumed when using the cell only on Earth's terrestrial use. However, the roughness of the surface and the number of structural features, which were examined using the atomic force microscope, increased slightly. The thermal radiation of the cell in the case of reverse-bias has changed and increased. The high temperature resulted in the restructuring of defects, which were also observed from the dark characteristics. Fluctuations from PSD increased, and power performance from light curves decreased, which is a consequence of not only surface but also internal elementary processes. The solar cell remained functional even though the thermal stress was relatively at the high level of 350 °C for over 4 hours. However, with more prolonged annealing, an increasing incidence of defects and a consequent decrease in performance can be expected. A sudden change results under reverse bias after increasing the processing temperature of the solar cell to the limit of its functionality (420 °C). This change is in the form of an immediate electric breakdown.

In contrast to the thermal stress of 350 °C, the successful cooling to –120 °C with nitrogen and subsequent XPS analysis was performed, which also took place during cooling, as opposed to heating where measurements were achieved only before and after processing without XPS measurement. The optical properties of the solar cell after cooling were considered to be excellent and, due to the almost unchanged reflectivity, it was not necessary to measure the surface morphology using AFM. Raman spectroscopy also indicated a relatively high quality unchanged elemental composition. However, the degradation of the sample probably occurred, by reason

of negative thermal expansion and internal processes. The decrease in performance was confirmed by I-V and P-V characteristics. The main surface modification at cooling is connected with C – O bond. Partial degradation of Al – O bond is associated with dissociatively adsorbed oxygen [79]. Decreasing of dangling oxygen bonds can be connected with C – O local surface defects [80].

The most comprehensive part of the work from the standpoint of analysis can be considered intense irradiation of samples with the gamma emitter with a dose of 500 kGy. In exception to the EDS method and infrared camera observation, all analytical measurements and tools listed in Tab. 4.1, were used. Most of these methods used mutually confirmed differences in anti-reflection and protective layers, their diffusion and also the decrease in PV cell performance.

In results of irradiation by the continuous laser, summarized dependences of electrical properties on exposure duration show a slight increase in efficiency at 42th day of the experiment. The SL energy caused displacement defects by virtue of migration of Ti and Al atoms. A good agreement between functional (electrical), optical and structural properties was observed. The XPS spectra show the degradation of the protective  $\text{AlO}_x$  layer as well. Raman spectroscopy allows us to suggest that As sites are related to defects formation. Diffusion of Al and Ti caused the changing of interference fringes studied by reflectometry. The fact of element displacement, as well as the anisotropic character, were shown by SIMS. The current-voltage (Fig. 5.46 and 5.45a) and power characteristics (Fig. 5.45b) studied during SL illumination shows that electron traps that appear as the result irradiation can relax over time, and the bond between electrons and the lattice of the material becomes weaker. The traps originate from the displacement of an atom when the kinetic energy of radiation is sufficient, and Frankel pair can appear [81]. The minor carriers are responsible for the electrical behaviour of solar cell under illumination. Generation of electron-hole pair can be affected by defects of the material structure. Defects at the depletion region caused increasing of recombination current and indicated degradation of PN junction (Fig. 5.46). The decreasing in the concentration of charge carriers can be associated with the capture of charge carriers on the resulting defects. Low effective lifetime of carriers can also be connected with defects caused by the migration of Al and Ti atoms. Electrical characteristics demonstrate non-linear character of degradation. It was most probably by cause of the fact that including of Al caused the appearance of deep donor level centres (DX centres). Diffusion of titanium creates additional charge separation in the film. The phase transformation of the Ti – O superlattice from the anatase phase to rutile may occur at the interface, which contributes to a change in the efficiency [82]. In this case, Ti atoms are partially released from the structure, which is confirmed by SIMS.

The results of this work provide opportunities for new studies not only in the field of solar cells but also in semiconductors and thin-films, which have been shown to diffuse into the surface during various stress tests. The work is also a valuable source of information for the advanced production of PV cells specializing in space applications because GaAs solar cells directly designed for satellites were used here as well.

## References

1. WILSON, Gregory M. et al. *Journal of Physics D: Applied Physics*. Vol. 53, The 2020 photovoltaic technologies roadmap. IOP Publishing Ltd, 2020. No. 49. ISSN 13616463. Available from DOI: 10.1088/1361-6463/ab9c6a.
2. GEISZ, John F. et al. Six-junction III-V solar cells with 47.1% conversion efficiency under 143 Suns concentration. *Nature Energy*. 2020, vol. 5, pp. 326–335. ISSN 20587546. Available from DOI: 10.1038/s41560-020-0598-5.
3. SIMON, John et al. GaAs solar cells grown on intentionally contaminated GaAs substrates. *Journal of Crystal Growth*. 2020, vol. 541, p. 125668. ISSN 00220248. Available from DOI: 10.1016/j.jcrysgro.2020.125668.
4. LOO, Robert Y.; KAMATH, G. Sanjiv; LI, Sheng S. Radiation Damage and Annealing in GaAs Solar Cells. *IEEE Transactions on Electron Devices*. 1990, vol. 37, no. 2, pp. 485–497. ISSN 15579646. Available from DOI: 10.1109/16.46387.
5. PAPEŽ, Nikola et al. Degradation analysis of GaAs solar cells at thermal stress. *Applied Surface Science*. 2018, vol. 461, pp. 212–220. ISSN 01694332. Available from DOI: 10.1016/j.apsusc.2018.05.093.
6. PAPEŽ, Nikola et al. Performance analysis of GaAs based solar cells under gamma irradiation. *Applied Surface Science*. 2020, vol. 510. ISSN 01694332. Available from DOI: 10.1016/j.apsusc.2020.145329.
7. MING, Lu; RONG, Wang; KUI, Yang; TIANCHENG, Yi. Photoluminescence analysis of electron irradiation-induced defects in GaAs/Ge space solar cells. *Nuclear Instruments and Methods in Physics Research, Section B: Beam Interactions with Materials and Atoms*. 2013, vol. 312, pp. 137–140. ISSN 0168583X. Available from DOI: 10.1016/j.nimb.2013.07.006.
8. ORLOVA, Marina N.; YURCHUK, Sergey Yu.; DIDENKO, Sergey I.; TAPERO, Konstantin I. Study of degradation of photovoltaic cells based on A3B5 nanoheterostructures under ionizing radiation. *Modern Electronic Materials*. 2015, vol. 1, no. 2, pp. 60–65. ISSN 24521779. Available from DOI: 10.1016/j.moem.2016.01.003.
9. KESER, Ömer Faruk; IDARE, Buğrahan. Designing anti-reflective microlens arrays for space solar cells. *Solar Energy Materials and Solar Cells*. 2019, vol. 200, p. 110003. ISSN 09270248. Available from DOI: 10.1016/j.solmat.2019.110003.

10. MOON, Sunghyun et al. Highly efficient single-junction GaAs thin-film solar cell on flexible substrate. *Scientific Reports*. 2016, vol. 6, no. 1, pp. 1–6. ISSN 20452322. Available from DOI: 10.1038/srep30107.
11. HIRST, L. C. et al. Intrinsic radiation tolerance of ultra-thin GaAs solar cells. *Applied Physics Letters*. 2016, vol. 109, no. 3, p. 033908. ISSN 00036951. Available from DOI: 10.1063/1.4959784.
12. SWANSON, Richard M. *Progress in Photovoltaics: Research and Applications*. Vol. 14, A vision for crystalline silicon photovoltaics. John Wiley & Sons, Ltd, 2006. No. 5. ISSN 10627995. Available from DOI: 10.1002/pip.709.
13. SAYIGH, Ali. *Comprehensive renewable energy*. 1st ed. Elsevier, 2012. ISBN 978-0-08-087872-0. Available also from: <https://www.elsevier.com/books/comprehensive-renewable-energy/lletcher/978-0-08-087872-0>.
14. ALAJLANI, Yahya et al. Inorganic Thin Film Materials for Solar Cell Applications. In: *Reference Module in Materials Science and Materials Engineering*. Elsevier, 2018. Available from DOI: 10.1016/b978-0-12-803581-8.10355-8.
15. LIPIŃSKI, M.; PANEK, P. Optimisation of monocrystalline silicon solar cell. *Opto-electronics Review*. 2003, pp. 291–295.
16. SHAH, Arvind. Amorphous silicon solar cells. In: *Springer Series in Materials Science*. Springer, 2020, vol. 301, pp. 139–161. ISSN 21962812. Available from DOI: 10.1007/978-3-030-46487-5\_6.
17. PHILIPPS, Simon. *Photovoltaics Report* [online]. Freiburg, 2020 [visited on 2020-09-10]. Available from: <https://www.ise.fraunhofer.de/content/dam/ise/de/documents/publications/studies/Photovoltaics-Report.pdf>.
18. GIBSON, Elizabeth A. *Solar energy capture materials*. 2019. ISBN 978-1-78801-107-5.
19. KHARCHENKO, N. V.; KHARCHENKO, Vadym M. *Advanced energy systems*. [N.d.]. ISBN 9781439886588.
20. SAFYANU, Bashir Danjuma; ABDULLAH, Mohd Noor; OMAR, Zamri. *Journal of Aerospace Technology and Management*. Vol. 11, Review of power device for solar-powered aircraft applications. *Journal of Aerospace Technology and Management*, 2019. ISSN 21759146. Available from DOI: 10.5028/jatm.v11.1077.
21. IKEGAMI, T. (Tetsuhiko); HASEGAWA, F.; TAKEDA, Y.; INSTITUTE OF PHYSICS (GREAT BRITAIN). *Gallium arsenide and related compounds 1992*. Institute of Physics, 1993. ISBN 9780750302500.

22. TAYLOR, Richard A.; RAMASAMY, Karthik. Colloidal quantum dots solar cells. *SPR Nanoscience*. 2017, vol. 4, pp. 142–168. ISBN 9781782621591. ISSN 2049355X. Available from DOI: 10.1039/9781782620358-00142.
23. ZAHARIA, Catalin. Polymer solar cells. In: *Sustainable Practices: Concepts, Methodologies, Tools, and Applications*. IGI Global, 2013, vol. 1, pp. 365–383. ISBN 9781466648531. Available from DOI: 10.4018/978-1-4666-4852-4.ch020.
24. BEELER, Richard et al. Comparative study of InGaAs integration on bulk Ge and virtual Ge/Si(1 0 0) substrates for low-cost photovoltaic applications. *Solar Energy Materials and Solar Cells*. 2010, vol. 94, no. 12, pp. 2362–2370. ISSN 09270248. Available from DOI: 10.1016/j.solmat.2010.08.016.
25. YAMAGUCHI, Masafumi; TAKAMOTO, Tatsuya; ARAKI, Kenji; EKINS-DAUKES, Nicholas. Multi-junction III-V solar cells: Current status and future potential. *Solar Energy*. 2005, vol. 79, no. 1, pp. 78–85. ISSN 0038092X. Available from DOI: 10.1016/j.solener.2004.09.018.
26. *Structure of a MJ Solar cell* [online]. 2010 [visited on 2020-09-10]. Available from: <https://commons.wikimedia.org/wiki/File:StructureMJetspectre.png>.
27. PHAM, Thanh Tuan; VU, Ngoc Hai; SHIN, Seoyong. Design of Curved Fresnel Lens with High Performance Creating Competitive Price Concentrator Photovoltaic. In: *Energy Procedia*. Elsevier Ltd, 2018, vol. 144, pp. 16–32. ISSN 18766102. Available from DOI: 10.1016/j.egypro.2018.06.004.
28. Linear Fresnel lens concentrators. *Solar Energy*. 1975, vol. 17, no. 5, pp. 285–289. ISSN 0038092X. Available from DOI: 10.1016/0038-092X(75)90045-6.
29. ASTE, N. et al. Performance analysis of a large-area luminescent solar concentrator module. *Renewable Energy*. 2015, vol. 76, pp. 330–337. ISSN 18790682. Available from DOI: 10.1016/j.renene.2014.11.026.
30. ZHAO, Yimu; LUNT, Richard R. Transparent luminescent solar concentrators for large-area solar windows enabled by massive stokes-shift nanocluster phosphors. *Advanced Energy Materials*. 2013, vol. 3, no. 9, pp. 1143–1148. ISSN 16146832. Available from DOI: 10.1002/aenm.201300173.
31. JORGENSEN, Gary et al. Advanced reflector materials for solar concentrators. *stct*. 1994, pp. 26–30.

32. HOHEISEL, R. et al. Solar cell experiments for space: past, present and future. In: *Physics, Simulation, and Photonic Engineering of Photovoltaic Devices II*. SPIE, 2013, vol. 8620, 86200U. ISBN 9780819493897. ISSN 0277786X. Available from DOI: 10.1117/12.2006087.
33. On-Orbit Operations of A Power System for Japan's Venus Explorer Akatsuki. In: *E3S Web of Conferences*. EDP Sciences, 2017, vol. 16. ISSN 22671242. Available from DOI: 10.1051/e3sconf/20171618004.
34. LAURETTA, D. S. et al. *Space Science Reviews*. Vol. 212, OSIRIS-REx: Sample Return from Asteroid (101955) Bennu. Springer Netherlands, 2017. No. 1-2. ISSN 15729672. Available from DOI: 10.1007/s11214-017-0405-1.
35. WALDMEIER, M. Ergebnisse und Probleme der Sonnenforschung. *Quarterly Journal of the Royal Meteorological Society*. 1956, vol. 82, no. 351, pp. 118–118. ISSN 00359009. Available from DOI: 10.1002/qj.49708235128.
36. CARROLL, Bradley W.; OSTLIE, Dale A. *An introduction to modern astrophysics*. Pearson Addison-Wesley, 2007. ISBN 9780805304022.
37. SMIL, Václav. *The earth's biosphere: evolution, dynamics, and change*. MIT Press, 2002. ISBN 9780262194723.
38. COTAL, Hector et al. *Energy and Environmental Science*. Vol. 2, III-V multi-junction solar cells for concentrating photovoltaics. The Royal Society of Chemistry, 2009. No. 2. ISSN 17545692. Available from DOI: 10.1039/b809257e.
39. SPITZER, Lyman. *Physical processes in the interstellar medium*. Wiley, 1998. ISBN 9780471293354.
40. PRIALNIK, Dina. *An introduction to the theory of stellar structure and evolution*. Cambridge University Press, 2010. ISBN 9780521866040.
41. TINSLEY, James R.; MOY, Kenneth J.; TUNNELL, Laura. Cobalt 60 as a marking agent. In: *Hard X-Ray/Gamma-Ray and Neutron Optics, Sensors, and Applications*. SPIE, 1996, vol. 2859, pp. 307–312. Available from DOI: 10.1117/12.245121.
42. STANCULESCU, A. The Role of Nuclear Power and Nuclear Propulsion in the Peaceful Exploration of Space. *International Atomic Energy Agency*. 2005. ISBN 9201074042.
43. KUKHARKIN, N. E.; PONOMAREV-STEPNOI, N. N.; USOV, V. A. Nuclear Power Sources for Space Systems. In: *Handbook of Nuclear Chemistry*. Springer US, 2011, pp. 2731–2758. Available from DOI: 10.1007/978-1-4419-0720-2\_59.



44. SIMPSON, J. A. Elemental and isotopic composition of the galactic cosmic rays. *Annual Review of Nuclear and Particle Science*. 1983, vol. 33, pp. 323–381. ISSN 01638998. Available from DOI: 10.1146/annurev.ns.33.120183.001543.
45. HAMDI, Roshen Tariq Ahmed; ABDULHADI, Sanaa; KAZEM, Hussein A; CHAICHAN, Miqdam Tariq. Humidity impact on photovoltaic cells performance: A review. *International Journal of Recent Engineering Research and Development*. 2018, vol. 3, no. 11, pp. 27–37. ISSN 2455-8761.
46. QI, Lei et al. Thermal-stress distribution and damage characteristics of three-junction GaAs solar cell irradiated by continuous laser beam. *Optik*. 2019. ISSN 00304026. Available from DOI: 10.1016/j.ijleo.2019.163284.
47. KRAUSS, Karin; FERTIG, Fabian; MENZEL, Dorothee; REIN, Stefan. Light-induced Degradation of Silicon Solar Cells with Aluminiumoxide Passivated Rear Side. In: *Energy Procedia*. 2015. ISSN 18766102. Available from DOI: 10.1016/j.egypro.2015.07.086.
48. MALETZ, Jörg; STEINER, Michael; FATKA, Oldřich. Middle Cambrian pterobranchs and the Question: What is a graptolite? *Lethaia*. 2005, vol. 38, no. 1, pp. 73–85. ISSN 00241164. Available from DOI: 10.1080/00241160510013204.
49. NASRAZADANI, Seifollah; HASSANI, Shokrollah. Modern analytical techniques in failure analysis of aerospace, chemical, and oil and gas industries. In: *Handbook of Materials Failure Analysis with Case Studies from the Oil and Gas Industry*. Elsevier Inc., 2016, pp. 39–54. ISBN 9780081001264. Available from DOI: 10.1016/B978-0-08-100117-2.00010-8.
50. TAMRAKAR, Vivek; S.C, Gupta; SAWLE, Yashwant. Single-Diode and Two-Diode Pv Cell Modeling Using Matlab For Studying Characteristics Of Solar Cell Under Varying Conditions. *Electrical & Computer Engineering: An International Journal*. 2015, vol. 4, no. 2, pp. 67–77. Available from DOI: 10.14810/ecij.2015.4207.
51. ROSA-CLOT, Marco; TINA, Giuseppe Marco. Introduction to PV Plants. In: *Submerged and Floating Photovoltaic Systems*. Elsevier, 2018, pp. 33–64. Available from DOI: 10.1016/b978-0-12-812149-8.00003-x.
52. WUNDERLICH, J. et al. Spin-injection Hall effect in a planar photovoltaic cell. *Nature Physics*. 2009, vol. 5, no. 9, pp. 675–681. ISSN 17452481. Available from DOI: 10.1038/nphys1359.

53. BOUZIDI, K.; CHEGAAR, Mohamed; AILLERIE, Michel. Solar Cells Parameters Evaluation from Dark I-V Characteristics. *Energy Procedia*. 2012, vol. 18, pp. 1601–1610. ISSN 1876-6102. Available from DOI: <https://doi.org/10.1016/j.egypro.2012.06.001>. Terragreen 2012: Clean Energy Solutions for Sustainable Environment (CESSE).
54. BREITENSTEIN, O. Understanding the current-voltage characteristics of industrial crystalline silicon solar cells by considering inhomogeneous current distributions. *Opto-electronics Review*. 2013, vol. 21, no. 3, pp. 259–282. ISSN 18963757. Available from DOI: [10.2478/s11772-013-0095-5](https://doi.org/10.2478/s11772-013-0095-5).
55. DENNIS, Tasshi. Full-spectrum optical-beam-induced current for solar cell microscopy and multi-junction characterization. In: *Conference Record of the IEEE Photovoltaic Specialists Conference*. 2013. ISBN 9781479932993. ISSN 01608371. Available from DOI: [10.1109/PVSC.2013.6744104](https://doi.org/10.1109/PVSC.2013.6744104).
56. WATANABE, Kentaroh et al. Open-circuit-voltage enhancement of the III-V super-lattice solar cells under optical concentration. In: *AIP Conference Proceedings*. American Institute of Physics AIP, 2012, vol. 1477, pp. 40–43. No. 1. ISBN 9780735410862. ISSN 0094243X. Available from DOI: [10.1063/1.4753829](https://doi.org/10.1063/1.4753829).
57. HOVELL, Harold J. *Semiconductors and semimetals*. Academic Press, 1975. ISBN 9780127521114.
58. SHANG, Aixue; LI, Xiaofeng. Photovoltaic Devices: Opto-Electro-Thermal Physics and Modeling. *Advanced Materials*. 2017, vol. 29, no. 8. ISSN 15214095. Available from DOI: [10.1002/adma.201603492](https://doi.org/10.1002/adma.201603492).
59. MACKŮ, Robert. *Analýza fluktuálních procesů v solárních článcích*. 2011. Doctoral thesis. Brno University of Technology.
60. MARINOV, Ognian; DEEN, M. Jamal; TEJADA, Juan Antonio Jimenez. Theory of microplasma fluctuations and noise in silicon diode in avalanche breakdown. *Journal of Applied Physics*. 2007, vol. 101, no. 6. ISSN 00218979. Available from DOI: [10.1063/1.2654973](https://doi.org/10.1063/1.2654973).
61. MOUSNIER, M. et al. Lock-in thermography for defect localization and thermal characterization for space application. *Microelectronics Reliability*. 2018, vol. 88-90, pp. 67–74. ISSN 00262714. Available from DOI: [10.1016/j.microrel.2018.07.014](https://doi.org/10.1016/j.microrel.2018.07.014).
62. ZHANG, Shenyi et al. First measurements of the radiation dose on the lunar surface. *Science Advances*. 2020, vol. 6, no. 39. ISSN 2375-2548. Available from DOI: [10.1126/sciadv.aaz1334](https://doi.org/10.1126/sciadv.aaz1334).

63. HARTL, I. et al. Ultrahigh-resolution optical coherence tomography using continuum generation in an air–silica microstructure optical fiber. *Optics Letters*. 2001. ISSN 0146-9592. Available from DOI: 10.1364/ol.26.000608.
64. TAMURA, Kohichi R.; KUBOTA, Hirokazu; NAKAZAWA, Masataka. Fundamentals of stable continuum generation at high repetition rates. *IEEE Journal of Quantum Electronics*. 2000. ISSN 00189197. Available from DOI: 10.1109/3.848347.
65. DUNSBY, C.; FRENCH, P. M.W. Biophotonics applications of supercontinuum generation. In: *Supercontinuum Generation in Optical Fibers*. 2010. ISBN 9780511750465. Available from DOI: 10.1017/CB09780511750465.016.
66. KIM, Minjung; CHELIKOWSKY, James R. Simulated non-contact atomic force microscopy for GaAs surfaces based on real-space pseudopotentials. *Applied Surface Science*. 2014, vol. 303, pp. 163–167. ISSN 0169-4332. Available from DOI: <https://doi.org/10.1016/j.apsusc.2014.02.127>.
67. ŠKVARENINA, L. et al. Noise fluctuation changes related to edge deletion of thin-film Cu(In,Ga)Se<sub>2</sub> solar cells. In: *2017 International Conference on Noise and Fluctuations (ICNF)*. 2017, pp. 1–4. Available from DOI: 10.1109/ICNF.2017.7986025.
68. YANG, V. K. et al. Crack formation in GaAs heteroepitaxial films on Si and SiGe virtual substrates. *Journal of Applied Physics*. 2003, vol. 93, no. 7, pp. 3859–3865. ISSN 00218979. Available from DOI: 10.1063/1.1558963.
69. SOMA, Toshinobu. Thermal Expansion Coefficient of Si and Ge. *Journal of the Physical Society of Japan*. 1977, vol. 42, no. 5, pp. 1491–1494. ISSN 13474073. Available from DOI: 10.1143/JPSJ.42.1491.
70. QUAGLIANO, Lucia G. Detection of As<sub>2</sub>O<sub>3</sub> arsenic oxide on GaAs surface by Raman scattering. *Applied Surface Science*. 2000, vol. 153, no. 4, pp. 240–244. ISSN 0169-4332. Available from DOI: [https://doi.org/10.1016/S0169-4332\(99\)00355-4](https://doi.org/10.1016/S0169-4332(99)00355-4).
71. KAYA, Senol; JAKSIC, Aleksandar; YILMAZ, Ercan. Co-60 gamma irradiation effects on electrical characteristics of HfO<sub>2</sub> MOSFETs and specification of basic radiation- induced degradation mechanism. *Radiation Physics and Chemistry*. 2018, vol. 149, pp. 7–13. ISSN 0969-806X. Available from DOI: <https://doi.org/10.1016/j.radphyschem.2018.03.007>.
72. LIN, J. Y.; DISSANAYAKE, A.; JIANG, H. X. DX centers in Al<sub>0.34</sub>Ga<sub>0.66</sub>As amorphous thin films. *Solid State Communications*. 1993. ISSN 00381098. Available from DOI: 10.1016/0038-1098(93)90414-I.

73. DALLAEVA, D. S. et al. Structural properties of Al<sub>2</sub>O<sub>3</sub>/AlN thin film prepared by magnetron sputtering of Al in HF-activated nitrogen plasma. *Thin Solid Films*. 2012. ISSN 00406090. Available from DOI: 10.1016/j.tsf.2012.11.023.
74. SONG, Tingting et al. Fabrication of super slippery sheet-layered and porous anodic aluminium oxide surfaces and its anticorrosion property. *Applied Surface Science*. 2015. ISSN 01694332. Available from DOI: 10.1016/j.apsusc.2015.07.140.
75. WAGNER, J. et al. N-induced vibrational modes in GaAsN and GaInAsN studied by resonant Raman scattering. *Journal of Applied Physics*. 2001. ISSN 00218979. Available from DOI: 10.1063/1.1412277.
76. ŠKARVADA, Pavel et al. A variety of microstructural defects in crystalline silicon solar cells. In: *Applied Surface Science*. 2014. ISSN 01694332. Available from DOI: 10.1016/j.apsusc.2014.05.064.
77. CHOU, Y. C. et al. On the investigation of gate metal interdiffusion in GaAs HEMTs. In: *Technical Digest - GaAs IC Symposium (Gallium Arsenide Integrated Circuit)*. 2003. Available from DOI: 10.1109/gaas.2003.1252362.
78. BERECHMAN, Ronen A.; REVZIN, Boris; SHAPIRA, Yoram. Correlating gate sinking and electrical performance of pseudomorphic high electron mobility transistors. *Microelectronics Reliability*. 2007. ISSN 00262714. Available from DOI: 10.1016/j.microrel.2006.08.020.
79. PASHUTSKI, A.; HOFFMAN, A.; FOLMAN, M. Low temperature XPS and AES studies of O<sub>2</sub> adsorption on Al(100). *Surface Science Letters*. 1989. ISSN 01672584. Available from DOI: 10.1016/0167-2584(89)90566-5.
80. HERMANN, K.; GUMHALTER, B.; WANDEL, K. Perturbation of the adsorbate electronic structure by local fields at surface defects. *Surface Science*. 1991. ISSN 00396028. Available from DOI: 10.1016/0039-6028(91)91163-R.
81. PONST, D.; BOURGOINT, J. C. *Journal of Physics C: Solid State Physics*. Irradiation-induced defects in gaas. 1985. ISSN 00223719. Available from DOI: 10.1088/0022-3719/18/20/012.
82. VASAN, R.; MAKABLEH, Y. F.; MANASREH, M. O. Comparison of anti-reflective properties of single layer anatase and rutile TiO<sub>2</sub> on GaAs based solar cells. In: *MRS Advances*. 2016. ISSN 20598521. Available from DOI: 10.1557/adv.2016.116.

## List of units

Unit	Description	Notation
A	electric current	ampere
a.u.	ratio of intensity amount	arbitrary unit
at%	concentration of dopant atoms	atomic percentage
Bq	activity or quantity of radioactive material	becquerel
°C	Celsius temperature	degree Celsius
eV	amount of kinetic to move an electron across a electric potential difference of 1 V	electronvolt
Gy	absorbed dose, absorbed dose index	gray
Hz	frequency	hertz
K	absolute temperature or thermodynamic tem- perature	kelvin
Pa	internal pressure or stress	pascal
px	point in a raster image	pixel
m <sup>-1</sup>	Raman shift	reciprocal metres
s	unit of time	second
A <sup>2</sup> Hz <sup>-1</sup>	unit of current spectral density	square current of the noise signal
Torr	unit of pressure defined as 1 standard atmo- sphere divided by 760	torr
V	voltage, electric pressure, electric tension or electric potential difference	volt
W	1 joule of work performed in 1 second	watt
W/m <sup>2</sup>	power density, heat flux density, irradiance	watt per square metre
wt%	mass fraction of the species times 100	weight percentage

# List of symbols

Symbol	Description	Unit
$A$	area of the solar cell	$\text{m}^2$
$a_0$	distance between the Earth and the Sun: $149\,600 \times 10^6$	m
$A_{\text{BULK}}$	absorbance of the bulk PV cell	– / %
$E_{\text{ABS}}$	total solar irradiance	$\text{W}/\text{m}^2$
$E_c$	conduction band	eV
$E_F$	Fermi level	eV
$E_g$	energy bandgap	eV
$E_i$	intrinsic energy	eV
$E_{\text{ph}}$	photon energy	eV
$E_s$	flux density on Earth's orbit: 1367	$\text{W}/\text{m}^2$
$E_v$	valence band	eV
$\vec{E}_1^0$	electric field from an electromagnetic incident wave	$\text{V m}^{-1}$
$\vec{E}_1$	external electric field	$\text{V m}^{-1}$
$FF$	fill factor	–
$I_0$	diode saturation current	A
$I_L$	generated photocurrent	A
$I_m$	maximum current	A
$I_{\text{ph}}$	output current of PV cell	V
$I_{\text{sc}}$	short-circuit current	A
$I_{\text{th}}$	noise current	A
$J_{\text{sc}}$	short-circuit current density	$\text{A m}^{-2}$
$k$	Boltzmann constant: $1.380\,649 \times 10^{-23}$	$\text{J K}^{-1}$
$\vec{k}_1$	wavevector of incident wave	$\text{m}^{-1}$
$L_{\odot}$	solar luminosity constant: $3.828 \times 10^{26}$	W
$n$	ideality factor of diode	–
$n_s$	number of PV cells in series	–
$P_m$	maximum power	W
$\vec{P}$	polarisation vector	$\text{C m}^{-2}$
$R$	electrical resistance	$\Omega$
$r$	distance from the Sun	m
$R_p$	shunt resistance	$\Omega$
$R_s$	series resistance	$\Omega$
$\vec{r}$	incident wave position	–
$R_{\oplus}$	radius of the Earth: $6371 \times 10^3$	m
$R_{\odot}$	radius of the Sun: $696\,340 \times 10^3$	m

Symbol	Description	Unit
$S_a$	average roughness	nm
$S_C$	solar constant	–
$S_i$	current spectral density	$A^2 Hz^{-1}$
$S_{ku}$	kurtosis	–
$S_{sk}$	skewness	–
$S_u$	voltage spectral density	$V^2 Hz^{-1}$
$T$	absolute temperature	K
$t$	time	s
$T_{AR}$	transmittance of the anti-reflective coating	– / %
$T_{\oplus}$	effective temperature of the Earth: 254.33	K
$T_{\odot}$	effective temperature of the Sun: 5780	K
$U_{th}$	noise voltage	V
$V_m$	maximum voltage	V
$V_{oc}$	open-circuit voltage	V
$V_{pv}$	output voltage of PV cell	V
$V_T$	thermal voltage	V
$\Delta E_c$	conduction band offset	eV
$\Delta E_v$	valence band offset	eV
$\Delta f$	frequency bandwidth	Hz
$\alpha$	albedo of the Earth: 0.3	– / %
$\eta$	efficiency of the solar cell	– / %
$\sigma$	Stefan–Boltzmann constant: $5.67 \times 10^{-8}$	$W m^{-2} K^4$
$\chi$	electric susceptibility	–
$\omega_1$	angular frequency of incident wave	Hz

# List of acronyms

---

Acronym	Description
2DHG	Two-Dimensional Electron Gas
2DHG	Two-Dimensional Hole Gas
ADC	Analogue-to-digital converter
AM	Amplitude Modulation
AM1.5	Air Mass coefficient fo terrestrial PV cells
BF	Bright-Field
BSE	Backscattered Electrons
CCD	Charge-Coupled Device
CIGS	Copper Indium Gallium Selenide
CIS	Copper Indium Selenide
CMB	Cosmic Microwave Background
CME	Coronal Mass Ejection
CPV	Concentrator Photovoltaics
CPVT	Concentrated Photovoltaic Thermal system
DML	Dynamic Mechanical Load
EBIC	Electron-Beam-Induced Current
ECHA	European Chemicals Agency
EDS	Energy-Dispersive X-ray Spectroscopy
EDX	see EDS
ESA	European Space Agency
FET	Field-Effect Transistors
FM	Frequency modulation
FTIR	Fourier-Transform Infrared Spectroscopy
FWHM	Full Width at Half Maximum
GCR	Galactic Cosmic Rays
GPHS	General Purpose Heat Source
HCPV	High Concentration Photovoltaics

---



---

<b>Acronym</b>	<b>Description</b>
HEMT	High Electron Mobility Transistor
ISS	International Space Station
LCD	Liquid Crystal Display
LO	Longitudinal Optical
LSC	Luminescent Solar Concentrator
LWRHU	Light-Weight Radioisotope Heater Unit
MJ	Multijunction
MPP	Maximum Power Point
NIR	Near Infrared
POE	Primary Optical Element
PSD	Power Spectral Density
PV	Photovoltaic
PV-EBIC	Plain-View Electron-Beam-Induced Current
QDSC	Quantum Dot Solar Cell
RTG	Radioisotope Thermoelectric Generator
SAC	Sample Analysis Chamber
SEH	Solar Energy Harvesting
SEM	Scanning Electron Microscope
SIMS	Secondary Ion Mass Spectrometry
SL	Supercontinuum Laser
SOE	Secondary Optical Element
SPE	Solar Particle Events
TCU	Temperature Control Unit
TO	Transverse Optical
UVA	Ultraviolet A
VIS	Visible

---

---

<b>Acronym</b>	<b>Description</b>
X-EBIC	Cross-sectional Electron-Beam-Induced Current
XPS	X-ray Photoelectron Spectroscopy

---

# List of used instruments

## BASEBAND ANALYSER

- Rohde & Schwarz FMU36

## ELECTRON MICROSCOPE

- FEI Helios NanoLab 660
  - FIB setup
  - STEM detector
- FEI Verios 460L
- TESCAN LYRA3, 2nd generation
  - EDS detector: Oxford Instruments X-Max 50
  - BSE detector
  - EBIC setup

## FOURIER-TRANSFORM INFRARED SPECTROMETER

- Bruker Hyperion 3000

## INFRARED CAMERA

- Micro-Epsilon TIM 160

## MONOCHROME CCD CAMERA

- Moravian Instruments G2-3200 Mark II

## OPTICAL SPECTROMETER

- Ocean optics JAZ 3-channel

## POWER SOURCE UNIT

- Agilent E3631A
- Keithley 2420
- Keithley 2510-AT
- Keithley 6220
- PXI-4130 module

## RAMAN IMAGING SYSTEM

- WITec alpha300 R
- Renishaw inVia

#### SCANNING PROBE MICROSCOPE

- Bruker Dimension Icon
- NTEGRA Prima

#### SECONDARY ION MASS SPECTROSCOPY

- IONTOF TOF-SIMS 5

#### SIGNAL RECOVERY

- Ametek Model 5184 Ultra Low-Noise Preamplifier

#### SPECTROSCOPIC ELLIPSOMETER

- J. A. Woollam V-VASE

#### X-RAY PHOTOELECTRON SPECTROMETER

- Kratos Analytical Axis Supra
  - Heat & Cool setup



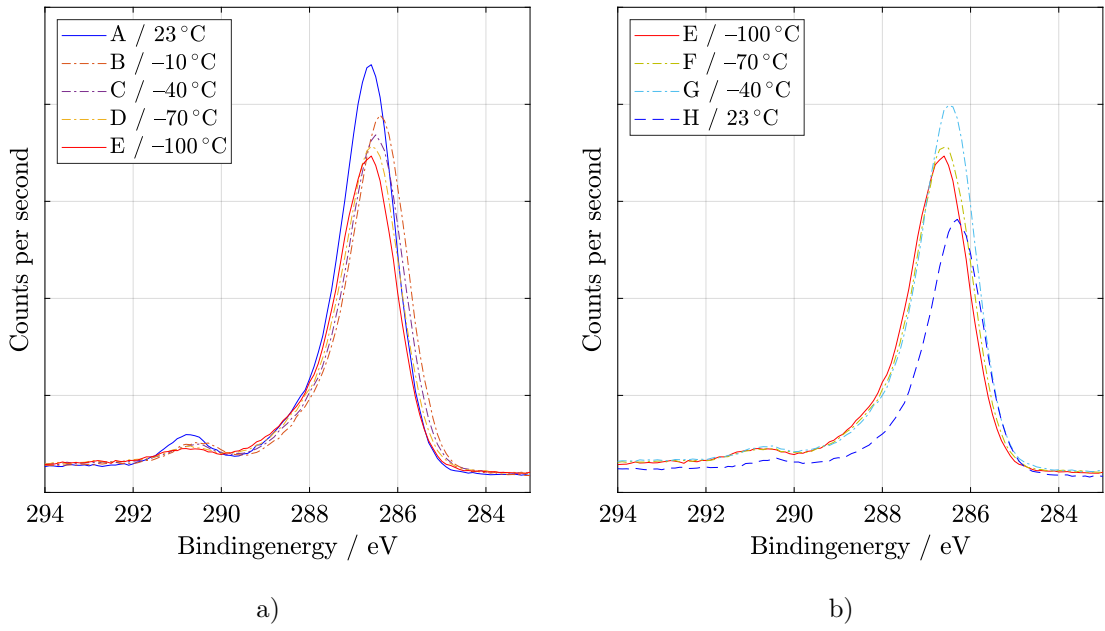


Fig. A.2: XPS observing during slow cooling process for C1s during a) cooling to  $-100^{\circ}\text{C}$  and subsequently b) return back to room temperature.

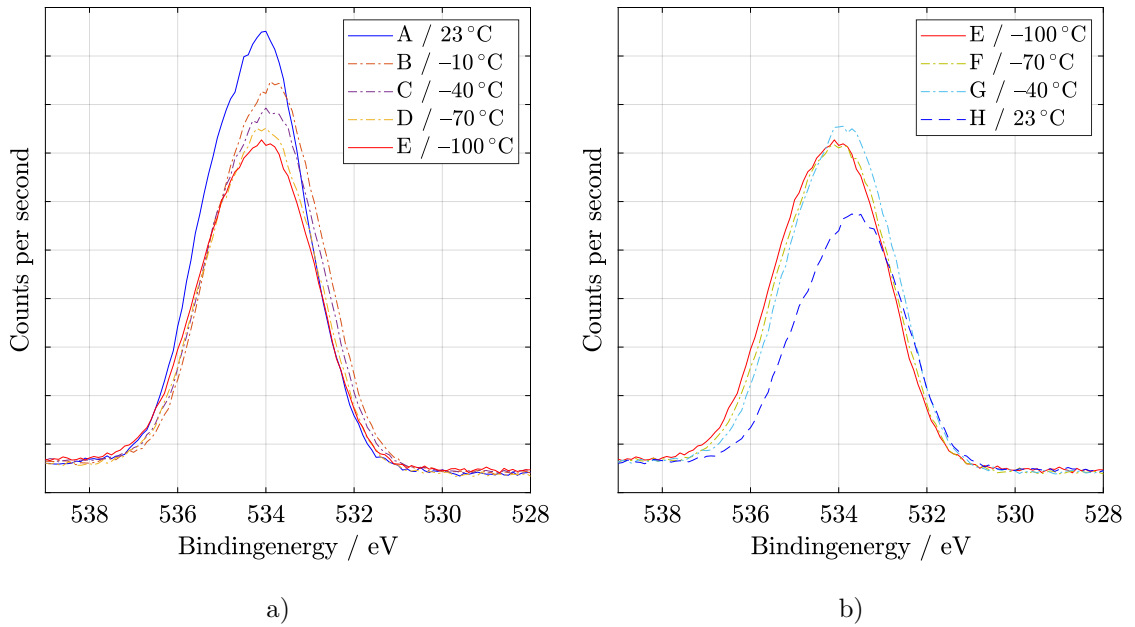


Fig. A.3: XPS observing during slow cooling process for O1s during a) cooling to  $-100^{\circ}\text{C}$  and subsequently b) return back to room temperature.

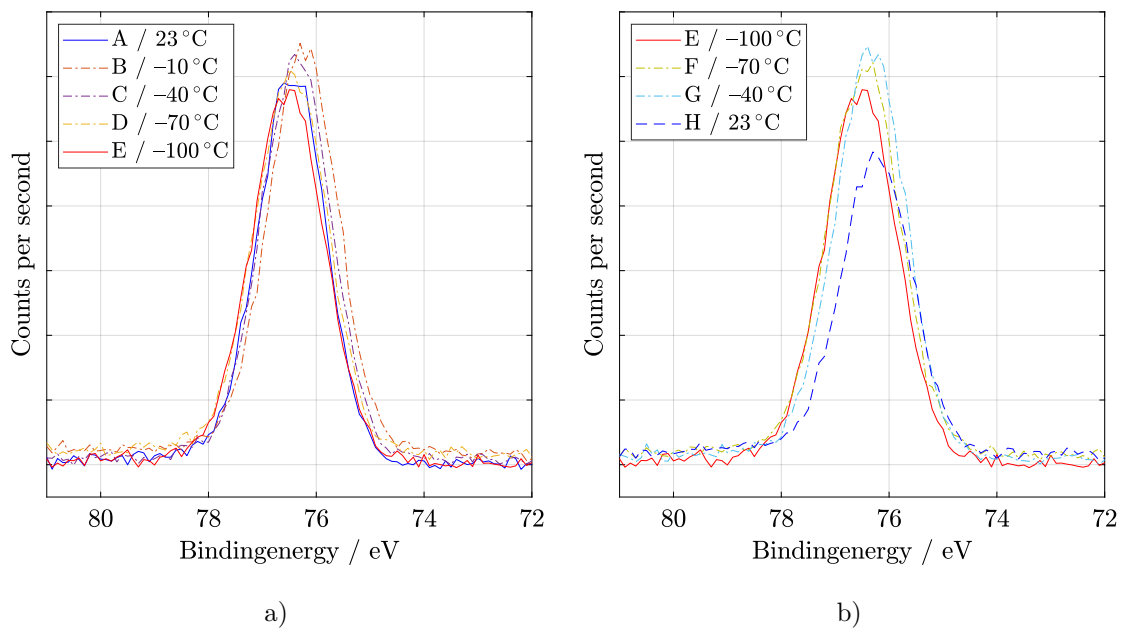


Fig. A.4: XPS observing during slow cooling process for Al<sub>2</sub>p during a) cooling to -100°C and subsequently b) return back to room temperature.

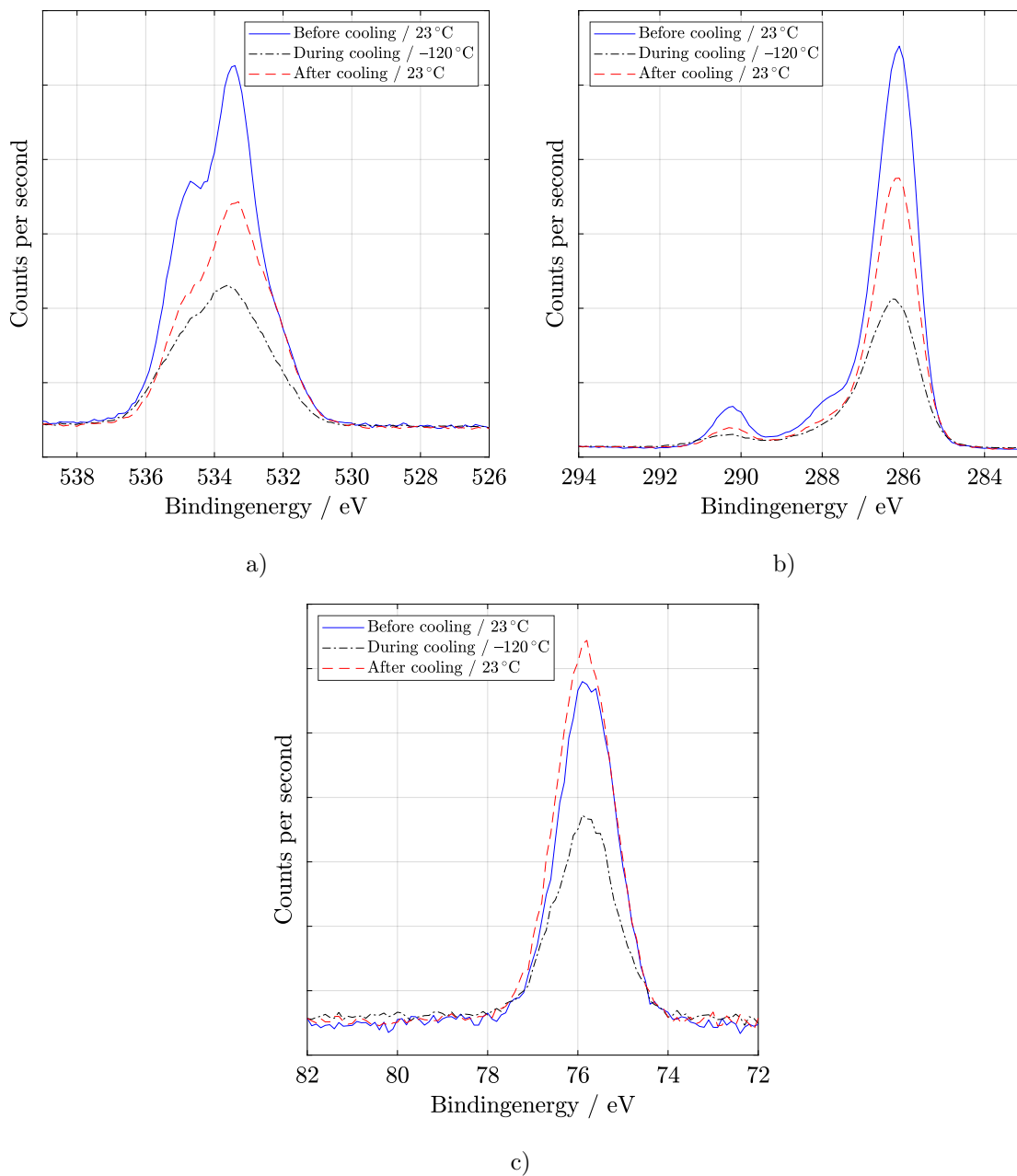


Fig. A.5: XPS observing during fast cooling process ( $-120^{\circ}\text{C}$ ) of a) O1s, b) C1s and c) Al2p high resolution spectra.



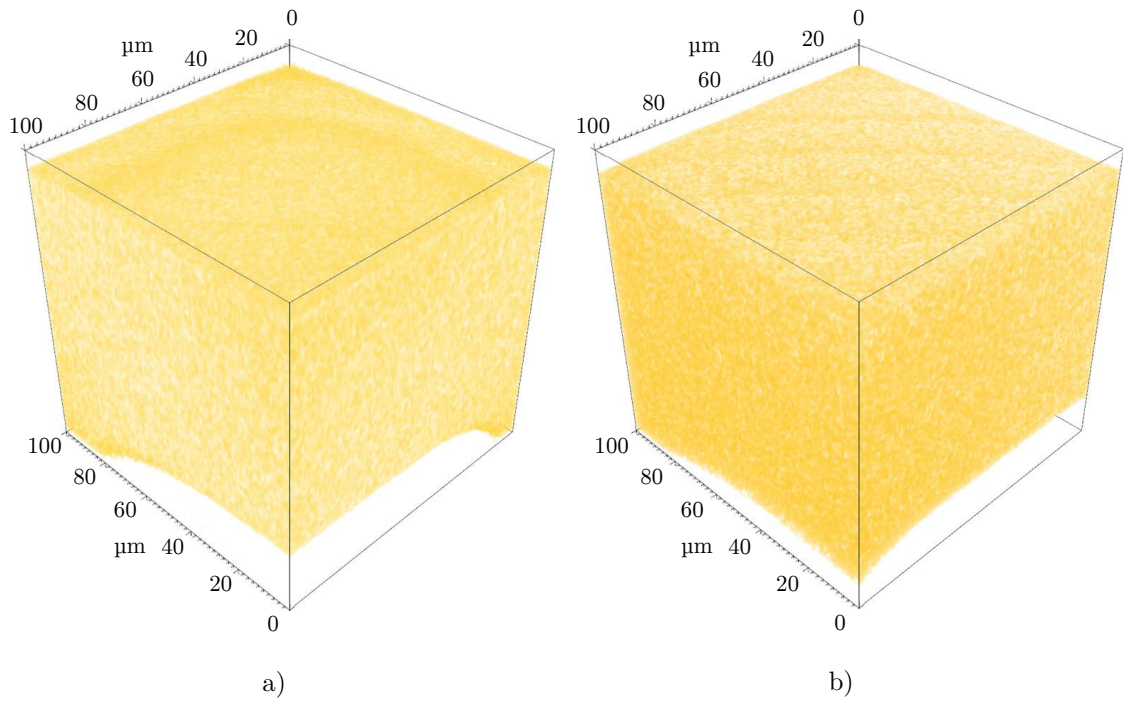


Fig. A.6: Three-dimensional visualisation of the elemental distribution of gallium a) before and b) after irradiation with the  $^{60}\text{Co}$  isotope investigated by SIMS .

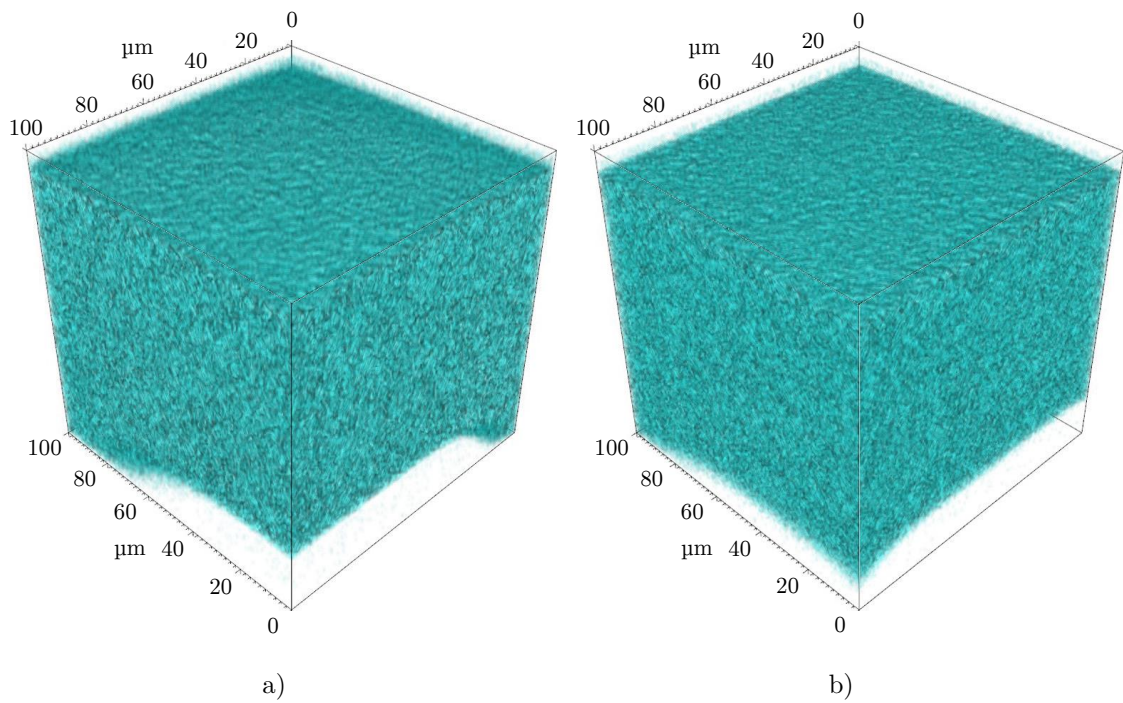


Fig. A.7: Three-dimensional visualisation of the elemental distribution of arsenic a) before and b) after irradiation with the  $^{60}\text{Co}$  isotope investigated by SIMS.

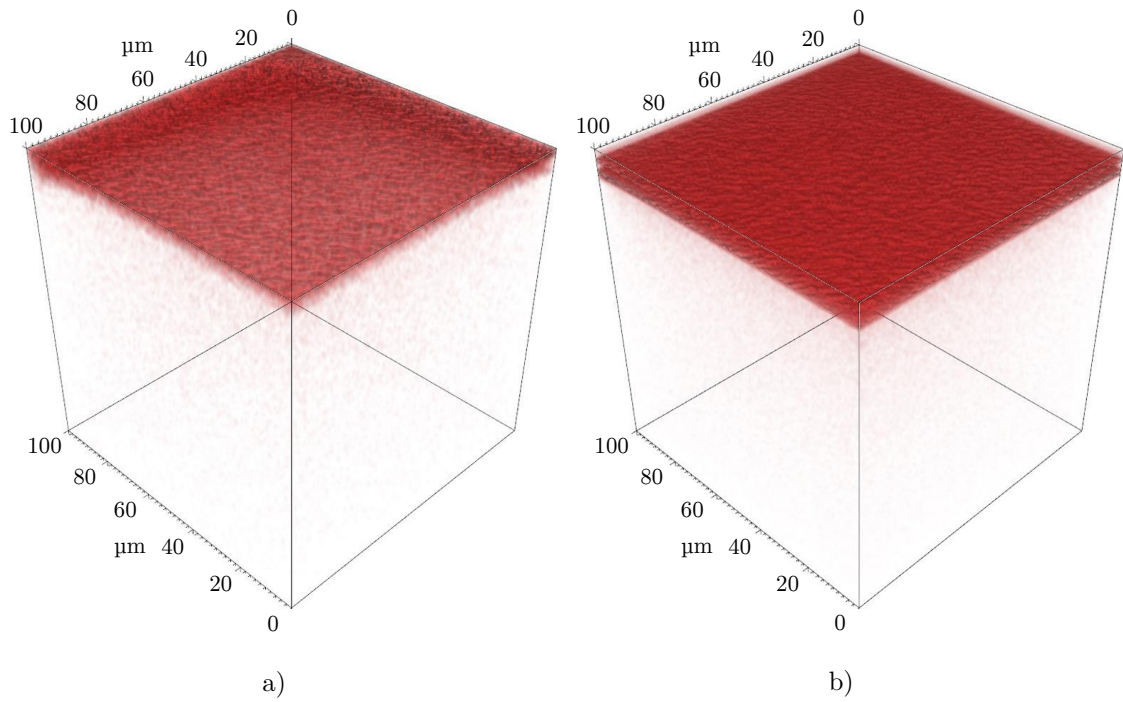


Fig. A.8: Three-dimensional visualisation of the elemental distribution of aluminium a) before and b) after irradiation with the  $^{60}\text{Co}$  isotope investigated by SIMS.

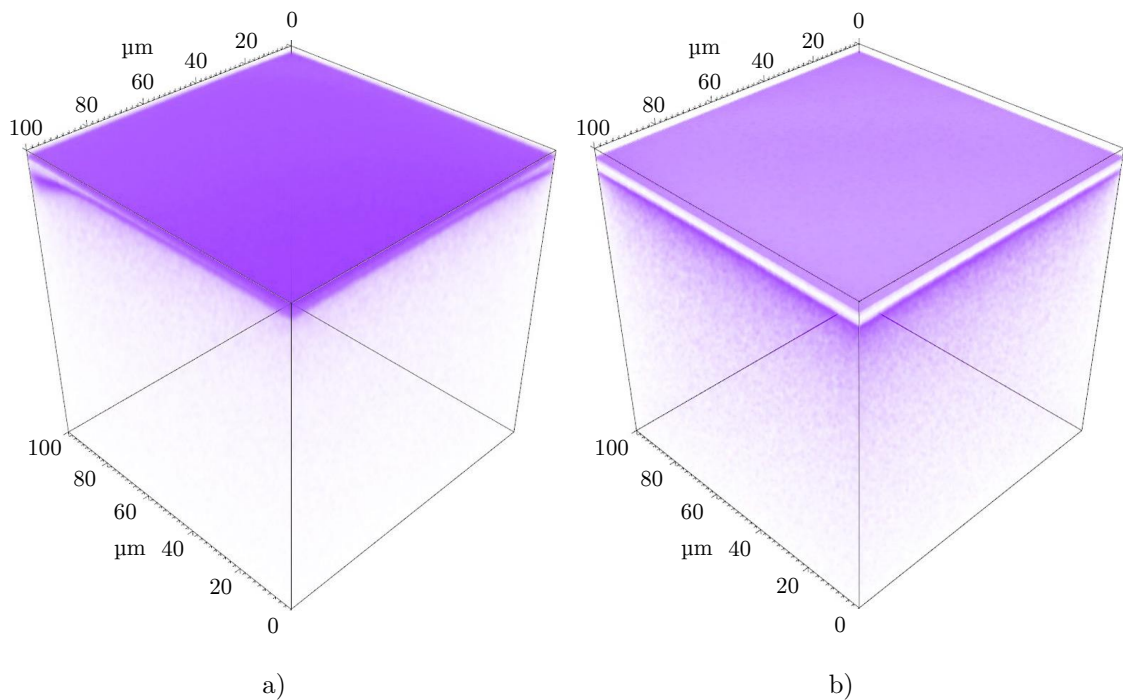


Fig. A.9: Three-dimensional visualisation of the elemental distribution of titanium a) before and b) after irradiation with the  $^{60}\text{Co}$  isotope investigated by SIMS.

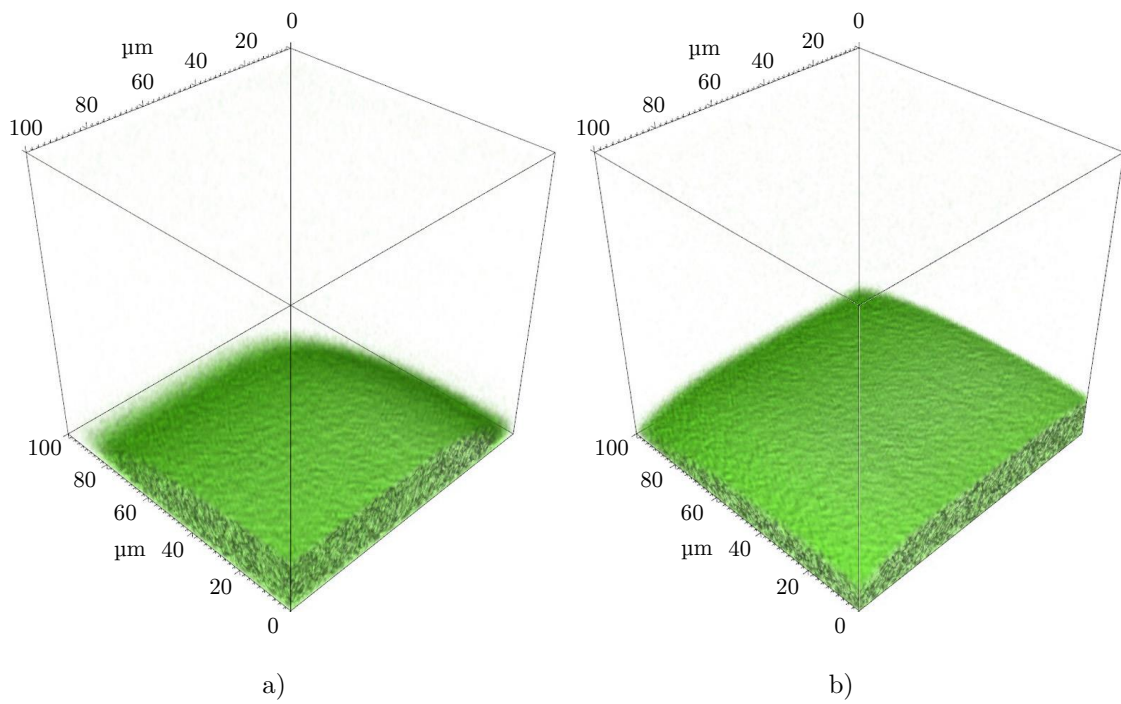


Fig. A.10: Three-dimensional visualisation of the elemental distribution of germanium a) before and b) after irradiation with the  $^{60}\text{Co}$  isotope investigated by SIMS.



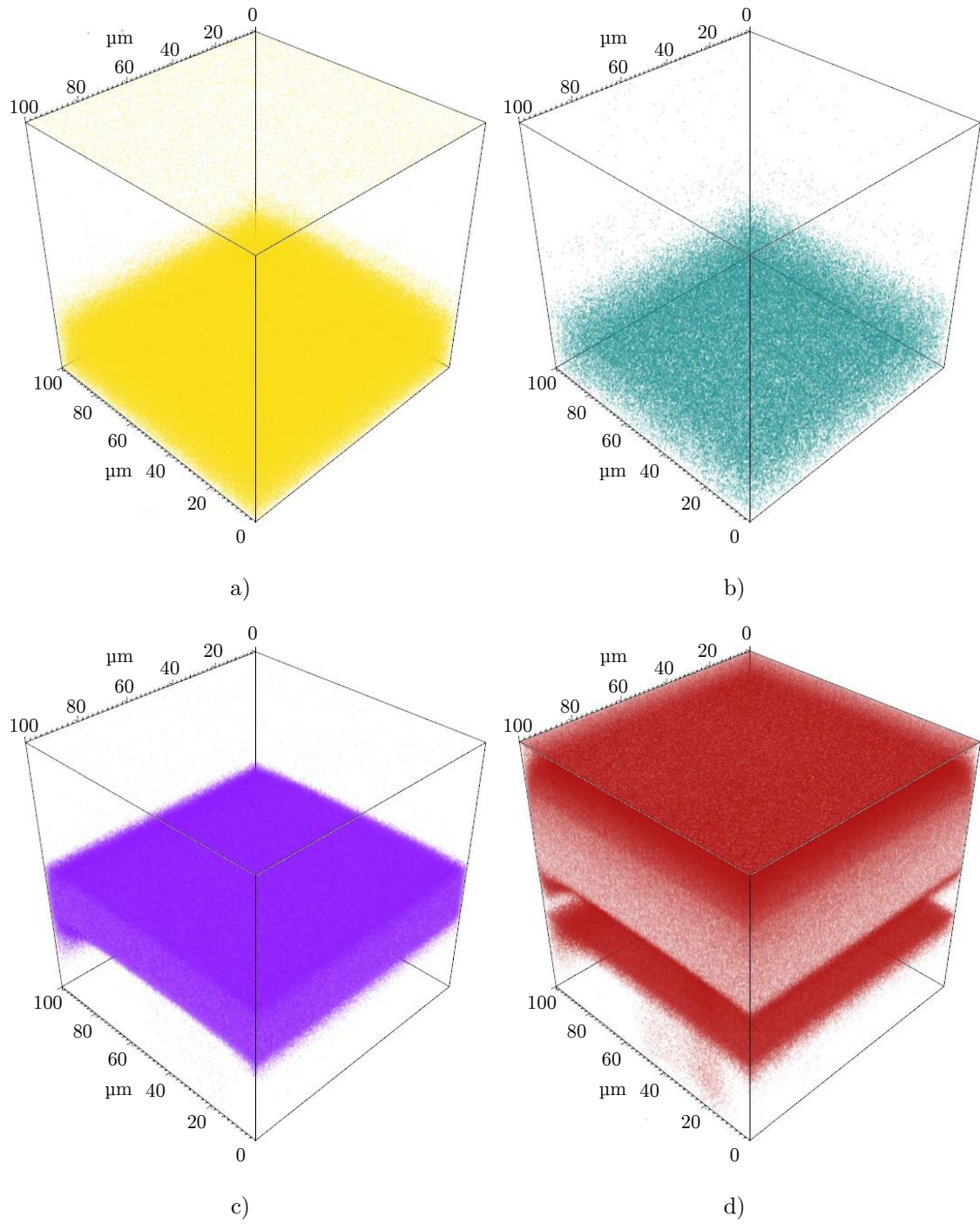


Fig. A.11: Three-dimensional structure of a) Ga, b) As, c) Ti and d) Al of the PV cell measured by SIMS.

*Curriculum Vitae*

# Nikola Papež

Pronouns: he/his

Nikola.Papez@vutbr.cz

+420 54114 6020

---

## EDUCATION

- 2016—Present*    **Degree:** Doctoral in Physical Electronics and Nanotechnology  
**Where:** Brno University of Technology  
Faculty of Electrical Engineering and Communication
- 2019—2020*    **Degree:** Lifelong Learning in Specialized study of Technical Expertise  
**Where:** Brno University of Technology  
Institute of Forensic Engineering
- 2014—2016*    **Degree:** Master's in Communications and Informatics  
**Where:** Brno University of Technology  
Faculty of Electrical Engineering and Communication
- 2010—2014*    **Degree:** Bachelor's in Teleinformatics  
**Where:** Brno University of Technology  
Faculty of Electrical Engineering and Communication

## TEACHING & WORKING

- 2016—Present*    **Position:** Learning Assistant  
**Where:** Department of Physics, Brno University of Technology

I am working as an undergraduate teaching assistant in Physics 1 and Physics 2 courses from the spring of my freshman year until my senior year. I teach labs, computer exercises, lead diploma thesis students as a supervisor, create exams and sometimes present extra credit problems for the classes.

As a researcher, I write publications, review papers in impacted journals, give lectures at invited events, and attend international conferences.

## TECHNICAL EXPERIENCE

### *Instruments & Analysis*

Electron microscopy – thin lamellas, EBIC, EDS; atomic force microscopy; Raman spectroscopy – 3D and depth profiling; X-ray photoelectron spectroscopy – heat and cool measurement; 3D printing and more...

### *Software & Coding*

L<sup>A</sup>T<sub>E</sub>X, MATLAB, Linux shell, PHP, HTML, CSS

## RESEARCHER IDENTIFIATORS

**ORCID iD:** 0000-0003-2297-2890

**Researcher ID:** Y-9823-2019

**Scopus ID:** 57195963424

## RESEARCH

*2020—2022*     **Project:** Advanced characterization of materials for sensors and electricity generators

**Where:** Brno University of Technology

**Advisor:** doc. Ing. Petr Sedlák, Ph.D.

*2014—2016*     **Project:** Development of advanced methods for diagnostics of electrotechnical materials and components

**Where:** Brno University of Technology

**Advisor:** doc. Ing. Petr Sedlák, Ph.D.

## PRESENTATIONS & CONFERENCES

- 2020*      **Conference:** Student EEICT  
**Where:** Czech Republic, Brno  
**Presentation:** Structural analysis of GaAs-based PV cells after ionizing irradiation
- 2019*      **Conference:** Student EEICT  
**Where:** Czech Republic, Brno  
**Presentation:** Advanced structural analysis of silicon solar cells
- 2019*      **Conference:** 8<sup>th</sup> International Conference on Materials Structure Micromechanics of Fracture  
**Where:** Czech Republic, Brno  
**Presentation:** Microstructural investigation of defects in photovoltaic cells by the electron beam-induced current method
- 2019*      **Conference:** 4<sup>th</sup> International Conference on Applied Surface Science  
**Where:** Italy, Pisa  
**Presentation:** Performance analysis of GaAs based solar cells under gamma irradiation
- 2019*      **Conference:** Progress in Applied Surface, Interface and Thin Film Science – Renewable Energy News VI  
**Where:** Italy, Florence  
**Presentation:** Effect of gamma radiation on properties and performance of GaAs based solar cells
- 2018*      **Conference:** Saint-Petersburg OPEN  
**Where:** Russia, Saint Petersburg  
**Presentation:** Surface morphology after reactive ion etching of silicon and germanium arsenide based solar cells
- 2018*      **Conference:** Student EEICT  
**Where:** Czech Republic, Brno  
**Presentation:** Morphological structure of solar cells based on silicon and gallium arsenide after ion etching
- 2018*      **Conference:** Solid State Surfaces and Interfaces  
**Where:** Slovakia, Smolenice  
**Presentation:** Characterization of nanoblister on HOPG surface

- 2017*      **Conference:** Photonics Prague 2017  
**Where:** Czech Republic, Prague  
**Presentation:** Thermal stability of gallium arsenide solar cells
- 2017*      **Conference:** Student EEICT  
**Where:** Czech Republic, Brno  
**Presentation:** Characteristics of gallium arsenide solar cells at high temperature
- 2017*      **Conference:** Progress in Applied Surface, Interface and Thin Film Science – Renewable Energy News V  
**Where:** Italy, Florence  
**Presentation:** Degradation analysis of GaAs solar cells at thermal stress



## AUTHOR'S PUBLICATIONS<sup>1</sup>

- 2020 PAPEŽ, Nikola. Structural analysis of GaAs-based PV cells after ionizing irradiation. In: *Proceedings of the 26th Conference STUDENT EEICT 2020*. Brno, 2020, pp. 203–208. ISSN 978-80-214-5735-5
- SOBOLA, Dinara et al. Stereometric analysis of Ta<sub>2</sub>O<sub>5</sub> thin films. *Materials Science-Poland*. 2020. ISSN 2083134X. available from DOI: 10.2478/msp-2019-0083
  - SOBOLA, Dinara et al. Complementary SEM-AFM of swelling Bi-Fe-O film on HOPG substrate. *Materials*. 2020, vol. 13, no. 10. ISSN 19961944. Available from DOI: 10.3390/ma13102402
- DALLAEV, Rashid et al. Investigation of structure of AlN thin films using Fourier-transform infrared spectroscopy. *Procedia Structural Integrity*. 2019, vol. 23, pp. 601–606. ISSN 24523216. Available from DOI: 10.1016/j.prostr.2020.01.152
- PAPEŽ, Nikola et al. Microstructural investigation of defects in photovoltaic cells by the electron beam-induced current method. *Procedia Structural Integrity*. 2019, vol. 23, pp. 595–600. ISSN 24523216. Available from DOI: 10.1016/j.prostr.2020.01.151
- PAPEŽ, Nikola et al. Performance analysis of GaAs based solar cells under gamma irradiation. *Applied Surface Science*. 2020, vol. 510. ISSN 01694332. Available from DOI: 10.1016/j.apsusc.2020.145329
  - PAPEŽ, Nikola et al. Effect of gamma radiation on properties and performance of GaAs based solar cells. *Applied Surface Science*. 2020, vol. 527. ISSN 01694332. Available from DOI: 10.1016/j.apsusc.2020.146766
- 2019 PAPEŽ, Nikola. Advanced structural analysis of silicon solar cells. In: *Proceedings of the 25th Conference STUDENT EEICT 2019*. Brno, 2019, pp. 723–727. ISSN 978-80-214-5735-5
- SOBOLA, Dinara et al. Characterization of nanoblister on HOPG surface. *Journal of Electrical Engineering*. 2019, vol. 70, no. 7, pp. 132–136. ISSN 13353632. Available from DOI: 10.2478/jee-2019-0055
- 2018 PAPEŽ, Nikola. Morphological structure of solar cells based on silicon and gallium arsenide after ion etching. In: *Proceedings of the 24th Conference STUDENT EEICT 2018*. Brno, 2018, pp. 513–517. ISSN 978-80-214-5735-5

---

<sup>1</sup>Significant publications in impacted journals are marked with a red bullet •.

GAJDOŠ, Adam. et al. Isolation and optoelectronic characterization of Si solar cells microstructure defects. In: *Journal of Physics: Conference Series*. Institute of Physics Publishing, 2018, vol. 1124. No. 4. ISSN 17426596. Available from DOI: 10.1088/1742-6596/1124/4/041009

PAPEŽ, Nikola; HOLCMAN, Ladislav. Efektivní zpracování dat z mikroskopie skenující sondou. *Jemná mechanika a optika*. 2018, vol. 63, pp. 180–182. ISSN 0447-6441

PAPEŽ, Nikola et al. Surface morphology after reactive ion etching of silicon and gallium arsenide based solar cells. In: *Journal of Physics: Conference Series*. Institute of Physics Publishing, 2018, vol. 1124. No. 4. ISSN 17426596. Available from DOI: 10.1088/1742-6596/1124/4/041015

- PAPEŽ, Nikola et al. Degradation analysis of GaAs solar cells at thermal stress. *Applied Surface Science*. 2018, vol. 461, pp. 212–220. ISSN 01694332. Available from DOI: 10.1016/j.apsusc.2018.05.093

ŤĀLU, Štefan et al. Efficient Processing of Data Acquired Using Microscopy Techniques. *DEStech Transactions on Social Science, Education and Human Science*. 2018, vol. 0, no. amse. Available from DOI: 10.12783/dtssehs/amse2018/24838

ŤĀLU, Štefan; PAPEŽ, Nikola; SOBOLA, Dinara; TOFEL, Pavel. Fractal Analysis of the 3-D surface Topography of GaAs Solar Cells. *DEStech Transactions on Environment, Energy and Earth Sciences*. 2018, no. epee. Available from DOI: 10.12783/dteees/epee2017/18173

2017 PAPEŽ, Nikola. Characteristics of gallium arsenide solar cells at high temperature. In: *Proceedings of the 23rd Conference STUDENT EEICT 2017*. Brno, 2017, pp. 693–697. ISSN 978-80-214-5496-5

SOBOLA, Dinara; PAPEŽ, Nikola; ŠKARVADA, Pavel; TOMÁNEK, Pavel. Srovnání metod SEM a SPM pro charakterizaci solárních článků. *Jemná mechanika a optika*. 2017, vol. 62, pp. 81–83. ISSN 0447-6441

- ŤĀLU, Štefan et al. Micromorphology investigation of GaAs solar cells: case study on statistical surface roughness parameters. *Journal of Materials Science: Materials in Electronics*. 2017, vol. 28, no. 20, pp. 15370–15379. ISSN 1573482X. available from DOI: 10.1007/s10854-017-7422-4

PAPEŽ, Nikola; ŠKVARENINA, Lubomír; TOFEL, Pavel; SOBOLA, Dinara. Thermal stability of gallium arsenide solar cells. In: *SPIE-Intl Soc Optical Eng*, 2017, p. 27. ISBN 9781510617025. ISSN 1996756X. available from DOI: 10.1117/12.2292673

SOBOLA, Dinara et al. Application of afm measurement and fractal analysis to study the surface of natural optical structures. *Advances in Electrical and Electronic Engineering*. 2017, vol. 15, no. 3, pp. 569–576. ISSN 18043119. Available from DOI: [10.15598/aeec.v15i3.2242](https://doi.org/10.15598/aeec.v15i3.2242)

ȚĂLU, Ștefan; SOBOLA, Dinara; PAPEŽ, Nikola. Analysis and Recommendations for Education Process of Experts in the Field of Scanning Probe Microscopy. *DEStech Transactions on Social Science, Education and Human Science*. 2017, no. aetms. Available from DOI: [10.12783/dtssehs/aetms2017/15830](https://doi.org/10.12783/dtssehs/aetms2017/15830)